Alma Mater Studiorum · Università di Bologna

Dottorato di ricerca in Fisica
Ciclo XXVII

Settore Concorsuale di afferenza: 02/A1
Settore Scientifico disciplinare: FIS/04

Measurement of the B^0 - $\bar{B}^0$ and B_s^0 - $\bar{B}_s^0$ production asymmetries in pp collisions at $\sqrt{s} = 7$ TeV and $\sqrt{s} = 8$ TeV with the LHCb experiment

Presentata da: Maria Zangoli

Coordinatore Dottorato:
Chiar.mo Prof. Fabio Ortolani

Relatore:
Chiar.mo Prof. Domenico Galli

Correlatore:
Dott. Angelo Carbone

Esame finale anno 2015

Contents

Introduction

One of the most intriguing questions of modern physics is why the Universe we observe is composed of matter. It is believed that at the time of the Big Bang equal amounts of matter and anti-matter were created, hence matter and anti-matter were equally populating the early Universe. Afterwards, particles and anti-particles started to annihilate each other, and according to the Sakharov conditions for the baryon asymmetry, a Universe exclusively composed of matter was left over. Such a phenomenon can be dynamically explained if it exists a violation of the CP symmetry, which differentiates the behaviours of matter and anti-matter. The first experiment revealing the violation of the CP symmetry dates back to 1964 when using the neutral kaon K_L decays, it was discovered that the CP symmetry is violated by weak interactions. In recent years the CP violation has been studied performing a large set of redundant measurements, of increasing precision, in the beauty hadrons system both at the beauty factories, by BABAR and BELLE experiments and at the Large Hadron Collider, mainly by the LHCb experiment.

Due to the large value of the beauty quark (b) production cross-section in proton-proton collisions and the high bunch crossing rate of LHC, the production rate of b-hadrons exploitable by LHCb is huge. However, the production rate of b and $\bar{b}$ hadrons at the LHC are not expected to be strictly identical, due to imbalance between quarks and anti-quarks presence in the pp collisions. This phenomenon can be naively related to the fact that the $\bar{b}$ quark produced in the hard scattering might combine with a u or d valence quark from the colliding protons, whereas the same cannot happen for a b quark. As a consequence, it can be expected to register a slight excess in production of B^+ and B^0 mesons over B^- and $\bar{B}^0$ mesons, giving rise to an asymmetry effect, which is referred to as the production asymmetry.

In the case of the B^0 and B_s^0 mesons the production asymmetry is defined as:

$$A_{\mathrm{P}}\left(B^0_{(s)}\right) = \frac{\sigma\left(\bar{B}^0_{(s)}\right) - \sigma\left(B^0_{(s)}\right)}{\sigma\left(\bar{B}^0_{(s)}\right) + \sigma\left(B^0_{(s)}\right)} \tag{1}$$

where $\sigma\left(\bar{B}^0_{(s)}\right)$ and $\sigma\left(B^0_{(s)}\right)$ denotes the production cross-section.

The production asymmetry is a spurious source of CP violation, to be therefore evaluated and eventually disentangled from the observed asymmetries, aiming to perform precise measurements of CP violation effects occurring in the mixing and decays of the beauty mesons.

This thesis presents the results of the measurements of the production asymmetry $A_{\mathrm{P}}\left(B^0\right)$ of the B^0 meson, which are obtained by performing the time-dependent analysis of the two flavour specific decay modes:

$$B^0 \to J/\psi(\mu^+\mu^-)K^{*0}(K^+\pi^-)$$

and

$$B^0 \to D^-(K^+\pi^-\pi^-)\pi^+.$$

In addition the results of the production asymmetry $A_{\rm P}\left(B_s^0\right)$ of the B_s^0 meson are also provided. They are obtained by means of the time-dependent analysis of the flavour specific decay mode:

$$B_s^0 \to D_s^-(K^+K^-\pi^-)\pi^+.$$

Inclusion of charge-conjugate decay modes is throughout implied.

The measurements of production asymmetries have been performed as a function of transverse momentum ($p_{\rm T}$) and pseudorapidity (η) of B^0 and B_s^0 mesons, to test possible dependence of the hadronization mechanisms on relevant kinematical variables. It is also provided the values of production asymmetries integrated over the ranges $4 < p_{\rm T} < 30\,{\rm GeV}/c$ and $2.5 < \eta < 4.5$, covered by the LHCb detector.

This thesis is organised in three Chapters. The first Chapter explains the CP violation mechanism occurring in the Standard Model, according to the Cabibbo-Kobayashi-Maskawa quark mixing model; it also contains the general formalism that describes the time evolution of neutral B^0 and B_s^0 meson states. For the flavour specific decay modes of interest, it is also shown how differential decay rates depend on the production asymmetry.

The second Chapter describes the main components of LHCb detector, including the trigger system and the analysis tools.

The third Chapter presents the results of the analysis. It describes in all details the procedure used for event selection based on a multivariate analysis technique. It is also shown how the proper time resolution is estimated, the model used to describe time acceptance and how the various sources of backgrounds are parameterised. Finally the fit results are reported, discussing possible dependence of production asymmetry on the pseudorapidity and transverse momentum variables and the various sources of systematic errors and their estimations.

Chapter 1

CP Violation in the Standard Model

1.1 The Standard Model

The Standard Model is a field-theoretic description of strong and electroweak interaction at GeV's energies. It requires as input 18 adjustable parameters [1, 2]. These parameters are not explained by the Standard Model; their presence implies the need for an understanding of Nature at an even deeper level. Nonetheless, processes describes by the Standard Model posses a remarkable insulation from signals of such New Physics.

1.1.1 The fundamental particles and forces

In the Standard Model there are two types of particles: fermions and bosons. Fermions have half-integer spins and obey Fermi-Dirac statistics, while bosons have integer spins and obey Bose-Einstein statistics. There are 12 fermions: six leptons and six quarks. Leptons and quarks can be further arranged in two classes according to electric charge and into three generations, where the particles in each generation can be considered higher mass copies of the previous generation but with identical quantum numbers. The fermions, their charges and their generations are summarised in Table 1.1. Not shown is the corresponding anti-particle of each fermion, which is an oppositely charged particle with otherwise identical fundamental properties, such as mass and spin. There are four types of gauge bosons which mediate the fundamental forces of nature, the photon (γ) for the electromagnetic force, 8 gluons (g) for the strong force, the $W^{\pm}$ and the Z^0 for the weak force. These bosons are exchanged between particles, allowing particles to interact with one another. However, not all of the bosons couple to all of the fermions. The photon only couples to charged particles and therefore cannot interact with the neutrinos, gluons, the Z^0 or even other photons. Gluons only couple to particles which carry the colour charge and so they only couple to the quarks and gluons themselves. The weak force can interact with all of the fermions and is therefore the only force in the Standard Model coupled to neutrinos.

In addition, there is a scalar boson, called the Higgs (H^0), which does not mediate a force but is instead linked to the appearance of mass in the Standard Model. In 2012, the ATLAS and CMS experiments have observed a new boson at the predicted mass of the Higgs boson [3, 4]; results indicate that the new particle is the Higgs boson [5]. The fundamental properties of the Standard Model bosons are summarised in Table 1.2.

In the Standard Model the interactions of particles with the different forces are described by several different Quantum Field Theories (QFTs). The electromagnetic force, described by the theory of Quantum ElectroDynamics (QED), governs the interactions of electrically charged particles. The weak force is the cause of radioactive decays and it allows the coupling of different

	Charge	I Gen	II Gen	III Gen
Leptons	-1	e	μ	τ
	0	ν_e	ν_μ	ν_τ
Quarks	$+2/3$	u	c	t
	$-1/3$	d	s	b

Table 1.1: The basics fermions in the Standard Model: three lepton and quark generations, split into their respective doublets with labelled charge values [6].

Boson	Interaction	Mass (GeV/c^2)	Spin
γ	Electromagnetic	0	1
$W^\pm$	Weak Charged Current	80.385 ± 0.015	1
Z^0	Weak Neutral Current	91.1876 ± 0.0021	1
g	Strong	0	1
H^0	Mass	125.7 ± 0.4	0

Table 1.2: The bosons in the Standard Model and their respective spins, masses and interactions [6]

flavours of fermions. It also allows Charge-Parity (CP) violation to occur, which will be discussed in the next section. The current Standard Model unifies the electromagnetic and weak forces, which are therefore called the ElectroWeak (EW) interaction. The strong force is responsible for the binding and confinement of quarks into hadrons, as well as the attraction between nucleons in the nucleus of an atom. Particles with colour charge (quarks and gluons) can interact with the strong force and these interactions are described by Quantum ChromoDynamics (QCD). The Standard Model does not describe gravitational force.

1.2 CP Violation

Symmetries play an important role in physics since they limit the possible terms which enter the Lagrangian according to conservation laws. The CP violation in the weak interactions is the violation of the combined conservation laws associated with charge conjugation (C) and parity (P). Charge conjugation is the symmetry operation that transforms a particle into the corresponding antiparticle. Every charged particle has an oppositely charged antimatter counterpart, while the antiparticle of an electrically neutral particle may be identical to the particle, as in the case of the neutral π meson, or it may be distinct, as with the antineutron. Parity, or space inversion, is the reflection in the origin of the space coordinates of a particle or particle system. The parity operation on the particle wave function $\Psi(x, y, z, t)$ transforms it to $\Psi(-x, -y, -z, t)$, or

$$(P\Psi)(x, y, z, t) = \Psi(-x, -y, -z, t). \tag{1.1}$$

Parity conservation or P symmetry implies that any physical process will proceed identically when viewed in mirror image. Before 1950s it was assumed that C and P were exact symmetries of elementary processes. The experiment performed by C. S. Wu [7] in 1956, as proposed by T. D. Lee e C. N. Yang [8], showed a Parity violation in nuclear β-decay. Few weeks later Lederman

and Garwin performed another experiment [9], which allowed the observation of parity violation in the charged pion decay. The experiment showed also that the combined application of the parity operation together with the operation of charge conjugation seems to be a symmetry of nature. Historically, the CP simmetry conservation in the weak interaction was first proposed by L. Landau [10]. In the 1957 Friedman and Telegdi [11], verified independently the CP conservation in pion decay

$$\pi^+ \to \mu^+ \nu_\mu. \tag{1.2}$$

In 1964 Christenson, Cronin e Fitch [12] observed the decay of the long-living neutral kaon K_L, which normally decays in three pion final state with *CP* eigenvalue -1, into two pions with *CP* eigenvalue $+1$. It turned out that not all processes are invariant under the *CP* operation. The observation of *CP* violation allows us to make a convention-free definition of matter, with respect to anti-matter. In recent years most experimental and theoretical developments in the field of flavour physics have occurred in the meson systems involving beauty quarks, and, as a result, the term *B physics* is intimately related to flavour physics [13–15]. The study of B mesons and their decays is not only interesting for the study of *CP* symmetry violation. Many observables in B physics are extremely sensitive to possible contribution of virtual particles, such as those foreseen by models beyond the Standard Model.

1.3 The CKM matrix

The unitary matrix describing the mixing of the quark flavours in the Standard Model is the so called Cabibbo-Kobayashi-Maskawa (CKM) [16, 17]. The CKM matrix, V_{CKM}, is a unitary 3×3 complex matrix: $V_{CKM} V_{CKM}^{+} = 1$.

The charged-current interactions responsible for all flavour-changing process at the quark level are mediated by the charged $W^{\pm}$ weak bosons. They are described by the following expression:

$$J_{cc} = \sum_{i=1}^{3} \overline{u}^i \gamma_\mu (1 - \gamma_5) V_{ik} d^k = \sum_{i=1}^{3} \overline{u}_L^i \gamma_\mu V_{ik} d_L^k \tag{1.3}$$

where $u^i = u, c, t$ are the up-like quark fields and $d^k = d, s, b$ are the down-like quark fields, while V_{ij} represents the couplings of the up-like quarks with the down-like quarks:

$$V_{CKM} = \begin{pmatrix} V_{ud} & V_{us} & V_{ub} \\ V_{cd} & V_{cs} & V_{cb} \\ V_{td} & V_{ts} & V_{tb} \end{pmatrix}. \tag{1.4}$$

The CKM matrix has four free parameters, three mixing angles and one complex phase. This complex phase is the only source of *CP* violation in the Standard Model. Among the various possible conventions, a standard choice to parametrise V_{CKM} is the following:

$$V_{CKM} = \begin{pmatrix} c_{12}c_{13} & s_{12}c_{13} & s_{13}e^{-i\delta} \\ -s_{12}c_{23} - c_{12}s_{23}s_{13}e^{i\delta} & c_{12}c_{23} - s_{12}s_{23}s_{13}e^{i\delta} & s_{23}c_{13} \\ s_{12}s_{23} - c_{12}c_{23}s_{13}e^{i\delta} & -c_{12}s_{23} - s_{12}c_{23}s_{13}e^{i\delta} & c_{23}c_{13} \end{pmatrix} \tag{1.5}$$

where $s_{ij} = \sin\theta_{ij}$, $c_{ij} = \cos\theta_{ij}$ and δ is the *CP* violating phase. Using the standard parametrisation in (1.5), starting from the observed hierarchy relations among the matrix terms $|V_{ij}|$, thanks to the experimental information available on their magnitude, it can be stated that:

$$s_{12} = 0.22 \gg s_{23} = \mathcal{O}(10^{-2}) \gg s_{13} = \mathcal{O}(10^{-3}). \tag{1.6}$$

In order to emphasise the existing hierarchy among the matrix elements it is useful to introduce the "Wolfenstein parametrisation" [18] of the CKM matrix. By defining:

$$s_{12} = \lambda = \frac{|V_{us}|}{\sqrt{|V_{ud}|^2 + |V_{us}|^2}}, \quad s_{23} = A\lambda^2 = \lambda \left|\frac{V_{cb}}{V_{us}}\right|, \quad s_{13}e^{-i\delta} = A\lambda^3(\rho - i\eta) = V_{ub}, \tag{1.7}$$

the CKM matrix in (1.5) can be re-written as a power expansion in the parameter $\lambda = \sin\theta_C$ (where θ_C is the Cabibbo angle [16]):

$$V_{CKM} = \begin{pmatrix} 1-\lambda^2/2 & \lambda & A\lambda^3(\rho - i\eta) \\ -\lambda & 1-\lambda^2/2 & A\lambda^2 \\ A\lambda^3(1-\rho-i\eta) & -A\lambda^2 & 1 \end{pmatrix} + \mathcal{O}\left(\lambda^4\right) \tag{1.8}$$

The amount of *CP* violation in the Standard Model [19] is a phase-convention independent measure, given by the condition on the Jarlskog invariant J:

$$F_u F_d J \neq 0 \tag{1.9}$$

where:

$$\begin{aligned} J &= \Im\left(V_{us}V_{cd}V_{cs}^*V_{ub}^*\right) = c_{12}\,c_{23}\,c_{13}^2\,s_{12}\,s_{23}\,s_{13}\sin\delta = A^2\lambda^6\eta \\ F_u &= \left(m_u^2 - m_c^2\right)\left(m_c^2 - m_t^2\right)\left(m_t^2 - m_u^2\right) \\ F_d &= \left(m_d^2 - m_s^2\right)\left(m_s^2 - m_b^2\right)\left(m_b^2 - m_d^2\right). \end{aligned} \tag{1.10}$$

This condition is related to the fact that it would be possible to remove the CKM phase if any of two quarks with the same charge were degenerated in mass. As a consequence the origin of *CP* violation is deeply connected to the "flavour problem", with the origin of quark masses hierarchy, and number of fermion generations. J can be interpreted as a measurement of the entity of *CP* violation in the Standard Model. Its value does not depend on the phase convention of the quark fields. Experimentally one has $J = \mathcal{O}\left(10^{-5}\right)$, which states that *CP* violation in Standard Model is very small. Various extensions of the Standard Model foresee new sources of flavour mixing which could enhance the strength of the violation.

The unitarity of the CKM matrix leads to a set of 12 equations relating the matrix elements: 6 for diagonal terms equal to 1 and 6 for the off-diagonal terms equal to 0. The equations for the off-diagonal terms can be represented as triangles in the complex plane, all having the same area, equal to $J/2$:

$$\underbrace{V_{ud}V_{us}^*}_{\mathcal{O}(\lambda)} + \underbrace{V_{cd}V_{cs}^*}_{\mathcal{O}(\lambda)} + \underbrace{V_{td}V_{ts}^*}_{\mathcal{O}(\lambda^5)} = 0 \tag{1.11}$$

$$\underbrace{V_{us}V_{ub}^*}_{\mathcal{O}(\lambda^4)} + \underbrace{V_{cs}V_{cb}^*}_{\mathcal{O}(\lambda^2)} + \underbrace{V_{ts}V_{tb}^*}_{\mathcal{O}(\lambda^2)} = 0 \tag{1.12}$$

$$\underbrace{V_{ud}V_{ub}^*}_{(\rho+i\eta)A\lambda^3} + \underbrace{V_{cd}V_{cb}^*}_{-A\lambda^3} + \underbrace{V_{td}V_{tb}^*}_{(1-\rho-i\eta)A\lambda^3} = 0 \tag{1.13}$$

$$\underbrace{V_{ud}^*V_{cd}}_{\mathcal{O}(\lambda)} + \underbrace{V_{us}^*V_{cs}}_{\mathcal{O}(\lambda)} + \underbrace{V_{ub}^*V_{cb}}_{\mathcal{O}(\lambda^5)} = 0 \tag{1.14}$$

$$\underbrace{V_{cd}^*V_{td}}_{\mathcal{O}(\lambda^4)} + \underbrace{V_{cs}^*V_{ts}}_{\mathcal{O}(\lambda^2)} + \underbrace{V_{cb}^*V_{tb}}_{\mathcal{O}(\lambda^2)} = 0 \tag{1.15}$$

$$\underbrace{V_{ud}^*V_{td}}_{(1-\rho-i\eta)A\lambda^3} + \underbrace{V_{us}^*V_{ts}}_{-A\lambda^3} + \underbrace{V_{ub}^*V_{tb}}_{(\rho+i\eta)A\lambda^3} = 0. \tag{1.16}$$

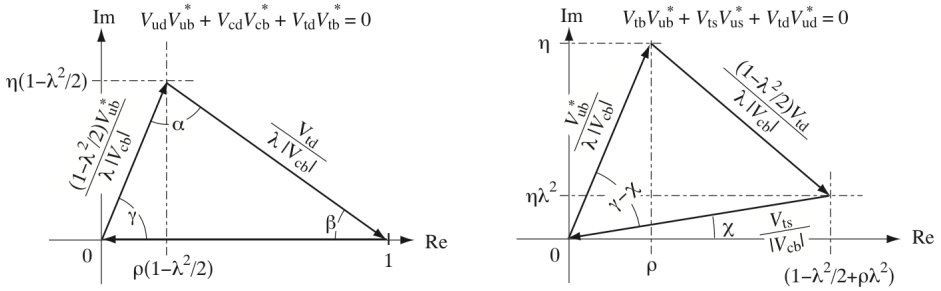

Figure 1.1: Representation in the complex plane of the unitary triangles described in the text: on the left the UT corresponding to Eq. (1.13); on the right the triangle corresponding to Eq. (1.16) is reported.

In these equations we emphasised the values of each product $V_{ij}V_{kl}^*$ at the leading order in λ as obtained from Eq. (1.8), representing the length of the corresponding triangle sides. Only two out of the six unitary triangles have sides of the same order of magnitude: they are described by Eqs. (1.13) and (1.16). The unitarity relations can be represented as triangles in the complex plane, known as unitarity triangles, UT. They are plotted in Fig. 1.1. It is usual practice to normalise the sides lengths of the triangles with respect to the magnitude of $V_{cd}V_{cb}^\star$. The angles of the UT, as shown in Fig. 1.1 can be then written as:

$$\begin{aligned} \alpha &= \arg\left(-\frac{V_{td}V_{tb}^*}{V_{ud}V_{ub}^*}\right) = \pi - \beta - \gamma \\ \beta &= \arg\left(-\frac{V_{cd}V_{cb}^*}{V_{td}V_{tb}^*}\right) \\ \gamma &= \arg\left(-\frac{V_{ud}V_{ub}^*}{V_{cd}V_{cb}^*}\right) \end{aligned} \tag{1.17}$$

and it is useful to define the equivalent of β in the B_s^0-system:

$$\beta_s = \arg\left(\frac{V_{ts}V_{tb}^*}{V_{cs}V_{cb}^*}\right) \equiv \chi. \tag{1.18}$$

The angles of the UT, which are combinations of the CKM elements, are usually probed through quantum interference measurements. For example, the angle β measures the relative phase of $V_{cd}V_{cb}^*$ with respect to $V_{td}V_{tb}^*$, which is involved in $B^0 \leftrightarrow \bar{B}^0$ box mixing diagrams. Direct decays to a *CP* eigenstate, $B_d^0 \to f$ or $\bar{B}_d^0 \to f$ and indirect decays (through the oscillation) $B_d^0 \to \bar{B}_d^0 \to f$ provide the interference terms in the observable widths that allows to probe the relative phase β. A multitude of measurements can be performed in order to constrain the UT. An example of the fit results, performed by the UTfit collaboration [20], to determine the UT parameters, is shown in Fig. 1.2. The measurement of the UT parameters plays a key role in the physics programme of LHCb.

1.4 Neutral Meson Time Evolution

The time evolution (oscillation and decays) of the B_q^0 - $\bar{B}_q^0$ system can be written as a superposition of particle states:

$$|\Psi(t)\rangle = a(t)\left|B_q^0\right\rangle + b(t)\left|\bar{B}_q^0\right\rangle + c_1(t)|f_1\rangle + c_2(t)|f_2\rangle + c_3(t)|f_3\rangle \ldots \tag{1.19}$$

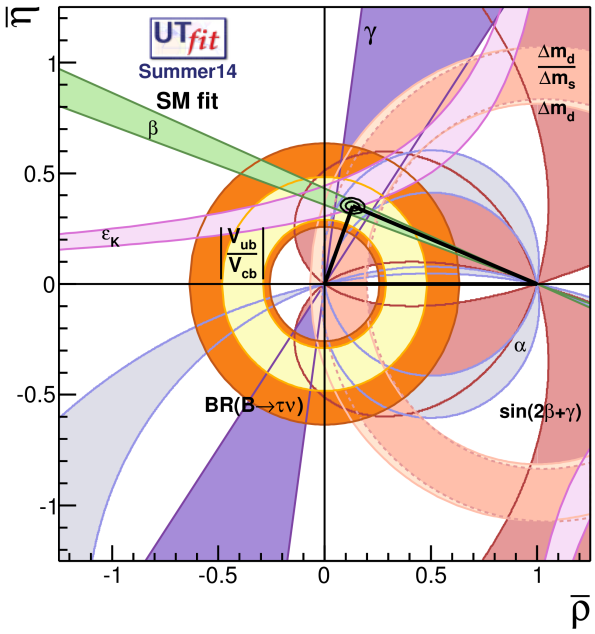

Figure 1.2: The global fit of the UT, by the UTfit group [21]. The coloured bands correspond to the constraints from different measurements. E.g. Δm_s and Δm_d are mass differences from $B^0_{s,d}$ meson mixing, and ϵ_K is a mixing parameter in the kaon sector [6]. An example of Unitarity Triangle is superimposed.

where the $\left|B^0_q\right\rangle$ and $\left|\bar{B}^0_q\right\rangle$ represent the particle and antiparticle state of the B^0_q meson, which are eigenstates of the strong and electromagnetic interactions with common mass m_0 and opposite flavour content; the f_i represent all possible final states where the mesons is allowed to decay into; $c_i\,(t)$ are the coefficients of each final state. The state $|\Psi(t)\rangle$ must obey the Schrödinger equation:

$$i\hbar\frac{\partial|\Psi(t)\rangle}{\partial t} = \mathcal{H}|\Psi(t)\rangle \tag{1.20}$$

where $\mathcal{H}$ is the *infinite*-dimensional Hermitian matrix that governs the time evolution; it's a sum of the strong, electromagnetic and weak Hamiltonians:

$$\mathcal{H} = \mathcal{H}_{strong} + \mathcal{H}_{em} + \mathcal{H}_{weak}. \tag{1.21}$$

In order to solve the evolution equation one can make use of the so called Weisskopf-Wigner approximation [22, 23]. In this case the state $|\Psi(t)\rangle$ is a linear combination of B^0_q and $\bar{B}^0_q$ alone:

$$|\psi\,(t)\rangle = a\,(t)\,|B_q\rangle + b\,(t)\left|\bar{B}_q\right\rangle \tag{1.22}$$

with $|a\,(0)|^2 + |b\,(0)|^2 = 1$.

For both the B^0_d and the B^0_s the state $|\psi(t)\rangle$ must then obey

$$i\hbar\frac{\partial|\psi(t)\rangle}{\partial t} = \mathbf{H}|\psi(t)\rangle. \tag{1.23}$$

The simplified time evolution is determined by a 2×2 effective Hamiltonian $\mathbf{H}$. Such a Hamiltonian is not Hermitian, as otherwise mesons would not decay, but it can be expressed in terms of Hermitian matrices $\mathbf{M}$ and $\mathbf{\Gamma}$:

$$i\hbar\frac{\partial|\psi(t)\rangle}{\partial t} = \mathbf{H}|\psi(t)\rangle = \left(\mathbf{M} - \frac{i}{2}\mathbf{\Gamma}\right)|\psi(t)\rangle = \begin{pmatrix} M - \frac{i}{2}\Gamma & M_{12} - \frac{i}{2}\Gamma_{12} \\ M_{12}^* - \frac{i}{2}\Gamma_{12}^* & M - \frac{i}{2}\Gamma \end{pmatrix}|\psi(t)\rangle. \tag{1.24}$$

The $\mathbf{H}$ matrix consist of two parts, $\mathbf{M}$ and $\mathbf{\Gamma}$, which respectively describe different transitions: $\mathbf{M}$ for transition via dispersive intermediate states (off-shell transition); $\mathbf{\Gamma}$ for absorptive intermediate states (on-shell transition). The diagonal terms of the matrix are associated to flavour-conserving transitions, while the off-diagonal elements are associated to flavour changing transitions. CPT conservation* [24] implies that $M_{11} = M_{22}$ and $\Gamma_{11} = \Gamma_{22}$, meaning that mass and total decay width of particle and antiparticle are identical. The diagonal elements of $\mathbf{H}$ are associated with flavour-conserving transitions, while off-diagonal elements are associated with flavour-changing transitions. The $\mathbf{M}$ matrix represents transitions via dispersive intermediate state ("off-shell" transitions), and $\mathbf{\Gamma}$ represents transitions via absorptive intermediate states ("on-shell" transition).

Solving the eigenvalue equation for $\mathbf{H}$ (1.24) one obtain two eigenvalues:

$$\begin{aligned} \lambda_H &= M - \frac{i}{2}\Gamma + \frac{q}{p}\left(M_{12} - \frac{i}{2}\Gamma_{12}\right) \\ \lambda_L &= M - \frac{i}{2}\Gamma - \frac{q}{p}\left(M_{12} - \frac{i}{2}\Gamma_{12}\right), \end{aligned} \tag{1.25}$$

and corresponding eigenstates $B_{H,L}$ with masses $M_{H,L}$ and widths $\Gamma_{H,L}$

$$\begin{aligned} |B_H\rangle &= \frac{p\,|B\rangle + q\,\left|\bar{B}\right\rangle}{\sqrt{|p|^2 + |q|^2}} \\ |B_L\rangle &= \frac{p\,|B\rangle - q\,\left|\bar{B}\right\rangle}{\sqrt{|p|^2 + |q|^2}}. \end{aligned} \tag{1.26}$$

where H and L indicate respectively the heavy and light mass eigenstates. The p and q terms being:

$$\left(\frac{q}{p}\right) = \sqrt{\frac{M_{12}^* - (i/2)\,\Gamma_{12}^*}{M_{12} - (i/2)\,\Gamma_{12}}}. \tag{1.27}$$

The time evolution of a pure flavour initial state can be written by using the eigenstates (1.26) as:

$$\begin{aligned} |B\,(t)\rangle &= g_+\,(t)\,|B\rangle + \frac{q}{p}g_-\,(t)\,\left|\bar{B}\right\rangle, \qquad |B(0)\rangle = |B^0\rangle \\ \left|\bar{B}\,(t)\right\rangle &= g_+\,(t)\,\left|\bar{B}\right\rangle + \frac{p}{q}g_-\,(t)\,|B\rangle, \qquad |\bar{B}(0)\rangle = |\bar{B}^0\rangle \end{aligned} \tag{1.28}$$

where

$$g_+\,(t) = \frac{1}{2}\left(e^{-i\lambda_H t} + e^{-i\lambda_L t}\right), \qquad g_-\,(t) = \frac{1}{2}\left(e^{-i\lambda_H t} - e^{-i\lambda_L t}\right). \tag{1.29}$$

*T represents the time reversal operator that changes the time flow direction ($t \to -t$).

Denoting by A_f, $A_{\bar{f}}$, $\bar{A}_f$ and $\bar{A}_{\bar{f}}$ the amplitudes for the decay of B or $\bar{B}$ into a final state f or $\bar{f}$:

$$\begin{aligned} A_f &= A\left(B \to f\right) \\ \bar{A}_f &= A\left(\bar{B} \to f\right) \\ \bar{A}_{\bar{f}} &= A\left(\bar{B} \to \bar{f}\right) \\ A_{\bar{f}} &= A\left(B \to \bar{f}\right). \end{aligned} \tag{1.30}$$

According to the expressions of the time evolution of the B states (1.28) and the expressions of the decay amplitudes defined at (1.30), the decay rate to a final state f and its CP conjugate $\bar{f}$ are the following:

$$\begin{aligned} \Gamma_{B\to f}\left(t\right) &\equiv \Gamma\left(\left|B(t)\right\rangle \to \left|f\right\rangle\right) = \left|A_f\right|^2 \cdot \left|g_+\left(t\right) + \lambda_f g_-\left(t\right)\right|^2 \\ \Gamma_{\bar{B}\to f}\left(t\right) &\equiv \Gamma\left(\left|\bar{B}(t)\right\rangle \to \left|f\right\rangle\right) = \left|A_f\right|^2 \cdot \left|\lambda_f g_+\left(t\right) + g_-\left(t\right)\right|^2 \left|\frac{p}{q}\right|^2 \\ \Gamma_{\bar{B}\to \bar{f}}\left(t\right) &\equiv \Gamma\left(\left|\bar{B}(t)\right\rangle \to \left|\bar{f}\right\rangle\right) = \left|\bar{A}_{\bar{f}}\right|^2 \cdot \left|g_+\left(t\right) + \bar{\lambda}_{\bar{f}} g_-\left(t\right)\right|^2 \\ \Gamma_{B\to \bar{f}}\left(t\right) &\equiv \Gamma\left(\left|B(t)\right\rangle \to \left|\bar{f}\right\rangle\right) = \left|\bar{A}_{\bar{f}}\right|^2 \cdot \left|\bar{\lambda}_{\bar{f}} g_+\left(t\right) + g_-\left(t\right)\right|^2 \left|\frac{q}{p}\right|^2, \end{aligned} \tag{1.31}$$

where the complex parameters are:

$$\lambda_f = \frac{q}{p}\frac{\bar{A}_f}{A_f}, \qquad \bar{\lambda}_{\bar{f}} = \frac{p}{q}\frac{A_{\bar{f}}}{\bar{A}_{\bar{f}}}. \tag{1.32}$$

Defining $M_{12} \equiv \left|M_{12}\right| e^{i\varphi_M}$ and $\Gamma_{12} \equiv \left|\Gamma_{12}\right| e^{i\varphi_\Gamma}$ we can write:

$$\begin{aligned} \lambda_H - \lambda_L &= 2\sqrt{\left(M_{12} - \frac{i}{2}\Gamma_{12}\right)\left(M_{12}^* - \frac{i}{2}\Gamma_{12}^*\right)} \\ &= 2\left|M_{12}\right|\sqrt{1 - \frac{\left|\Gamma_{12}\right|^2}{4\left|M_{12}\right|^2} - i\frac{\left|\Gamma_{12}\right|}{\left|M_{12}\right|}\cos\left(\varphi_M - \varphi_\Gamma\right)}. \end{aligned} \tag{1.33}$$

Since, according to [25]:

$$\frac{\Gamma_{12}}{M_{12}} \propto \frac{m_b^2}{m_t^2} = \mathcal{O}\left(10^{-3}\right). \tag{1.34}$$

We can expand (1.33) in terms of $\left|\Gamma_{12}\right| / \left|M_{12}\right|$, neglecting second order terms, as:

$$\lambda_H - \lambda_L \approx \underbrace{2\left|M_{12}\right|}_{\Delta M} - \underbrace{2i\left|\Gamma_{12}\right|\cos\left(\varphi_M - \varphi_\Gamma\right)}_{\Delta\Gamma}. \tag{1.35}$$

In the end we can write:

$$\begin{aligned} \lambda_H &= M + \frac{\Delta M}{2} - \frac{i}{2}\left(\Gamma + \frac{\Delta\Gamma}{2}\right) \\ \lambda_L &= M - \frac{\Delta M}{2} - \frac{i}{2}\left(\Gamma - \frac{\Delta\Gamma}{2}\right). \end{aligned} \tag{1.36}$$

Now, inserting Eqs. (1.36) in Eqs. (1.31) we can write:

$$\begin{aligned}
\Gamma_{B\to f}(t) &= |A_f|^2 e^{-\Gamma t}\left[I_+(t) + I_-(t)\right] \\
\Gamma_{\bar{B}\to f}(t) &= |A_f|^2 e^{-\Gamma t}\left[I_+(t) - I_-(t)\right]\left|\frac{p}{q}\right|^2 \\
\Gamma_{\bar{B}\to \bar{f}}(t) &= \left|\bar{A}_{\bar{f}}\right|^2 e^{-\Gamma t}\left[\bar{I}_+(t) + \bar{I}_-(t)\right] \\
\Gamma_{B\to \bar{f}}(t) &= \left|\bar{A}_{\bar{f}}\right|^2 e^{-\Gamma t}\left[\bar{I}_+(t) - \bar{I}_-(t)\right]\left|\frac{q}{p}\right|^2
\end{aligned} \tag{1.37}$$

where:

$$\begin{aligned}
I_+(t) &= \left(1 + |\lambda_f|^2\right)\cosh\left(\frac{\Delta\Gamma}{2}t\right) - 2\Re(\lambda_f)\sinh\left(\frac{\Delta\Gamma}{2}t\right) \\
I_-(t) &= \left(1 - |\lambda_f|^2\right)\cos(\Delta M t) - 2\Im(\lambda_f)\sin(\Delta M t) \\
\bar{I}_+(t) &= \left(1 + \left|\bar{\lambda}_{\bar{f}}\right|^2\right)\cosh\left(\frac{\Delta\Gamma}{2}t\right) - 2\Re\left(\bar{\lambda}_{\bar{f}}\right)\sinh\left(\frac{\Delta\Gamma}{2}t\right) \\
\bar{I}_-(t) &= \left(1 - \left|\bar{\lambda}_{\bar{f}}\right|^2\right)\cos(\Delta M t) - 2\Im\left(\bar{\lambda}_{\bar{f}}\right)\sin(\Delta M t).
\end{aligned} \tag{1.38}$$

1.5 Flavour specific decays

If only the decay mode $B \to f$ is allowed, while $\bar{B} \to f$ is forbidden, the decay mode is called *flavour-specific* or *tagging mode*. In this case the amplitude defined at (1.30) become:

$$A_{\bar{f}} = 0, \qquad \bar{A}_f = 0 \tag{1.39}$$

and the terms defined at (1.32) in turn become:

$$\lambda_f = 0, \qquad \bar{\lambda}_{\bar{f}} = 0. \tag{1.40}$$

Accordingly, equations (1.38) collapse in the expressions below:

$$I_+(t) = \cosh\left(\frac{\Delta\Gamma}{2}t\right) = \bar{I}_+, \tag{1.41}$$

$$I_-(t) = \cos(\Delta M t) = \bar{I}_-. \tag{1.42}$$

We can rewrite the decay rate defined at (1.37) as:

$$\begin{aligned}
\Gamma_{B\to f}(t) &= |A_f|^2 e^{-\Gamma t}\left[I_+(t) + I_-(t)\right] \\
\Gamma_{\bar{B}\to f}(t) &= |A_f|^2 e^{-\Gamma t}\left[I_+(t) - I_-(t)\right]\left|\frac{p}{q}\right|^2 \\
\Gamma_{\bar{B}\to \bar{f}}(t) &= \left|\bar{A}_{\bar{f}}\right|^2 e^{-\Gamma t}\left[I_+(t) + I_-(t)\right] \\
\Gamma_{B\to \bar{f}}(t) &= \left|\bar{A}_{\bar{f}}\right|^2 e^{-\Gamma t}\left[I_+(t) - I_-(t)\right]\left|\frac{q}{p}\right|^2.
\end{aligned} \tag{1.43}$$

Let's assume that the sample of B^0 is initially equal to N_B and the initial number of $\bar{B}^0$ is equal to $N_{\bar{B}}$, then the number of B and $\bar{B}$ mesons decays to f and $\bar{f}$ final states at a given time t can

be written as:

$$\begin{aligned} N_{B\to f}(t) &= N_B \times \Gamma_{B\to f}(t) \\ N_{\bar{B}\to f}(t) &= N_{\bar{B}} \times \Gamma_{\bar{B}\to f}(t) \\ N_{\bar{B}\to \bar{f}}(t) &= N_{\bar{B}} \times \Gamma_{\bar{B}\to \bar{f}}(t) \\ N_{B\to \bar{f}}(t) &= N_B \times \Gamma_{B\to \bar{f}}(t). \end{aligned} \tag{1.44}$$

Because of the production asymmetry can be defined as:

$$A_P = \frac{N_{\bar{B}} - N_B}{N_{\bar{B}} + N_B}, \tag{1.45}$$

the numbers of B and $\bar{B}$ mesons at $t = 0$ are:

$$\begin{aligned} N_B &= \frac{N}{2} \times (1 - A_P) \\ N_{\bar{B}} &= \frac{N}{2} \times (1 + A_P) \end{aligned} \tag{1.46}$$

where $N \equiv N_B + N_{\bar{B}}$.
Equations (1.44) can be rewritten using (1.46) as:

$$\begin{aligned} N_{B\to f}(t) &= \frac{N}{2}(1 - A_P)\,\Gamma_{B\to f}(t) \\ N_{\bar{B}\to f}(t) &= \frac{N}{2}(1 + A_P)\,\Gamma_{\bar{B}\to f}(t) \\ N_{\bar{B}\to \bar{f}}(t) &= \frac{N}{2}(1 + A_P)\,\Gamma_{\bar{B}\to \bar{f}}(t) \\ N_{B\to \bar{f}}(t) &= \frac{N}{2}(1 - A_P)\,\Gamma_{B\to \bar{f}}(t) \end{aligned} \tag{1.47}$$

By defining the CP asymmetry A_{CP} as:

$$A_{CP} = \frac{\left|\bar{A}_{\bar{f}}\right|^2 - |A_f|^2}{\left|\bar{A}_{\bar{f}}\right|^2 + |A_f|^2}, \tag{1.48}$$

the square of the decay amplitudes become:

$$\begin{aligned} |A_f|^2 &= \frac{|A|^2}{2} \times (1 - A_{CP}) \\ \left|\bar{A}_{\bar{f}}\right|^2 &= \frac{|A|^2}{2} \times (1 + A_{CP}) \end{aligned} \tag{1.49}$$

where $|A|^2 \equiv |A_f|^2 + \left|\bar{A}_{\bar{f}}\right|^2$.
Equations (1.47) can be rewritten using (1.37) and (1.49):

$$\begin{aligned} N_{B\to f}(t) &= \frac{N}{2}(1 - A_P)\frac{|A|^2}{2}(1 - A_{CP})\,e^{-\Gamma t}\left[I_+(t) + I_-(t)\right] \\ N_{\bar{B}\to f}(t) &= \frac{N}{2}(1 + A_P)\frac{|A|^2}{2}(1 - A_{CP})\,e^{-\Gamma t}\left[I_+(t) - I_-(t)\right]\sigma^{-2} \\ N_{\bar{B}\to \bar{f}}(t) &= \frac{N}{2}(1 + A_P)\frac{|A|^2}{2}(1 + A_{CP})\,e^{-\Gamma t}\left[I_+(t) + I_-(t)\right] \\ N_{B\to \bar{f}}(t) &= \frac{N}{2}(1 - A_P)\frac{|A|^2}{2}(1 + A_{CP})\,e^{-\Gamma t}\left[I_+(t) - I_-(t)\right]\sigma^{2} \end{aligned} \tag{1.50}$$

where $\sigma \equiv |q/p|$.
The detection asymmetry A_f of the final states, defined in terms of the detection efficiencies ϵ_f and $\epsilon_{\bar{f}}$, can written as:

$$A_f = \frac{\epsilon_{\bar{f}} - \epsilon_f}{\epsilon_{\bar{f}} + \epsilon_f} \tag{1.51}$$

then, the efficiencies for reconstructing the final states are:

$$\begin{aligned} \epsilon_f &= \frac{\epsilon_d}{2} \times (1 - A_f) \\ \epsilon_{\bar{f}} &= \frac{\epsilon_d}{2} \times (1 + A_f) \end{aligned} \tag{1.52}$$

where $\epsilon_d \equiv \epsilon_f + \epsilon_{\bar{f}}$.
The untagged observable decay rates can be obtained from equations (1.50) with the efficiencies defined in (1.52) as:

$$\begin{aligned} \widehat{N}_{B\to f}(t) &= \frac{\epsilon_d}{2}(1 - A_f)\frac{N}{2}(1 - A_P)\frac{|A|^2}{2}(1 - A_{CP})\, e^{-\Gamma t}\left[I_+(t) + I_-(t)\right] \\ \widehat{N}_{\bar{B}\to f}(t) &= \frac{\epsilon_d}{2}(1 - A_f)\frac{N}{2}(1 + A_P)\frac{|A|^2}{2}(1 - A_{CP})\, e^{-\Gamma t}\left[I_+(t) - I_-(t)\right]\sigma^{-2} \\ \widehat{N}_{\bar{B}\to \bar{f}}(t) &= \frac{\epsilon_d}{2}(1 + A_f)\frac{N}{2}(1 + A_P)\frac{|A|^2}{2}(1 + A_{CP})\, e^{-\Gamma t}\left[I_+(t) + I_-(t)\right] \\ \widehat{N}_{B\to \bar{f}}(t) &= \frac{\epsilon_d}{2}(1 + A_f)\frac{N}{2}(1 - A_P)\frac{|A|^2}{2}(1 + A_{CP})\, e^{-\Gamma t}\left[I_+(t) - I_-(t)\right]\sigma^{2}. \end{aligned} \tag{1.53}$$

Defining the discrete variabile η as $\eta = 1$ if the final state is f and $\eta = -1$ if the final state is the CP conjugate $\bar{f}$, (1.53) can be shortened to the following:

$$\begin{aligned} \widehat{N}_B(t,\eta) &= \frac{\epsilon_d}{2}(1 - \eta A_f)\frac{N}{2}(1 - A_P)\frac{|A|^2}{2}(1 - \eta A_{CP})\, e^{-\Gamma t}\left[I_+(t) + \eta I_-(t)\right]\sigma^{1-\eta} \\ \widehat{N}_{\bar{B}}(t,\eta) &= \frac{\epsilon_d}{2}(1 - \eta A_f)\frac{N}{2}(1 + A_P)\frac{|A|^2}{2}(1 - \eta A_{CP})\, e^{-\Gamma t}\left[I_+(t) - \eta I_-(t)\right]\sigma^{-1-\eta}. \end{aligned} \tag{1.54}$$

The two expressions for the time dependent decay rates in (1.54) allow us to write the decay pdf as:

$$\begin{aligned} f(t,\eta) &= K(1 - \eta A_{CP})(1 - \eta A_f) \times \\ &\quad \times \left\{ e^{-\Gamma t}\left[\Lambda_+ \cosh\left(\frac{\Delta\Gamma t}{2}\right) + \eta\Lambda_- \cos(\Delta m t)\right]\right\} \end{aligned} \tag{1.55}$$

where K is the normalisation constant and the terms Λ_+ and Λ_- defined as

$$\Lambda_\pm = (1 - A_{\mathrm{P}})\left|\frac{q}{p}\right|^{1-\eta} \pm (1 + A_{\mathrm{P}})\left|\frac{q}{p}\right|^{-1-\eta}, \tag{1.56}$$

contain the production asymmetry A_P we want to measure.

Chapter 2

LHCb detector

LHCb detector [26] is one of the four major experiments operating at the Large Hadron Collider (LHC) at CERN, Switzerland. The experiment is located at point 8 on the LHC tunnel close to Ferney-Voltaire, France just over the border from Geneva. The LHC project has been approved in December 1994. The first beams have circulated in September 2008 and the first collisions at 8 TeV in the centre-of-mass frame took place in April 2012. Up to now an integrated luminosity of 2 fb^{-1} has been recorded by the LHCb experiment at a centre-of-mass energy of 8 TeV.

In this chapter an overall description of the accelerator and of the experiment will be given. Each sub-detector will also be described in the following sections.

2.1 The Large Hadron Collider

The LHC [27] synchrotron represents the state-of-the-art of particle accelerators and one of the most important technological challenges ever made. The LHC is a circular proton-proton collider with a circumference of 26.7 km, located 100 m underground in the tunnel already used for the LEP machine, placed across the Swiss and French borders. The beams travel in opposite direction in two pipes enclosed within superconducting magnets cooled by liquid helium. The machine is designed to collide protons up to a centre-of-mass energy of 14 TeV and an instantaneous luminosity of 10^{34} $\text{cm}^{-2}\text{s}^{-1}$, and heavy ions (Pb-Pb) with an energy of 2.8 TeV per nucleon at a peak luminosity of 10^{27} $\text{cm}^{-2}\text{s}^{-1}$. To reach such values of energy the beams are accelerated in several steps by the CERN accelerator complex, shown in Fig. 2.1. Protons are obtained from ionized hydrogenium atoms deprived of their electrons by an electric field. Linac 2, the first accelerator in the chain, accelerates the protons to the energy of 50 MeV. The beam is then injected into the Proton Synchrotron Booster (PSB), which accelerates the protons to 1.4 GeV, followed by the Proton Synchrotron (PS), which pushes the beam to 25 GeV. Protons are then sent to the Super Proton Synchrotron (SPS) where they are accelerated to 450 GeV. The protons are finally transferred to the two beam pipes of the LHC. The beam in one pipe circulates clockwise while the beam in the other pipe circulates anti-clockwise. It takes 4 minutes and 20 seconds to fill each LHC ring, and 20 minutes for the protons to reach the energy of 4 TeV. The two beams are brought into collision inside four detectors - ALICE, ATLAS, CMS and LHCb - where the total energy at the collision point is equal to 8 TeV. At its nominal regime the LHC rings will store 2808 proton bunches per ring, each of them containing 1.1×10^{11} protons and colliding with a frequency of 40 MHz. The accelerator complex includes the Antiproton Decelerator and the Online Isotope Mass Separator (ISOLDE) facility, and feeds the CERN Neutrinos to Gran Sasso (CNGS) project and the Compact Linear Collider test area, as well as

the neutron time-of-flight facility (nTOF).

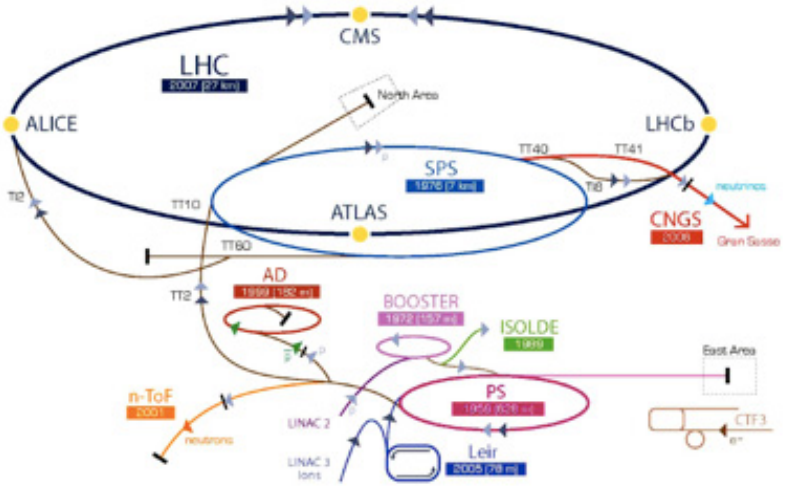

Figure 2.1: Schematic view of the complex of CERN accelerators. The Linac2, Proton Synchrotron Booster (BOOSTER), Proton Synchrotron (PS), Super Proton Synchrotron (SPS), LHC and the two tunnels for the injection of proton beams into the LHC, TI2 (near the ALICE experiment) and TI8 (near the LHCb experiment),mentioned in the text are shown. The Antiproton Decelerator and the Online Isotope Mass Separator (ISOLDE) facility, the CERN Neutrinos to Gran Sasso (CNGS) project and the Compact Linear Collider test area, as well as the neutron time-of-flight facility (nTOF) are also shown.

2.1.1 2011 data taking

In 2011 the data taking operations started on the 12^{th} April and ended at the end of October. During this period LHC operated at an energy of 3.5 TeV per beam. LHCb, in order to cope with detector and trigger design limits, worked with a system allowing to continuously levelling the instantaneous luminosity to about 3.5×10^{32} cm^{-2}s^{-1}; such a value corresponds to about 1.75 times the design instantaneous luminosity.
The total integrated luminosity delivered to LHCb has been 1.22 fb^{-1} and the experiment collected 1.11 fb^{-1} with an efficiency of about 90% as shown in Fig. 2.2.

2.1.2 2012 data taking

In 2012 the data taking operations started on the 5^{th} April and ended in December. The good results obtained in the previous years gave the confidence to increase the energy without any significant risk to the machine, up to 4 TeV per beam. The total integrated luminosity delivered to LHCb was 2.21 fb^{-1} and the experiment collected 2.08 fb^{-1} with an efficiency of about 94%, as shown in Fig. 2.3.

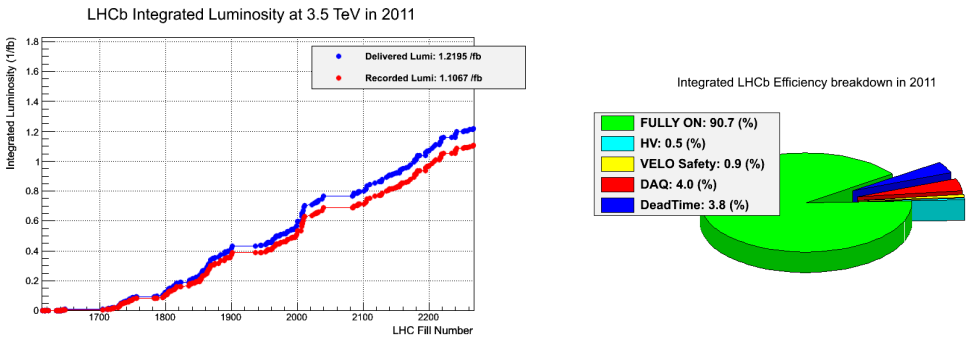

Figure 2.2: On the left: integrated luminosity at $\sqrt{s} = 7$ TeV delivered by LHC to the LHCb experiment (blue points) and recorded luminosity by the LHCb experiment (red points) as a function of fill number during 2011. On the right: pie chart showing the data taking efficiency of the LHCb detector (green) and the various sources of inefficiencies.

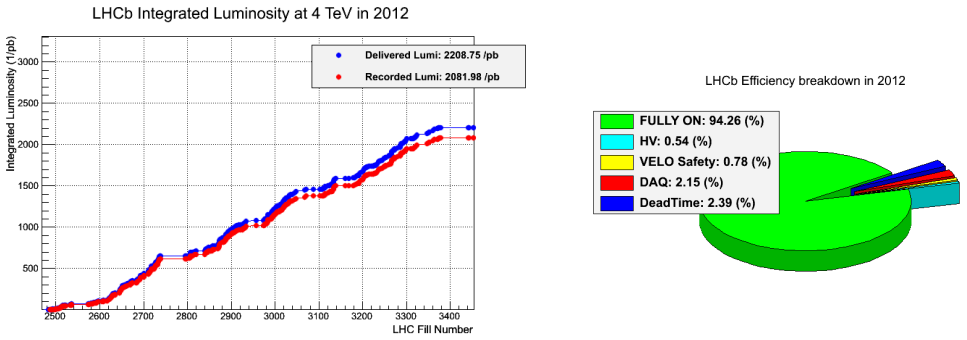

Figure 2.3: On the left: integrated luminosity at $\sqrt{s} = 8$ TeV delivered by LHC to the LHCb experiment (blue points) and recorded luminosity by the LHCb experiment (red points) as a function of fill number during 2012. On the right: pie chart showing the data taking efficiency of the LHCb detector (green) and the various sources of inefficiencies.

2.2 Overview of LHCb

LHCb is a single-arm spectrometer with a forward angular coverage from approximately 10 mrad to 300 mrad in the horizontal plane and between 10 mrad to 250 mrad in the vertical plane. The choice of the detector geometry is justified by the fact that at high energies both b and $\overline{b}$ quarks are predominantly produced in the same forward or backward cone. The pseudo-rapidity (η) range for tracks inside the LHCb geometrical acceptance is between about 1.8 and 4.9.

The physics program at LHCb requires the reconstruction of exclusive leptonic, semi-leptonic and fully hadronic decays and the ability to separate these signals from various background processes. LHCb consists of a system of sub-detectors to satisfy the following requirements:

- **High precision vertex reconstruction and proper-time resolution:** most of the LHCb analyses require time-dependent measurements of B-hadron decay rates. This requires that the precision in the reconstruction of pp interaction vertices and the B decay vertices must be very high, in order to have a suitable proper-time resolution (30-50 fs) to follow the neutral B meson oscillations (in particular the fast B_s^0 one). This measurement

is achieved by the Vertex Locator (VELO).

- **Excellent particle identification** to separate the different final states and discriminate between charged pions, charged kaons and protons in a very wide momentum range (from few GeV/c up to and above 100 GeV/c). These information are achieved by different sub-detectors: two Ring Imaging Cherenkov provide information for the identification of charged particles in different momentum range; the electromagnetic calorimeter system is used to identify electrons and photons while the Muon Stations are used for muons.

- **Energy and momentum resolution** to distinguish the signal peak in the invariant mass spectrum from the flat distribution of random tracks combinations. The LHCb dipole magnet, the tracking system and the calorimeters are all necessary to this purpose.

- **Fast event filtering:** hadron colliders produce primary interactions via quark/gluon fragmentation and this generally results in high multiplicity events. At design luminosity, LHCb is expected to have a visible interaction rate of 10 MHz. Of these, only about 100 kHz comprises $b\bar{b}$ pairs and only $\sim 15\%$ of these have at least one B meson with all decay products within the LHCb acceptance. It is essential to have rapid response event filtering without incurring dead time for the next bunch crossing. The accepted data need to be further reduced to about 2 kHz before the events are written to offline storage. This requires a combination of hardware and software triggers, retaining only events likely to contain decays of interest.

The various sub-detectors are indicated in Fig 2.4. A description of these sub-detectors is given in the subsequent sections of this chapter.

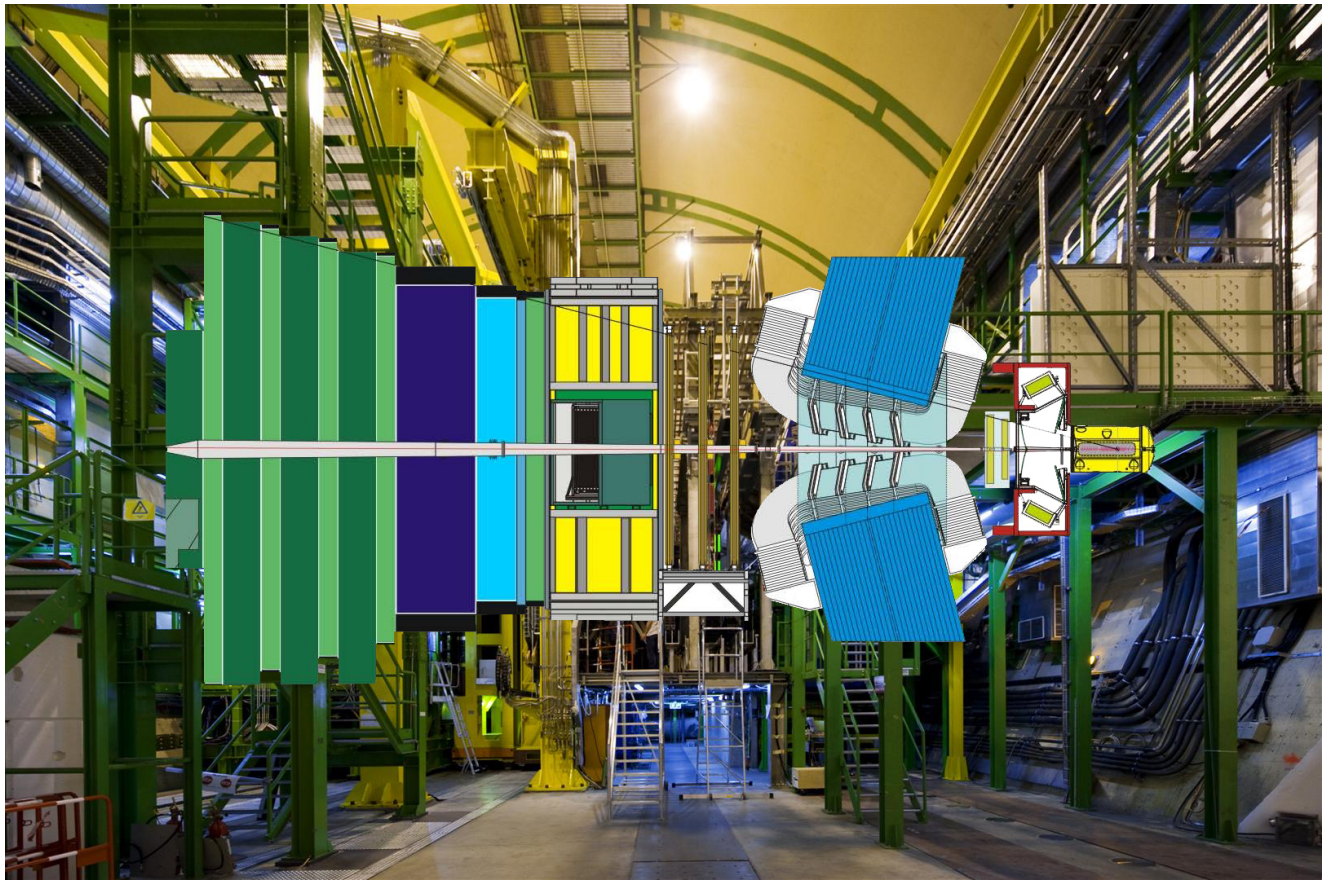

Figure 2.4: Overview of the entire LHCb detector. From right to left the various sub-detectors are visible: VELO, RICH1, TT, Magnet, Tracking Stations, RICH2, Electromagnetic Calorimeter (ECAL), Hadronic Calorimeter (HCAL) and Muon Stations.

2.3 The LHCb dipole magnet

A dipole magnet is used in the LHCb experiment to measure the momentum of charged particles. The magnet consists of two coils, as visible in Fig. 2.5, both weighing 27 tons, mounted inside a 1,450 tons steel frame. Each coil is constructed from 10 pancakes arranged in five triplets and produced of pure Al-99.7 hollow conductor in an annealed state which has a central cooling channel of 25 mm diameter [28]. The generated magnetic field is mainly directed along the Y coordinate such that the bendind plane for charged tracks results to be almost parallel to the horizontal plane of the detector. The maximum intensity of the magnetic field is about 1 T, while the magnetic field integral is about 4 Tm. During the data taking the polarity of the dipole has been flipped several times in order to allow the evaluation of any left-right asymmetry introduced by the detector. In fact positively and negatively charged tracks are bent to different directions by the magnetic field, thus any variation of the detection efficiency between the left and right region of the detector could affect *CP* asymmetry measurements.

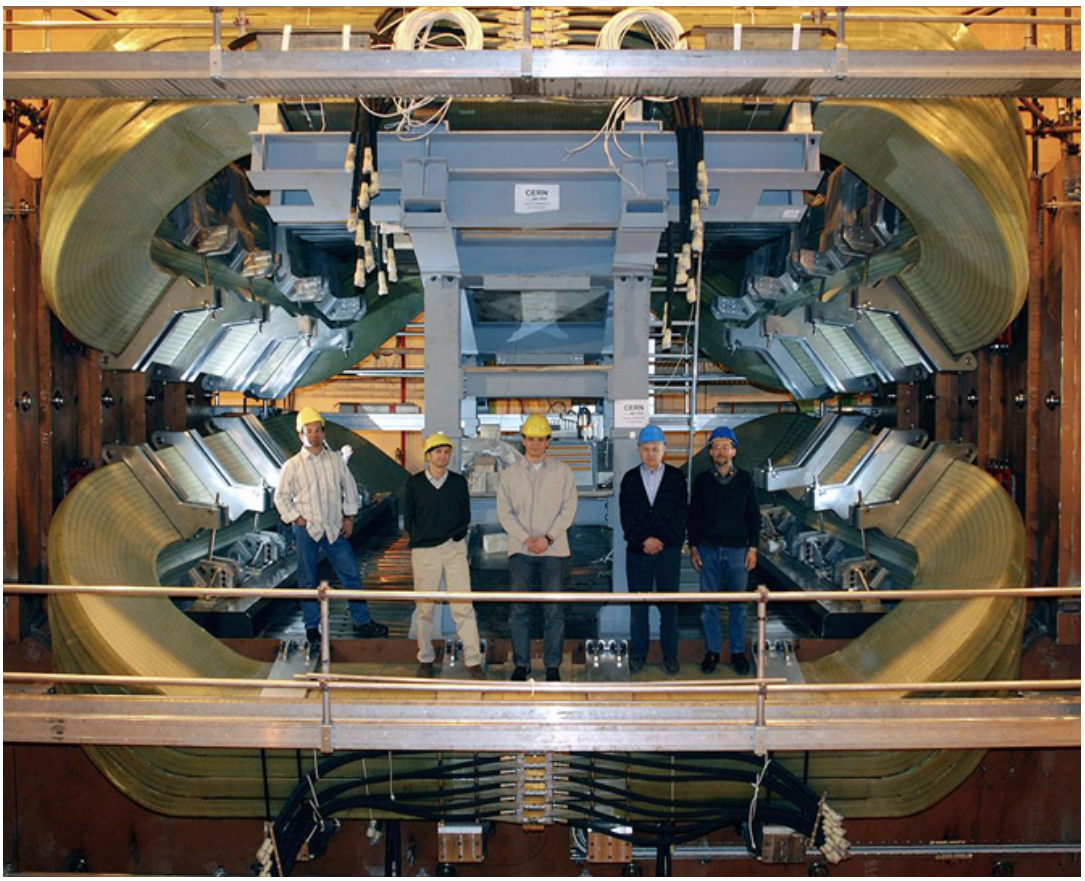

Figure 2.5: Front view of the LHCb dipole magnet after the installation in the detector cavern. The particular profile of the two coils, in order to follow the detector acceptance, is visible.

2.4 The tracking system of LHCb

The LHCb tracking system consists of the vertex locator system (VELO) and four planar tracking stations: the Trigger Tracker (TT) and the three tracking stations (T1, T2 and T3).

2.4.1 The Vertex Locator

The VErtex LOcator (VELO) provides precise measurements of track coordinates close to the interaction region, which are used to identify the displaced secondary vertices which are a distinctive feature of b and c hadron decays [29]. To reach an impact parameter resolution of 20 μm with respect to the primary vertex, the silicon sensor modules of the VELO must be located very close to the beam.

The VELO layout, shown in Fig 2.6, consists of 21 circular stations perpendicular to the beam axis. Each station, composed by two halves of silicon microstrip detectors, provides a measure of the r and ϕ coordinates. The two halves are allowed to move between 3 cm (fully open) and 8 mm (data taking conditions) from the beam. This is done to minimize the material traversed by a charged particle before it crosses the sensors and the geometry is such that it allows the two halves of the station to overlap when in the closed position. The resolution for the reconstruction of the primary vertices is ~ 42 μm along the beam line and ~ 11 μm on the plane perpendicular to the z-axis. Module halves are composed of two planes of 220 μm thick silicon microstrip sensors allowing to measure radial (R-sensors) and polar (ϕ-sensors) coordinates of the hits generated by ionizing particles. For the R-sensor the diode implants are concentric semi-circles with their centre at the nominal LHC beam position. In order to minimize the occupancy each strip is subdivided into four 45° regions. The microstrips are modelled in a semi-circular shape and their width varies from 40 μm (near the beam) to 92 μm (far from the

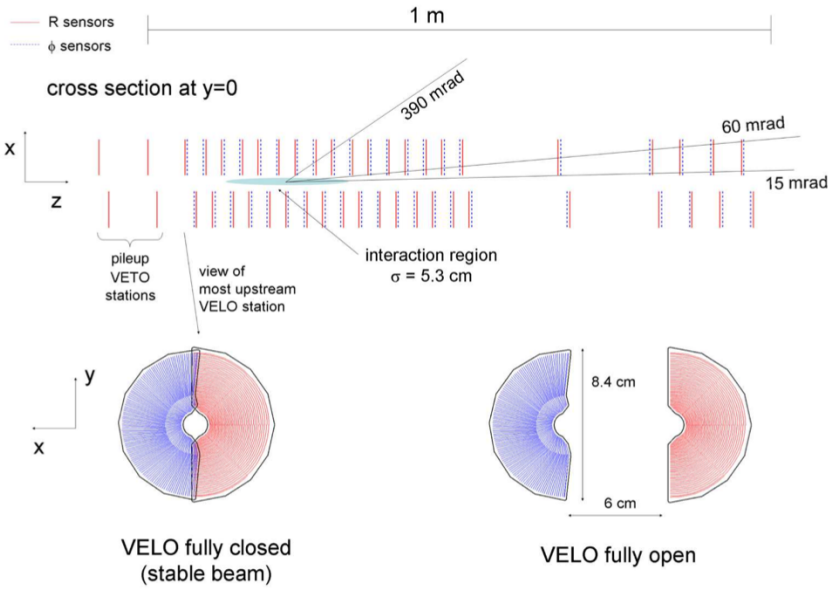

Figure 2.6: On the top: cross section in the (x, z) plane of the VELO silicon sensors, at $y = 0$, with the detector in the fully closed position. On the bottom: front view of the modules in both the closed (left) and open positions (right).

beam) in order to take into account the higher particle occupancy near the interaction point. The ϕ-sensors are designed to readout the orthogonal coordinate to the R-sensor; it's subdivided into two regions, inner and outer. The outer region starts at a radius of 17.25 mm and its pitch is set to be roughly half (39.3 μm) that of the inner region (78.3 μm), which ends at the same radius. Inner and outer regions have different skew to the radial direction in order to improve pattern recognition: 20° and 10° respectively. In addition, for a better stereo view of track reconstruction, longitudinally adjacent ϕ-sensors have opposite skew to each other. A scheme of R and ϕ sensors is reported in Fig. 2.7.

The VELO layout has been optimized to minimize the amount of material in the acceptance while providing good geometrical coverage. All tracks inside the LHCb acceptance ($1.6 \leq \eta \leq 4.9$) pass through at least three VELO modules.

The performances of the VELO detector [30] have been studied by means of the large amount of minimum bias events collected during the first period of LHC physics operation, from 2009 to 2013 and have been compared with full Monte Carlo simulated events. The resolution on vertex position is strongly dependent on the number of tracks in the vertex. A resolution of 13 μm in the transverse plane and 71 μm along the beam axis is achieved for vertices with 25 tracks, as shown in Fig. 2.8. A 1D impact parameter resolution of 12 μm in the plane transverse to the beam for high momentum tracks is obtained. For lower momentum tracks the impact of multiple scattering in the detector material becomes dominant, and an impact parameter resolution of 35 μm for particles with transverse momentum of 1 GeV/c is achieved. The decay time resolution is approximately 50 fs, which plays a key role in many LHCb physics results.

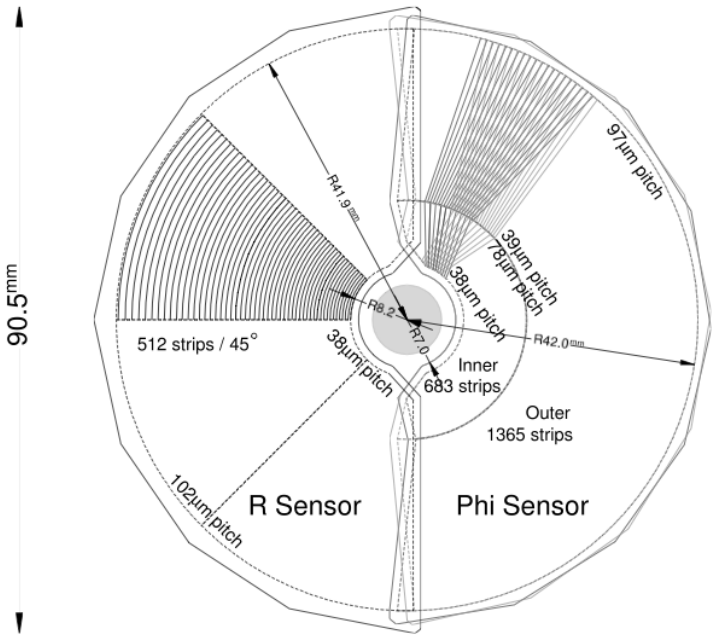

Figure 2.7: Sketch of the geometry of the R (left part) and ϕ (right part) sensors of the VELO. For clarity, only a portion of the strips are illustrated. The strips of the ϕ sensors for two adjacent modules are drawn, in order to highlight their different orientation.

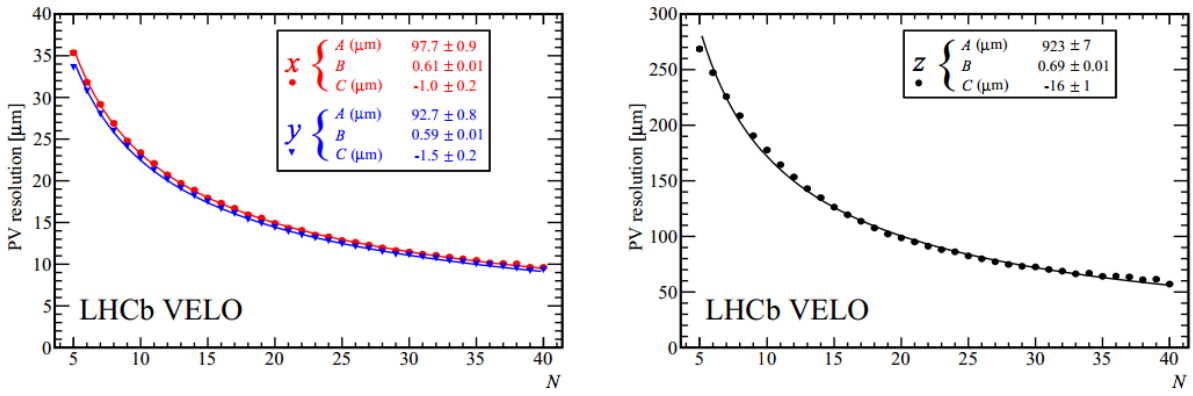

Figure 2.8: PV Resolution of events with exactly one PV in 2011 data as a function of track multiplicity. On the left, x (red) and y (blue) resolution and, on the right, z resolution. The fit parameters A, B and C for each coordinate are given.

2.4.2 The Trigger Tracker

The Trigger Tracker [31] is placed after the first Cherenkov detector (RICH1) and before the magnetic dipole, in a region where a residual magnetic field is present. Its rôle is to provide reference segments to combine the tracks reconstructed in the tracking stations after the magnet and those reconstructed in the VELO in order to improve the resolution on their momentum and trajectory. The system comprises four stations, grouped two-by-two and called TTa and TTb, spaced by approximately 30 cm (as shown in Fig. 2.9) and at a distance of approximatively 2.4 m from the interaction region. Each of the four stations covers a rectangular region 157 cm wide and 132 cm high and covers the full acceptance of the experiment. In order to cope with the high spatial resolution required and the necessity to work in a region with high occupancy of charged tracks, a silicon microstrip technology has been adopted for the sensors of the TT sub-detector. The microstrips have a pitch of about 200 μm and are arranged into up to 38 cm long readout strips. In the first and fourth station the strips are disposed parallel to the vertical plane, while in the second and third station, in order to improve the precision in the reconstruction, they are tilted by +5° (u-layer) and -5° (v-layer) respectively.

2.4.3 The T tracking stations

The tracking stations T1, T2 and T3 are placed behind the magnetic dipole, just before the second Cherenkov detector (RICH2). A schematic view is shown in Fig. 2.10. Two different technologies have been used for the tracking stations: silicon microstrip sensor in the inner part of the detector (Inner Tracker or IT) and drift straw tube in the outer part (Outer Tracker or OT). Each IT station consists of four detection planes overlapped with two of them aligned with the Y axis (x planes) and two of them tilted by $\pm 5°$ (u- and v- plane respectively); as shown in Fig. 2.10 the IT part of each station is placed in front the OT part. The choice of silicon microstrip sensors for the IT [32] has been driven by the high charged track multiplicity close to the beam line. The characteristics of silicon microstrip sensors are the same as those used for the TT: they have a pitch of about 200 μm and they are up to 22 cm long. The sizes of the total Inner Tracker sub-detector are about 1.2 m on the bending plane (X coordinate) and about 40 cm on the vertical plane (Y coordinate).

The Outer Tracker [33] is realized using drift straw tubes technology. For each station four

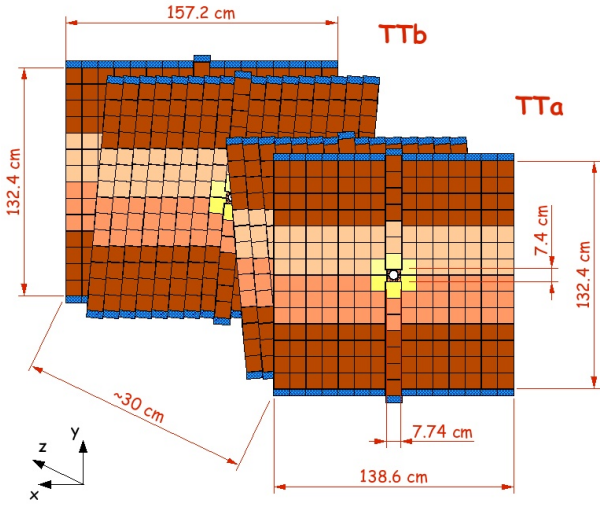

Figure 2.9: Layout of the four TT stations. The front and rear planes have sensors vertically arranged, while the two planes in the middle represent the u-plane and v-plane described in the text with sensors tilted by $\pm 5°$ respectively.

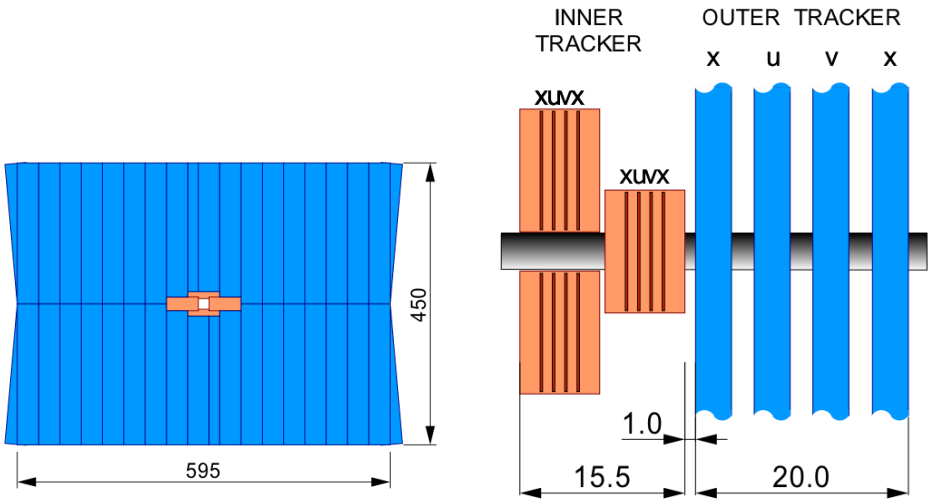

Figure 2.10: On the left: layout of a T station from a front view. The IT subdetector (in orange) is placed around the beam pipe, while the OT sub-detector covers the outer region of the station.
. In the right: layout of a T station from a side view. The IT sub-detector is placed in front of the OT sub-detector. The x- u- and v-planes described in the text are also drawn.

planes of straw tubes are arranged in the same way as the microstrip of TT and IT: first and fourth planes have vertically aligned tubes, while the second and third planes have them tilted by $\pm 5°$ (usual u- and v- planes respectively). In addition each plane has two rows of tubes arranged with a honeycomb structure (see Fig. 2.11) in order to maximize the sensible area.

The configuration defines a bidimensional lattice to measure both the X and Y coordinates of track hits, maintaining the occupancy low. The straw tubes have a radius of 5 mm and are filled with a mixture of $Ar/CF_4/CO_2$ that gives a drift time of the order of 50 ns.

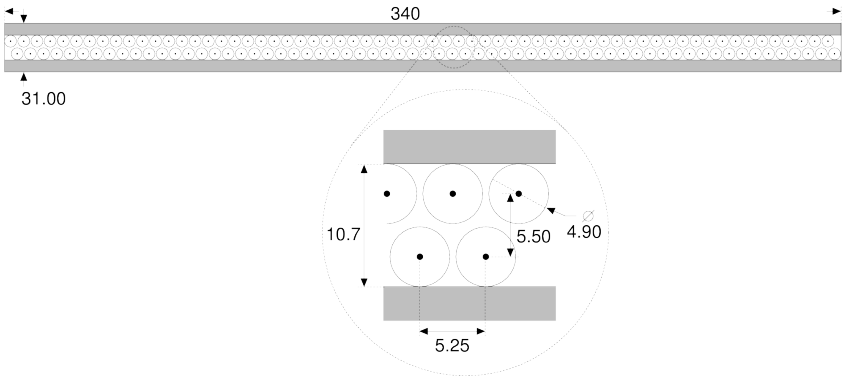

Figure 2.11: Cross section of a straw-tubes module. The zoom-in shows the honeycomb arrangement of the two layers of tubes.

2.5 Identification of charged particles

Particle identification (PID) is a fundamental requirement for LHCb. Most of the measurements of the LHCb physics programme (and in particular those treated in this thesis) require the identification of charged leptons and hadrons. This task is accomplished by some dedicated sub-detectors that we are going to describe.

2.5.1 The RICH detectors

LHCb is provided by two Ring Imaging Cherenkov detectors (RICH1 and RICH2) [34] able to efficiently discriminate charged hadrons in the range between few GeV/c up to about 150 GeV/c. This range of momentum comprises most of the particles coming from B hadron decays. RICH1, using Aerogel and C4F10 radiators, is optimized to identify tracks of lower momentum (between 1 and about 50 GeV/c), while RICH2 is optimized for the identification of tracks of higher momentum (up to 150 GeV/c) using a CF4 radiator. The discrimination of charged pions, kaons and protons in a wide momentum range is crucial in the selection of B hadron decays with these particles in the final states. In addition the distinction between charged pions and kaons coming from the hadronization process of b quarks is used to determine the flavour state at the production of neutral B mesons. This procedure, known as *flavour tagging*, is used to determine if the neutral B meson at $t = 0$ has been produced as a B or $\overline{B}$.

Cherenkov light detectors exploit the relation between the particle momentum and the emission angle of Cherenkov photons:

$$\cos(\theta_c) = \frac{1}{n \cdot v/c}, \tag{2.1}$$

where θ_c is the angle of Cherenkov photon emission with respect to the particle direction of flight, n is the refraction index of the radiator, v is the particle speed and c is the speed of light.

The only way to cover a wide range of momentum is to use different radiators, with different refraction indices. This is because Cherenkov light is emitted only by particles with the

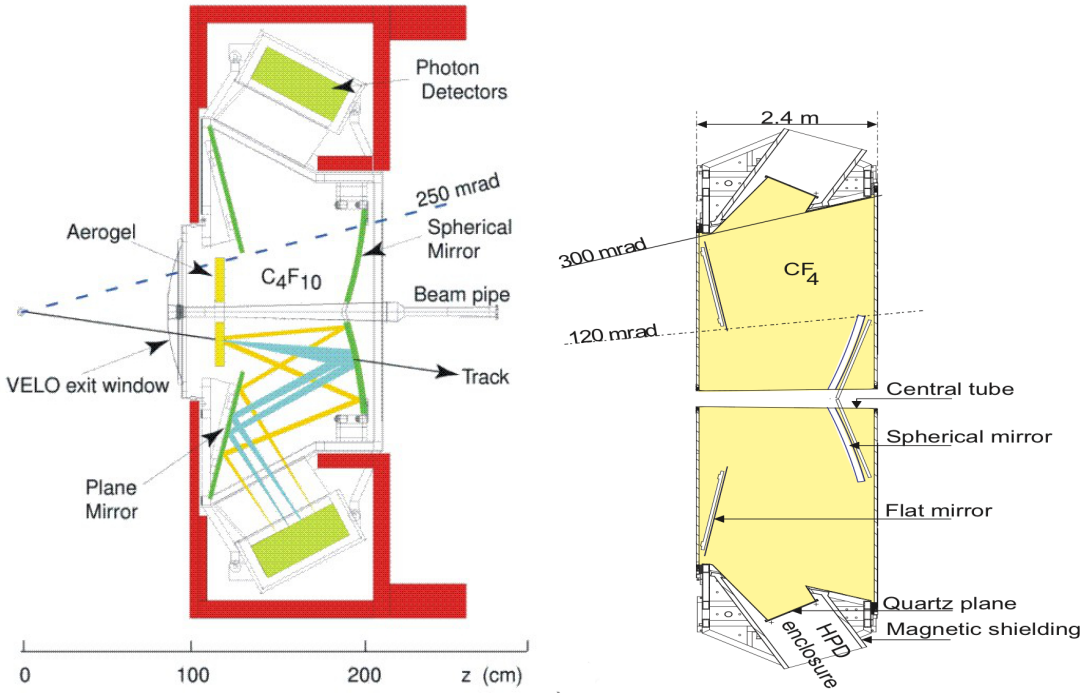

Figure 2.12: On the left: schematic layout from a side view of the RICH1 detector. The Cherenkov light as emitted by a charged track traversing the Aerogel tiles and the C_4F_{10} radiator is also drawn. On the right: schematic layout from a top view of the RICH2 detector.

parameter $\beta = v/c$ in the range $c/n < \beta < c$. For $\beta = 1/n$ the Cherenkov angle will be 0, while approaching the speed of light the Cherenkov angle will saturate at a value $\theta_c = \arccos(1/n)$.

RICH1 is placed between the VELO and the TT detectors (see Fig. 2.4) and is able to cover practically the entire geometrical acceptance of LHCb (between 25 mrad to 330 mrad). It uses two different radiators: a layer of 5 cm thick Aerogel with a refraction index of about $n = 1.03$ (optimal for low momentum particles $1 - 10$ GeV/c), and a gap about 85 cm thick filled with C_4F_{10} with refraction index $n = 1.0015$ (optimal for momenta up to 50 GeV/c). RICH2 is placed between the last tracking station and the first muon station (see Fig. 2.4). Its geometrical acceptance covers an angular region of about 120 mrad in the vertical plane and 100 mrad in the horizontal plane, the region with most of the high momentum particles. As radiator it uses CF_4 with refraction index $n = 1.00046$ inside a gap 170 cm thick. Schematic pictures of RICH1 and RICH2 are reported in Fig. 2.12.

For both the RICH detectors the Cherenkov light emitted is collected by an optical system made of spherical and plane mirrors on two planes equipped with Pixel Hybrid Photon Detector (HPD), placed out of the LHCb acceptance. The anode of these photomultipliers is a silicon pixel sensor on which the electrons (produced by the photocathode) are focused by electric field.

RICH detectors give the information to evaluate the mass-hypothesis likelihood for a given particle. As Cherenkov photons emitted by a particle are characterized by the same emission angle θ_c, they are expected to form a ring on the HPD plane, with radius proportional to θ_c. Thus, given the direction of a particle, it is possible to extrapolate the position of the corresponding ring centre on the photo-detector plane. The distribution of Cherenkov photon hits on the plane, as a function of the radial distance from the centre, is thus expected to

be peaked around a value related to θ_c and smeared by resolution effects. Solitary rings from isolated tracks provide a useful test of the RICH performance, since the reconstructed Cherenkov angle can be uniquely predicted. A track is defined as isolated when its Cherenkov ring does not overlap with any other ring from the same radiator. Fig. 2.13 shows the Cherenkov angle as a function of particle momentum using information from the C4F10 radiator for isolated tracks selected in data ($\sim 2\%$ of all tracks) with the theoretical expectation superimposed. As expected, the events are distributed into distinct bands according to their mass.

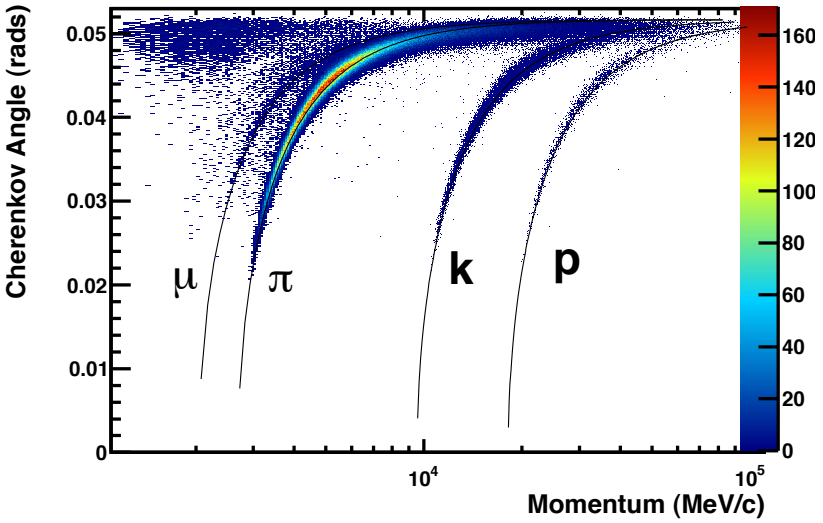

Figure 2.13: Cherenkov angle as a function of track momentum measured for isolated tracks. The theoretical expectations for the various particle hyptheses are superimposed.

The particle-identification discriminating variable used in LHCb is the so called $\Delta \log \mathcal{L}$. The value of the likelihood is computed changing the mass-hypothesis of a single track, maintaining all the other hypotheses unchanged with respect to the maximum-likelihood solution. As the value of the global likelihood can be quite large its logarithm is used. In the end the pion mass-hypothesis is taken as reference, such that $\Delta \log \mathcal{L}$ for the pion hypothesis results to be always 0. Then the discrimination between mass-hypotheses is performed on the basis of the difference of the likelihood logarithm under a generic hypothesis and the pion hypothesis. For example $\Delta \log \mathcal{L}_{K\pi}(P)$ is the difference between the logarithm of the likelihood under the K hypothesis and under the π hypothesis for the particle P:

$$\Delta \log \mathcal{L}_{K\pi}(P) = \log \mathcal{L}_K(P) - \log \mathcal{L}_\pi(P), \tag{2.2}$$

thus a large positive value of $\Delta \log \mathcal{L}_{K\pi}(P)$ translates to a large confidence that the particle P is a kaon. Performances of RICH detectors in discriminating between mass-hypotheses have been studied by means of real data samples. Thanks to the high production rate and to their kinematic characteristics, particle decays like $K^0_S \to \pi^+\pi^-$, $\Lambda \to p\pi^-$ and $D^{*+} \to D^0 (\to K^-\pi^+)\pi^+$ allow to select pure high statistics samples of pions and kaons without making any use of RICH detectors. Due to the dependence of θ_c on particle momentum, also $\Delta \log \mathcal{L}$ depends on particle momentum. Fig. 2.14 shows the efficiency (kaons identified as kaons) and pion misidentification (pions misidentified as kaons), as a function of particle momentum, obtained from imposing two different requirements on $\Delta \log \mathcal{L}_{K\pi}$. Requiring, for example, $\Delta \log \mathcal{L}_{K\pi} > 0$ and averaging over the momentum range $2 - 100$ GeV/c, the kaon efficiency and pion misidentification

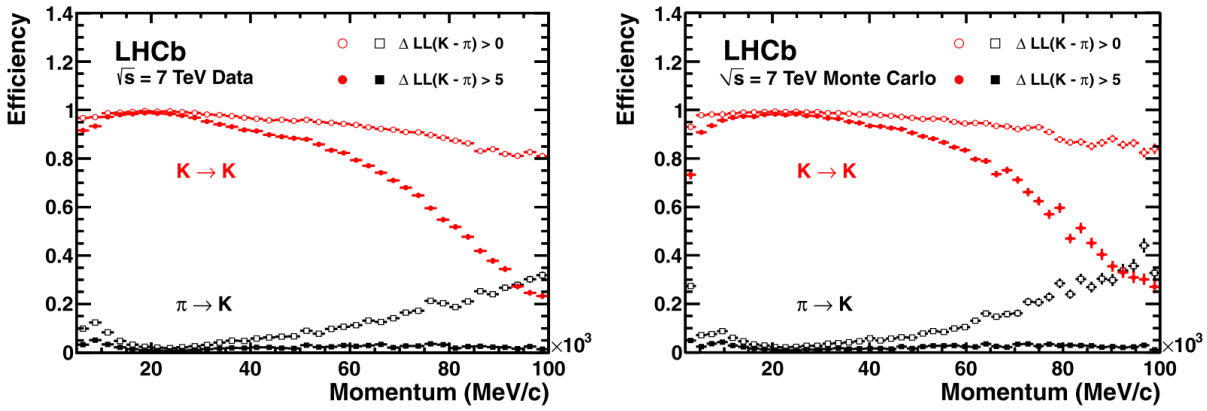

Figure 2.14: Kaon identification efficiency and pion misidentification rate measured on data (left) and using simulated events (right) as a function of track momentum. Two different $\Delta \log \mathcal{L}_{K\pi}$ requirements have been imposed on the samples, resulting in the open and filled marker distributions, respectively.

fraction are found to be $\sim 95\%$ and $\sim 10\%$, respectively. The alternative PID requirement of $\Delta \log \mathcal{L}_{K\pi} > 5$ illustrates that the misidentification rate can be significantly reduced to $\sim 3\%$ for a kaon efficiency of $\sim 85\%$ [35]. On the right of Fig. 2.14 the corresponding efficiencies and misidentification fractions in simulation are shown. The LHCb RICH detectors were designed to run with 0.6 interaction per bunch crossing. However the current operating conditions have 1.6 interaction per bunch crossing. The increased particle multiplicity provide an insightful glimpse of the RICH performance at high luminosity running. Fig. 2.15 shows the pion misidentification fraction versus the kaon identification efficiency as a function of track multiplicity and the number of reconstructed primary vertices.

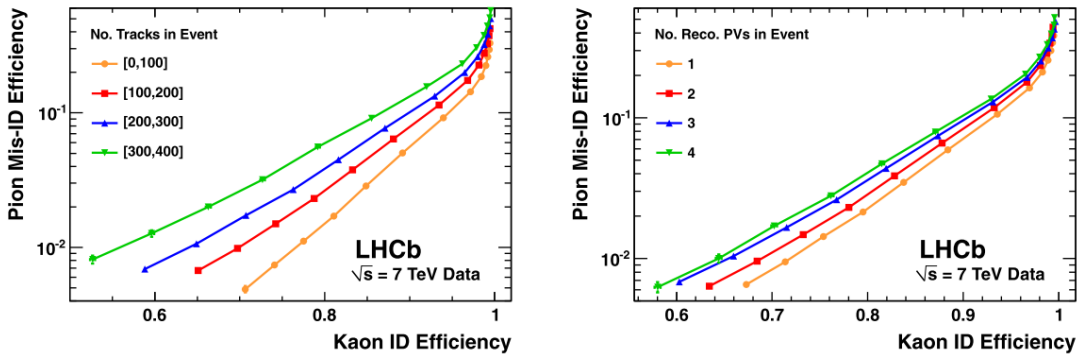

Figure 2.15: Pion misidentification fraction versus kaon identification efficiency as measured in 7 TeV LHCb collisions: on the left, as a function of track multiplicity, and on the right, as a function of the number of reconstructed primary vertices. The efficiencies are averaged over all particle momenta

2.5.2 The calorimeter system

The calorimeter system [36] performs several functions. It estimates the transverse energy E_T of hadron, electron and photon candidates* used by the first trigger level (L0) and it provides information used to discriminate between electrons, photons and hadrons as well as the measurement of their energies and positions. It is divided into four sub-detector:

- Scintillator Pad Detector (SPD);
- Pre-Shower (PS);
- Electromagnetic Calorimeter (ECAL);
- Hadronic Calorimeter (HCAL).

Each sub-detector is divided into regions where differently sized sensors are used. ECAL, PS and SPD are divided into three regions (inner, middle and outer as shown in Fig. 2.16) while HCAL is subdivided only into two regions. The size of sensor elements increases going far from the beam-pipe and the high occupancy region. Such choice is motivated by a compromise between occupancy (in order to guarantee a good resolution in energy and position of clusters) and the necessity to maintain a reasonable number of read-out channels. SPD and PS are auxiliary sub-detectors of ECAL and are placed before it. SPD is used to discriminate between charged and neutral particles, as the former ones produce light inside the scintillator layers while the latter do not. The PS is used for a better discrimination between electrons and pions both at the trigger level and in the offline reconstruction. Both sub-detectors consist of a scintillator plane and they are separated by a lead converter layer about 15 mm thick. The total material budget of the two sub-detectors corresponds to about 2.5-3 radiation lengths. The light produced inside the scintillator is collected, by wave length shifter (WLS) optical fibers, on multi-anode photo-multipliers.

The ECAL is a sampling calorimeter realized using Shashlik technology† and separated into different independent modules. It is composed of 66 lead converter layers (2 mm thick), each

*Transverse energy is defined as $E_T = E * sin\theta$ where E is the cluster energy in the calorimeter and θ is the polar angle of the cluster.

†Shashlik technology consist in the use of a pile of alternating slices of absorber and scintillator materilas.

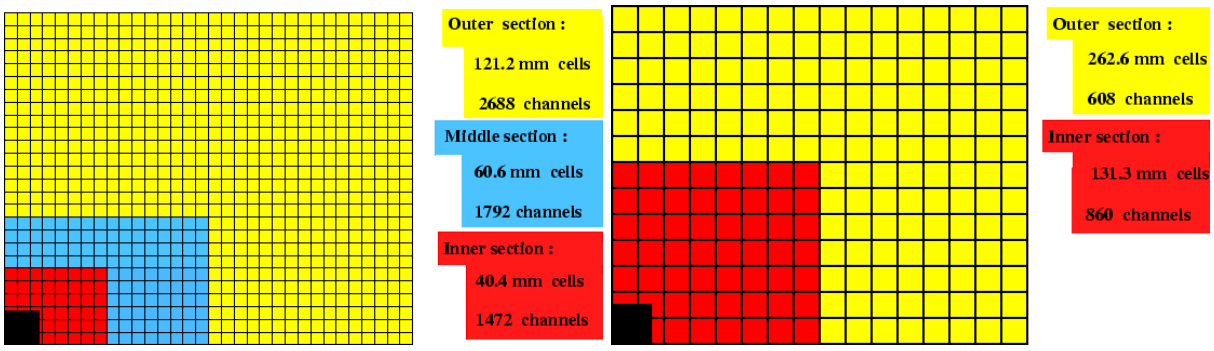

Figure 2.16: On the left: lateral segmentation of the SPD/PS and ECAL and, on the right, the HCAL. One quarter of the detector front face is shown. In the left figure the cell dimensions are also given for the ECAL.

one sandwiched between plastic scintillator layers 4 mm thick. The total material budget for each module is about 25 radiation lengths and 1.1 nuclear interaction lengths. The resolution provided on the measurement of photons and electrons energy is $\sigma(E)/E = 10\%/\sqrt{E} \oplus 1.5\%$ where E is given in GeV.

The optical fibers WLS cross longitudinally the entire module and bring light to the read-out photo-multipliers situated in the backward part of the module. Sizes and number of read-out channels of modules for different regions are different: the inner region has modules with a section of 4×4 cm^2 with 9 read-out channels per module; the middle region has modules of 6×6 cm^2 with 4 channels each; finally the outer region has 12×12 cm^2 modules with one channel each.

The hadronic calorimeter HCAL has as main purpose the measurement of energies of hadronic showers that is the main information needed by the Level-0 hadronic trigger. Its structure is similar to ECAL, but each module is built by layers of scintillator material 4 mm thick separated by layers of steal 16 mm thick. The total material budget corresponds to 5.6 nuclear interaction lengths. Module sizes are bigger than for ECAL and only two regions are defined: inner and outer (see Fig. 2.16). In the inner region modules are 13×13 cm^2, while in the outer region are 26×26 cm^2. The energy resolution is $\sigma(E)/E = 80\%/\sqrt{E} \oplus 10\%$ where E is given in GeV.

2.5.3 Muon detectors

Muons with high p_T and large impact parameter with respect to the primary vertex are a very clean signal for triggering events with B-hadrons. Such muons are also used in the flavour tagging algorithm to identify the flavour of the spectator B-hadron produced associated to the signal B-hadron. Muons are even present as final products in various core analyses of LHCb, like $B^0 \to \mu^+\mu^- K^{*0}$ and $B_{s,d} \to \mu^+\mu^-$ decays.

The muon detector [37] is composed of five stations (M1-M5), covering an angular acceptance of ± 300 mrad in the horizontal plane and ± 200 mrad in the vertical plane, corresponding to a geometrical efficiency of about 46% for the detection of muons coming from B-hadrons. The first muon station M1 is placed before the calorimeter system in order to avoid possible multiple scattering effects from the calorimeter material budget, that can modify the muon trajectory. M2-M5 are placed after the hadronic calorimeter and are separated by iron planes 80 cm thick, as depicted in Fig. 2.17.

Each muon station is subdivided into four regions (R1-R4) with increasing distance and segmentation from the beam-pipe, in a ratio of $1:2:4:8$ (see Fig. 2.18). With this geometry the charged particle occupancy is expected to be more or less the same in each region. Multi-Wire Proportional Chambers (MWPC) are used for all regions except the inner region of station M1 where the expected particle rate exceeds safety limits for ageing. In this region triple-GEM (Gas Electron Multiplier) detectors are used. MWPC have a structure with four overlapped gaps, in order to increase the detection efficiency for the single hit, each one 5 mm thick and with a distance between wires of about 2 mm (see Fig. 2.19). The total number of chambers used to build the muon detector is 1380. The triple-GEM detector consists of three GEM foils sandwiched between anode and cathode planes (see Fig. 2.19).

2.6 The LHCb trigger

The LHCb trigger [38] is required to be very efficient in accepting signals, rejecting most of the background events. The only way to achieve the required efficiency and purity of the stored

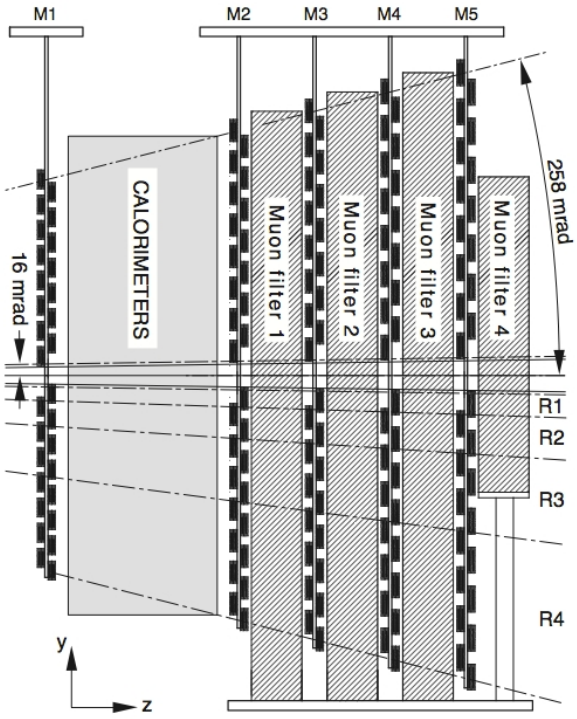

Figure 2.17: Scheme of the muon system from a side view.

sample is to subdivide the trigger system into different levels. The LHCb trigger system is

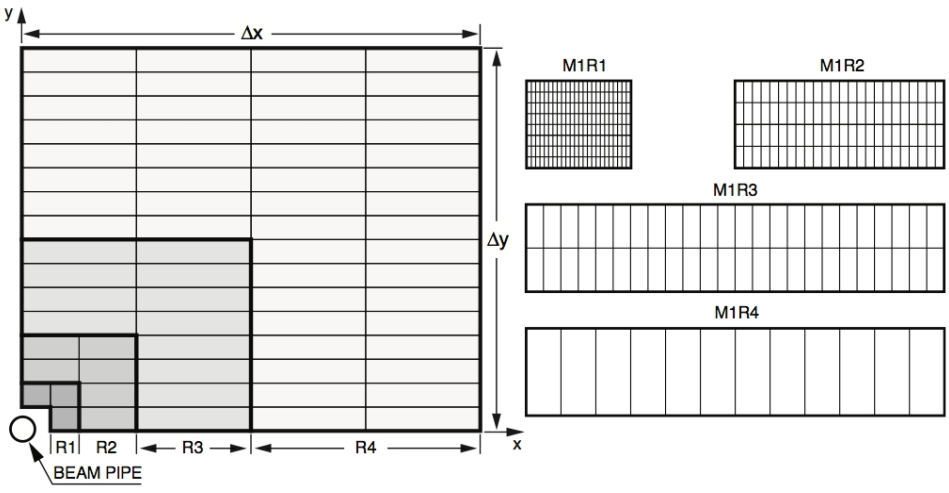

Figure 2.18: On the left: front view of a quadrant of a muon station. Each rectangle represents one chamber. Each station contains 276 chambers. On the right: division into logical pads of four chambers belonging to the four regions of station M1. In each region of stations M2-M3 (M4-M5) the number of pad columns per chamber is double (half) the number in the corresponding region of station M1, while the number of pad rows per chamber is the same.

divided into three levels, as shown in Fig. 2.20. The earliest trigger level (Level-0 or L0) is based on custom electronics and is designed to perform a first filtering, taking events with a maximum input rate of 40 MHz and sending them to the next trigger level at a maximum rate of about 1 MHz. Second (High Level Trigger 1 or HLT1) and third (High Level Trigger 2 or HLT2) trigger levels are software based and they perform a full reconstruction of the events on a dedicated computing farm. HLT1 filters heavy hadron events in an inclusive way and reduces the rate of accepted events to about 50 kHz. HLT2 is based on the same software used by HLT1 but it performs an exclusive selection of beauty and charm decays quite close to the final offline selections. The output of HLT2 is sent to mass storage at a rate of about 3 kHz.

2.6.1 The Level-0 Trigger

The L0 exploits fast detectors, able to provide valuable information without performing complicated reconstruction algorithms. The basic strategy is to measure transverse momentum of electrons, photons, hadrons and muons. The system utilises three independent systems running in parallel.

- **Electron/photon trigger**: it uses the electromagnetic calorimeter ECAL and the auxiliary PS and SPD detectors (to discriminate between charged and neutral particles). Custom electronic boards are programmed to measure energy of the electromagnetic showers, identifying those with highest transverse energy. An event is accepted if at least one cluster with transverse energy greater than a given threshold is present;

- **Hadronic trigger**: it uses the information of HCAL. It works like the electron/photon trigger, accepting events with at least one hadronic cluster with transverse energy higher than a given threshold;

- **Muon trigger**: it uses information coming from the hits in the five muon chambers. Muon segments are reconstructed dividing the muon chambers in fields of interest and connecting hits in the same field of interest from different chambers. The reconstructed tracks are then extrapolated to the proton-proton interaction region and a value for the transverse momentum of the muon is evaluated. Events are accepted if at least one muon

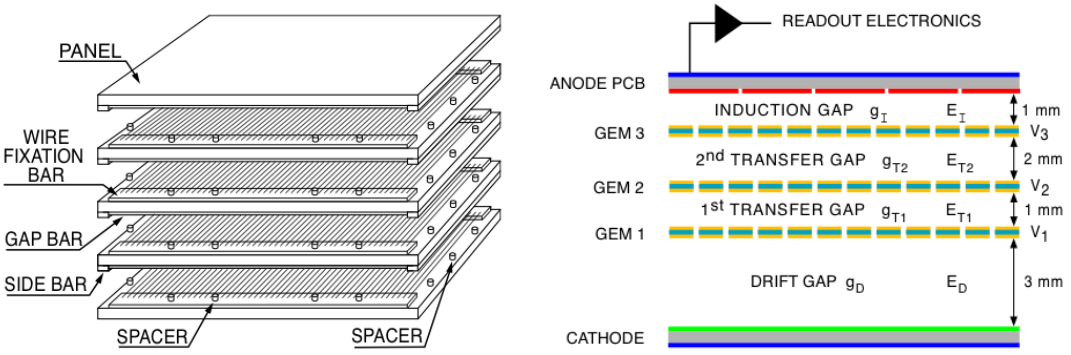

Figure 2.19: On the left: exploded schematic view of a MWPC showing the various elements. On the right: schematic cross section of a triple-GEM detector showing the most relevant elements and dimensions.

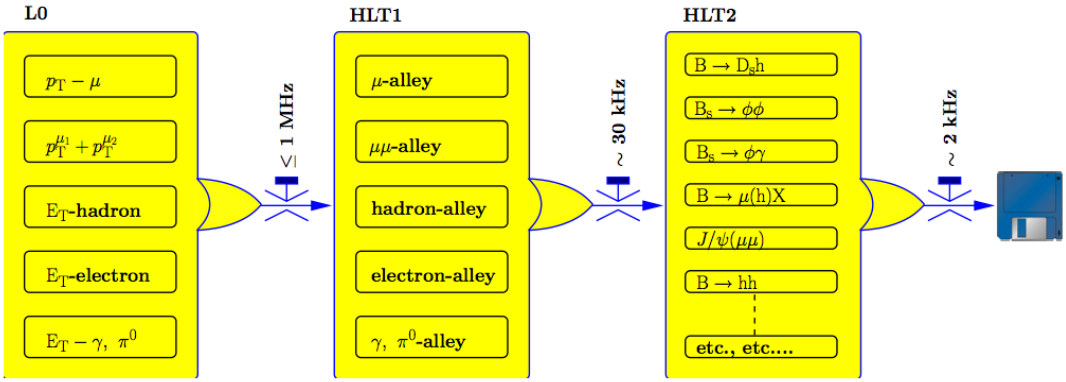

Figure 2.20: Structure of the LHCb trigger. The L0, HLT1 and HLT2 with their output rates are reported.

candidate has a transverse momentum greater than a threshold. An algorithm allowing to select muon pairs is also used, asking for muon pairs with the product of transverse momentum exceeding a given threshold.

Data taking conditions during 2011 and 2012 have been quite different from what planned during the design phase. In particular the mean number of interactions per bunch crossing has been approximatively four times the design level. This brought an increase in the number of primary vertices and tracks in each event. In addition the event size to be transferred to the second trigger level resulted to be higher. As a consequence both online and offline reconstruction and the data transfer timing for high occupancy events overcame the capabilities of the DAQ and of the offline reprocessing of LHCb. In order to cope with these difficulties a system to reject high occupancy events has been developed at the L0 trigger level. The very fast response of SPD detector allows to use it to roughly estimate the number of charged particles in the event satisfying the timing requirements of the Level-0 trigger. Events are accepted only if the number of hits in the SPD is less than 600. The final trigger decision is taken by an electronic module name *L0 Decision Unit*, that collects all the information and performs the OR of the three subsystem decisions. Events are accepted when at least one of the subsystems gives a positive decision.

2.6.2 The High Level Trigger

For events passing the Level-0 trigger, the full set of detector information is transferred to the Event Filter Farm (EFF), composed of about 1000 multi-core computing nodes, where the High Level Trigger (HLT) is run. The HLT is a software based C++ application performing a fast full reconstruction of events. Up to about 26000 copies of online reconstruction applications can run concurrently in the EFF. The HLT is divided in two steps: HLT1 and HLT2.

HLT1

Before the track reconstruction of the event is performed, the HLT1 algorithm makes a first selection of events based on the detector occupancy. Events with high occupancy (especially in the OT sub-detector) could take much more than the average allowed processing time of ~ 25 ms to be reconstructed. Thus events with OT occupancy larger than 20% are rejected, allowing to

avoid the throttling of the HLT process with a small loss in efficiency. For remaining events the reconstruction strategy is a consequence of the following considerations:

- High mass of B hadrons and their production processes imply that the particles coming from B hadron decays have a large momentum (p) and transverse momentum (p_T) compared with light-quark hadrons originating from the primary vertex (PV);
- The average decay length of B hadrons produced in the LHCb acceptance is ~ 1 cm so that their decay products will have a large impact parameter (IP) with respect to their PV.
- each B hadron decay has at least one final state particle characterized by large p, p_T and IP;
- the VELO reconstruction is fast enough to allow a full 3D pattern recognition and PV finding to be performed for all events entering the HLT;
- the full reconstruction can be performed only for a limited number of tracks due to limited time.

The last two points bring to the choice of subdividing the reconstruction into two steps. In the first step VELO tracks and PV are reconstructed. VELO tracks are selected asking for large impact parameters with respect to the closest PV and for a minimum number of hits in the VELO. In order to kill as much as possible ghost tracks the expected number of hits in the VELO for each track is performed considering the track direction and its first hit in the detector. If the difference between the expected number of hits and the number of hits used to reconstruct the tracks is greater than a certain threshold the track is rejected. Cut values changed several times during 2010 but during 2011 they have been stable. As a reference the cut values used in the 2011 trigger are: $IP > 125$ μm, number of hits greater than 9 and difference between expected and observed hits less than 3. The number of VELO tracks selected by this first step allows to perform the full forward reconstruction without exceeding the timing limit. Forward reconstructed tracks are then selected asking for minimal p and p_T requirements further reducing their number. Remaining tracks are then fitted using a bi-directional Kalman filter with outlier removal, in order to obtain an offline-quality value for the track χ^2 as well as an offline-quality covariance matrix at the first state of the track, allowing a cut on the IP significance squared ($\chi^2(IP)$). Cut on $\chi^2(IP)$ is very efficient in rejecting background from the primary vertex and track χ^2 is a powerful discriminating variable against ghosts.

HLT2

The lower input rate to HLT2 allows to perform the bi-directional Kalman filter on all the tracks in the event passing a minimal requirement of $p > 5$ GeV/c and $p_T > 0.5$ GeV/c. In this way it is possible to proceed to the full reconstruction of beauty and charm hadron decays with an almost offline-like reconstruction quality. HLT2 filtering is mainly based on three inclusive selections, so-called topological lines. In addition few dedicated lines for the core analyses of LHCb are used.

The main strategy of topological line is to build multibody candidates in the following way: two input particles are combined to form a two-body object; another input particle is added to the two body object to form a three-body object, and so on; the kaon mass hypothesis is assigned to all particles. Thus an n-body candidate is formed combining a $(n-1)$-body candidate and a particle (saving CPU time with respect to combining directly n particles). Only a particle

satisfying a cut on the distance of closest approach ($DOCA$) can be added to form a $(n+1)$-body candidate. When a 2-body object is built, a $DOCA < 0.15$ mm cut is imposed for the object to either become a 2-body candidate or to become the seed for a 3-body candidate. When a 3-body object is made by combining a 2-body object and another particle, another $DOCA < 0.15$ mm cut is imposed for the object to either become a 3-body candidate or input to a 4-body candidate. This DOCA is computed between the 2-body object and the additional particle, not among the three particles. This greatly enhances the efficiency of the HLT2 topological lines (in particular on $B \to DX$ decays) and saves CPU time. In addition to the topological lines, HLT2 contains a set of lines which exploit tracks which have been identified as muons. Dimuon candidates are formed and, depending on their mass, cuts are applied on the flight distance and p_T of the dimuon candidate. Single muon candidates are accepted either requiring large p_T, or a combination of $\chi^2\,(IP)$ and p_T cuts.

2.7 Computing

The availability of computing resources is a key factor in a modern High Energy Physics experiment. The amount of data delivered by LHC and thus collected by the experiment can not be processed inside one computing centre alone but must be distributed to various storage centres, to guarantee the possibility to have various backup copies of data. The baseline LHCb computing model is based on a distributed multi-tier regional centre model denominated WLCG [39] and it's centrally controlled by a specifically version of DIRAC [40] framework (Distributed Infrastructure with Remote Agent Control), designed for the LHCb collaboration. The principal DIRAC functionalities are the Workload Management System (WMS), the Data Management System (DMS) and the Transformation Management System (TMS). WMS exploit the now widely used concept of Pilot Agents, allowing an efficient allocation of computing resources. DMS manage in a versatile way the routine distribution tasks. TMS is built on top of the Workload and Data Management services, providing an automated data driven submission of processing jobs. A workload monitoring service allows an on-time monitoring of resource usage and of storage system status. The raw data coming out of the trigger system are transferred to the CERN Tier 0 centre for further processing and archiving. At this level data contain only the information of the detector itself, like hits in the tracking system, response of the calorimeter read-out, the hits on the HPD plane of the RICH system and are denominated RAW data. From the Tier-0 storage RAW data are copied to different Tier-1's where they will be processed. Data are transferred dependently on the available storage at the various Tier-1's. The next stage consists in data reconstruction, where RAW files are processed downloading them directly to the worker node where the process will run. Reconstruction consists in providing physical quantities out of the detector information: track trajectories and momentum, primary vertex coordinates, energy of calorimeter clusters, mass-hypothesis likelihood for the tracks. The output of the reconstruction phase is a new data type, the so called *Data Summary Tape* (DST). The pattern recognition algorithms in the reconstruction program make use of calibration and alignment constants to correct for any temporal changes in the response of the detector in its electronics and in its movements. Such information are stored into distributed databases, continuously updated by online monitoring of detector response. The computing model plan periodical reprocessings of collected data during the year, in order to utilise more precise calibration and alignment information obtained from off-line reprocessed data.

The next stage of the computing system consists of a preselection of events named *Stripping*. The output of this stage will be used for the physics analysis, thus is necessary to maintain it available on disk. The amount of disk space required by the full LHCb data sample would be

too much expensive. In addition the fraction of events useful for each single analysis inside the total sample is very small. Thus the stripping stage runs loose selections on the collected data sample, filtering the sample and creating the candidates that will be used in the final analysis. The events that pass the selection criteria will contain the candidates, the information of the reconstruction phase and also the RAW data relative to each event, in order to have as detailed event information as needed for the analysis. Stripping selections are divided into physics macro areas of interest denominated *streams* (BHADRON, LEPTONIC, CHARM, ...). As the stripping output file could contain very few selected events, files are merged up to a dimension of about 5 GB for each final merged DST. The *stream* separation facilities also the access to interesting events.

For what concerns simulated data, the processing phases are the same described above, but with small differences. Simulated RAW data (MC-RAW) are produced from a detailed description of the LHCb detector incorporating the current best understanding of detector response, trigger response and dead material. MC-RAW data contain simulated hit information and extra "truth" information. The truth information is used to record the simulated particles in the event and their relationship with hits in the detector. Such truth information are carried through all the processing step in order to use it during final analysis. The main difference with respect to real data is that trigger and stripping responses are just used to flag events, without rejecting them in case of non affirmative answer from selection algorithms. In order to save storage space also production with trigger and stripping in *rejection* mode are planned. Another difference with respect to real data processing is that all the steps except *merging* are executed one after the other on the same worker node, saving the output of intermediate steps temporarily on the local worker node disk. Because of the presence of "truth" information inside the data, simulated files are bigger than real data files. As for real data processing, simulated data are produced almost continuously during the year, using updated information on detector response and alignment, stored inside distributed database. Final DST's (both from real and simulated data) are meant for user analysis, thus they need to be stored on disk for a faster and more efficient access. RAW and DST files, instead, are transferred to magnetic tape support after the creation of the corresponding stripped DST in order to save disk space. In order to facilitate calibration, alignment and comparison of performance between different processings of data, at least the last two versions of stripped DST's are maintained available on disk. In Tab. 2.1 are reported the computing resources needed to process and store a single event at each step, as observed during the first half of 2011 activity.

Process	Data Type	CPU (HS06·s/evt)	Storage (kB/evt)
Data Taking	RAW	–	50
Reconstruction	DST	25	40
Stripping	DST	1.75	130
Simulation	DST	1700	400

Table 2.1: Computing resources needed for the processing of a single event at each step as observed during the first half of 2011.

Chapter 3

Measurement of the $\overline{B}^0 - B^0$ and $\overline{B}^0_s - B^0_s$ production asymmetries

In this chapter the analysis performed using data collected by LHCb during 2011 at the center of mass energy of 7 TeV and data collected during 2012 at the center of mass energy of 8 TeV is presented. We describe the measurements of the values of $A_{\rm P}\left(B^0\right)$ and $A_{\rm P}\left(B^0_s\right)$ obtained by measuring the oscillations of B^0 and B^0_s mesons with a time-dependent analysis of the $B^0 \to J/\psi(\mu^+\mu^-)K^{*0}(K^+\pi^-)$, $B^0 \to D^-(K^+\pi^-\pi^-)\pi^+$ and $B^0_s \to D^-_s(K^+K^-\pi^-)\pi^+$ decay rates. The measurements are performed as a function of transverse momentum, $p_{\rm T}$, and pseudorapidity, η, of the B^0 and B^0_s mesons within the LHCb acceptance, and then integrated over the range $4 < p_{\rm T} < 30\,{\rm GeV}/c$ and $2.5 < \eta < 4.5$.

3.1 Event selection

3.1.1 Stripping

The events $B^0 \to J/\psi\, K^{*0}$ are those selected with the `BetaSBd2JpsiKstarDetached` stripping line. This stripping line implements a selection based on the reconstruction of $J/\psi \to \mu^+\mu^-$ and $K^{*0} \to K^+\pi^-$ decays. The J/ψ candidates are reconstructed from two oppositely charged tracks, identified as muons, having $p_{\rm T} > 500\,{\rm MeV}/c$ and originating from a common vertex. The invariant mass of this pair of muons must lie in the range $3030 - 3150\,{\rm MeV}/c^2$. The K^{*0} candidates are reconstructed starting from two oppositely charged tracks, one identified as a kaon and the other as a pion, originating from a common vertex. It is required that the K^{*0} candidate has $p_{\rm T} > 1\,{\rm GeV}/c$ and that the invariant mass lies in the range $826 - 966\,{\rm MeV}/c^2$.

The B^0 candidates are reconstructed from the J/ψ and K^{*0} candidates, with the invariant mass of the $\mu^+\mu^-$ pair constrained to the J/ψ mass. They are required then to have an invariant mass in the range $5150 - 5400$ MeV/c^2. The decay time of each B^0 candidate is calculated from a vertex and a kinematic fit that constrains the candidate to originate from its associated PV. The χ^2 per degree of freedom of the fit is required to be less than 10. Only B^0 candidates with a decay time greater than 0.2 ps are retained. This lower bound on the decay time rejects a large fraction of the prompt combinatorial background.

In the cases of the $B^0 \to D^-\pi^+$ and $B^0_s \to D^-_s\pi^+$ decays, the stripping line is the `B02DPiD2HHHBeauty2Charm` and the selection of the B-meson candidates are based on the reconstruction of $D^- \to K^+\pi^-\pi^-$ and $D^-_s \to K^+K^-\pi^-$ decays, respectively. Requirements are made on the D^- and D^-_s decay products before combining them to form a common vertex. The scalar $p_{\rm T}$ sum of the tracks must exceed $1.8\,{\rm GeV}/c$ and the maximal distance of closest approach

between all possible pairs of tracks must be less than 0.5 mm. The $D^-_{(s)}$ candidate is required to have a flight distance with respect to the associated PV with a χ^2 greater than 36 compared to the zero distance hypothesis. The masses of the D^- and D^-_s candidates must lie within $1850 - 1890\,\mathrm{MeV}/c^2$ and $1949 - 1989\,\mathrm{MeV}/c^2$, respectively. They are subsequently combined with a fourth particle, the bachelor pion, to form the B-meson decay vertices. The sum of the $D^-_{(s)}$ and bachelor pion p_T values must be larger than $5\,\mathrm{GeV}/c$ and the decay time of B-meson candidates must be greater than 0.2 ps. The cosine of the angle between the B-meson candidate momentum vector and the line segment between the PV and B-meson candidate vertex is required to be larger than 0.999.

3.1.2 Offline selection

An offline selection is applied to the events that pass the stripping line to further refine the sample purity. The offline selection consists in particle identification (PID) cuts, performed in order to reduce the misidentified backgrounds and a kinematic selection based on a multivariate analysis method to reduce the combinatorial background.

PID requirements

The $B^0 \to J/\psi\, K^{*0}$ candidates that pass the `BetaSBd2JpsiKstarDetached` line are required to satisfy the following particle identification (PID) requirements: $\Delta \ln \mathcal{L}_{K\pi} > 2$ to identify kaons and $\Delta \ln \mathcal{L}_{K\pi} < -2$ to identify pions. In the cases of the $B^0 \to D^-\pi^+$ and $B^0_s \to D^-_s\pi^+$ candidates, PID requirements are applied to those that pass the `B02DPiD2HHHBeauty2Charm` line in order to reduce to a negligible level misidentified backgrounds which may peak in the B mass region.

The main misidentified backgrounds for the $B^0 \to D^-\pi^+$ decays are due to the $\bar{\Lambda}^0_b \to \Lambda^-_c\pi^+$ decays, where the antiproton from the $\Lambda^-_c \to \bar{p}K^+\pi^-$ decay is misidentified as a pion, and to the $B^0_s \to D^-_s\pi^+$ decay, where the K^- from $D^-_s \to K^+K^-\pi^-$ is misidentified as pion. To reject these backgrounds the following PID requirements are applied:

- $\Delta \ln \mathcal{L}_{\mathrm{p}\pi} < -5$ for the pion candidates, when the invariant mass of D^- candidates, computed under the $\bar{p}K^+\pi^-$ mass hypothesis, lies within the window 2250–2315 MeV/c^2. This request is applied only to the pion candidates forming the D^- candidate, which have the same charge of the misidentified antiproton fron Λ^-_c.

- $\Delta \ln \mathcal{L}_{K\pi} < -2$ for the pion candidates, when the invariant mass of D^- candidates, computed under the $K^+K^-\pi^-$ mass hypothesis, is less then 2000 $\mathrm{MeV/c^2}$. As in the previous case this requirement is applied only to candidate pions forming the D^- candidate, which have the same charge of the misidentified kaon from D^-_s.

Figure 3.1 shows the invariant mass distribution of D^- candidates reconstructed under the $\bar{p}K^+\pi^-$ and $K^+K^-\pi^-$ mass hypotheses, with and without the PID requirements.

An additional source of background is the $B^0 \to D^-K^+$, where the K^+ is misidentified as a pion. To suppress this background we require $\Delta \ln \mathcal{L}_{K\pi} < -3$ for the bachelor π. In addition, we apply a requirement on the invariant mass of the D^-, which must lie within the window 1850–1890 MeV/c^2, corresponding to $\pm 20\,\mathrm{MeV}/c^2$ of the D^- nominal mass.

In the case of the $B^0_s \to D^-_s\pi^+$ decay, the main backgrounds are the $B^0 \to D^-(K^+\pi^-\pi^-)\pi^+$, where the pion from the D^- is misidentified as a kaon, the $B^0_s \to D^-_s K^+$ decay, where the kaon is misidentified as a pion, and the $\bar{\Lambda}^0_b \to \Lambda^-_c(\bar{p}K^+\pi^-)\pi^+$ where the antiproton from Λ^-_c is

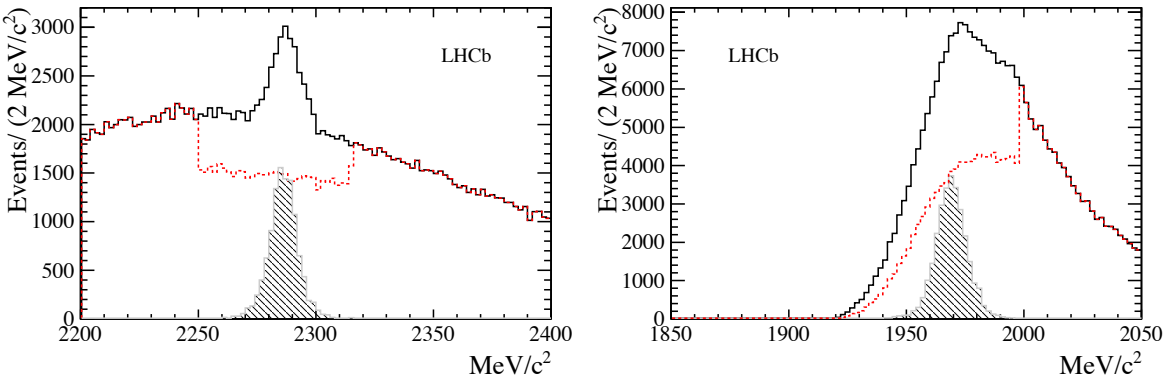

Figure 3.1: Invariant mass distribution of $D^- \to K^+\pi^-\pi^-$ offline selected candidates computed under the (left) $\bar{p}K^+\pi^-$ and (right) $K^+K^-\pi^-$ mass hypothesis, with (dashed red line) and without (solid black line) the PID requirement to reject protons and kaons. The Monte Carlo invariant mass distribution (hatched histogram) for $\Lambda_c^- \to \bar{p}K^+\pi^-$ (left) and and $D_s^- \to K^+K^-\pi^-$ (right) are also shown in arbitrary scale as a reference. The discrete jumps in the two invariant mass spectra are due to the fact that the PID requirements are applied only in the relevant invariant mass windows to minimize the loss of signal events.

misidentified as a kaon or when the antiproton from Λ_c^- is misidentified as pion and the pion from Λ_c^- as kaon. To suppress these backgrounds, the following requirements are applied:

- $\Delta \ln \mathcal{L}_{K\pi} > 5$ for the kaon candidates, when the invariant mass of D_s^- candidates, computed under the $K^+\pi^-\pi^-$ mass hypothesis, is greater then 1830 MeV/c^2. This request is applied only to the kaon candidates with the same charge of the misidentified pion from D^-.

- $\Delta \ln \mathcal{L}_{K\mathrm{p}} > 10$ for the kaon candidates, when the invariant mass of D_s^- candidates, computed under the $\bar{p}K^+\pi^-$ mass hypothesis, lies within the window 2225–2315 MeV/c^2. As in the previos case the requirement is applied only to the kaons from D_s^+ with the same charge of misidentified proton from Λ_c^-.

- $\Delta \ln \mathcal{L}_{\pi\mathrm{p}} > 10$ for the pion candidates, when the invariant mass of D_s^- candidates, computed under the $\bar{p}K^+\pi^-$ mass hypothesis, lies within the window 2225–2315 MeV/c^2. This is applied only for the pion candidates which have the same charge of the misidentified proton from Λ_c^-.

Figure 3.2 shows the invariant mass distribution of D_s^- candidates, computed under the $K^+\pi^-\pi^-$ mass hypothesis, the $\bar{p}K^+\pi^-$ mass hypothesis when the antiproton from Λ_c^- is misidentified as kaon, and the $\bar{p}K^+\pi^-$ mass hypothesis when the proton is misidentified as pion and the pion from Λ_c^- as kaon.

An additional source of background is the $B_s^0 \to D_s^- K^+$, where the K^+ is misidentified as a pion. To suppress this background we require the condition $\Delta \ln \mathcal{L}_{K\pi} < -1$ for the bachelor pion. Additional requirements are applied to the invariant mass of D_s^- candidates, that has to lie within the window 1949–1989 MeV/c^2, corresponding to ± 20 MeV/c^2 around the D_s^+ nominal mass, and $\Delta \ln \mathcal{L}_{K\pi} > -3$ for kaons.

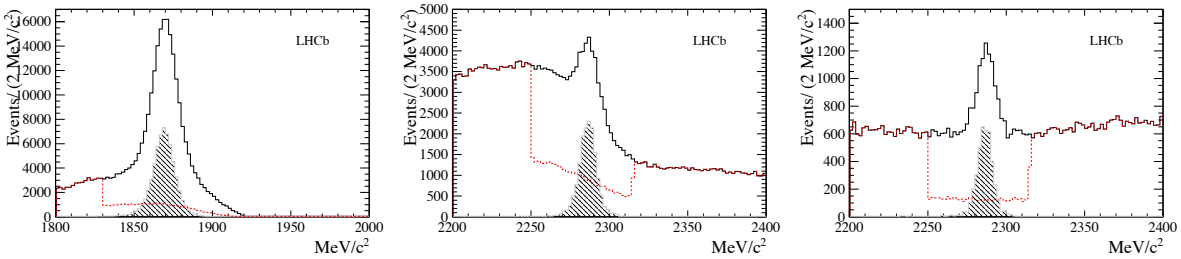

Figure 3.2: Invariant mass distribution of $D_s^- \to K^+K^-\pi^-$ offline selected candidates under (left) the $K^+\pi^-\pi^-$ mass hypothesis, (middle) the $\bar{p}K^+\pi^-$ mass hypothesis when the antiproton from Λ_c^- is misidentified as kaon, and (right) the $\bar{p}K^+\pi^-$ mass hypothesis when the antiproton is misidentified as pion and the pion from Λ_c^- as a kaon. The dashed red line and solid black line correspond respectively to the cases with and without PID requirements applied.

Multivariate analysis

A final selection is applied to the events that satisfy the preselection and PID criteria listed above. Three different selections are set and optimised to reject the combinatorial background: for the $B^0 \to J/\psi K^{*0}$ decay, for the $B^0 \to D^-\pi^+$ decay and for the $B_s^0 \to D_s^-\pi^+$ decay. All of them are based on a multivariate analysis method, namely the so-called `Boosted Decision Tree` (BDT) [42, 43]. The tuning of the BDT is performed into two steps. First the BDT algorithm is trained, to it to distinguish between signal and combinatorial background events. In order to achieve this goal, the algorithm utilises two data samples: one is composed of signal events from Monte Carlo and the other is composed of combinatorial background events from real data sidebands. After the training phase has been accomplished, the BDT can be used as a classifier to assign to each event a number ($\mu_{\rm BDT}$) ranging from -1 and $+1$. The separation between signal and background events is achieved by choosing an appropriate threshold for the index $\mu_{\rm BDT}$, which maximises a predefined score function. The variables used by the BDT classifier are the following:

- The transverse momentum ($p_{\rm T}^{\rm dau}$) and the impact parameter ($d_{\rm IP}^{\rm dau}$) of the B daughter particles J/ψ and K^{*0}, or D and π;
- The transverse momentum ($p_{\rm T}^{B}$), the distance of flight ($d_{\rm FL}^{B}$) and the impact parameter ($d_{\rm IP}^{B}$) of the B candidates.

The preselection and PID requirements as applied to the data are equally applied to simulated events passing the trigger requirements. The combinatorial background are isolated in real data by selecting the events sitting in the high invariant mass sidebands, defined as $5.31 < m < 5.34\,{\rm GeV}/c^2$ for the $B^0 \to J/\psi K^{*0}$ decay, $5.4 < m < 5.8\,{\rm GeV}/c^2$ for the $B^0 \to D^-\pi^+$ decays and $5.45 < m < 5.9\,{\rm GeV}/c^2$ for the $B_s^0 \to D_s^-\pi^+$ decay.

The optimisation of the BDT selection requires a preliminary knowledge of the relative proportions of signal and background candidates. We estimate the signal and background components of the data samples by performing an unbinned maximum likelihood fits to the mass spectra.

The signal and combinatorial background components determined from the fit for the 2011 and 2012 data samples are the following:

- $N_{\rm sig}^{J/\psi K^*} = 101\,032 \pm 809$, $N_{\rm bkg}^{J/\psi K^*} = 303\,187 \pm 926$;

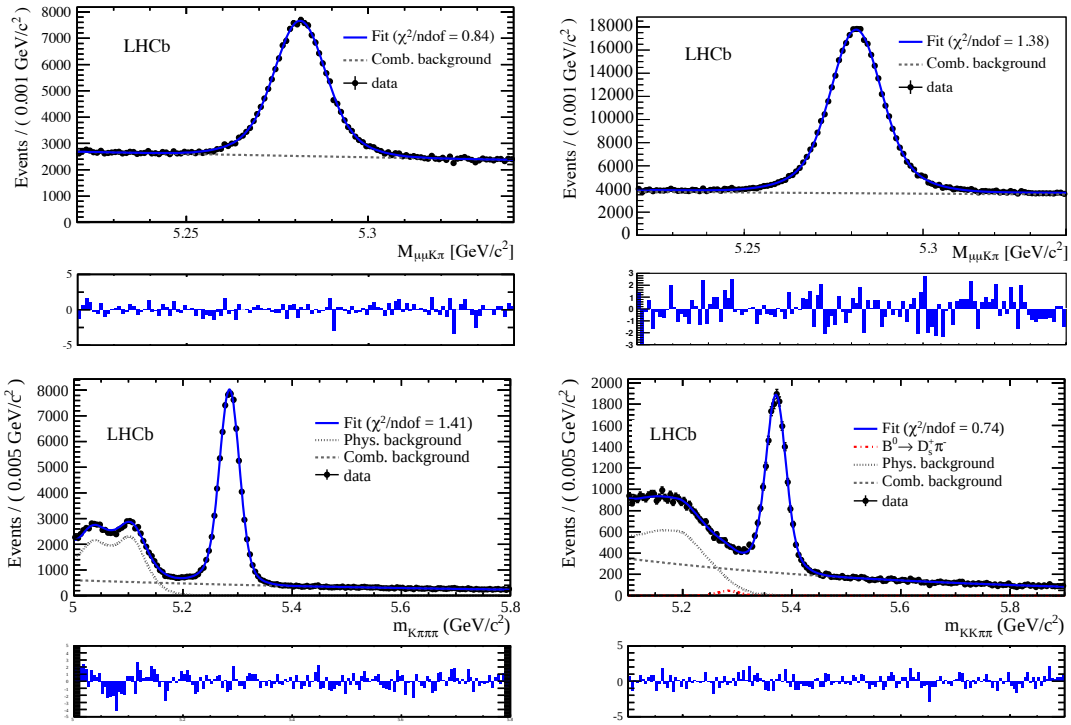

Figure 3.3: Invariant mass fits used for the relative normalization of signal and background yields in the BDT optimization: (top left) $B^0 \to J/\psi K^{*0}$ 2011 decays, (top right) $B^0 \to J/\psi K^{*0}$ 2012 decays, (bottom right) $B^0 \to D^-\pi^+$ decays and (bottom left) $B_s^0 \to D_s^-\pi^+$ decays.

- $N_{\rm sig}^{D^-\pi^+} = 77\,772 \pm 778$, $N_{\rm bkg}^{D^-\pi^+} = 62\,237 \pm 1458$;
- $N_{\rm sig}^{D_s^-\pi^+} = 17\,370 \pm 255$ and $N_{\rm bkg}^{D_s^-\pi^+} = 29\,723 \pm 652$.
- For the 2012 data, $N_{\rm sig}^{J/\psi K^*} = 276\,763 \pm 1\,171$, $N_{\rm bkg}^{J/\psi K^*} = 455\,018 \pm 1\,244$.

The fit is performed using a signal component parameterised as a double Gaussian convolved with a function with floating mean and width the radiative tail describing; the combinatorial background component is modeled using an exponential function. We have also taken into account a background component due to partially reconstructed B decays for the $B_{(s)}^0 \to D_{(s)}^-\pi^+$ decay modes. The shapes has been parameterised by means of a kernel estimation technique, obtained from the simulated samples, generated in the exclusive modes $B^0 \to D^{*-}\pi^+$, $B^0 \to D^-\rho^+$, $B_s^0 \to D^{*-}{}_s\pi^+$ and $B_s^0 \to D_s^-\rho^+$. The Monte Carlo events are selected with the same selection applied to the data. The true value of the invariant mass is smeared by a Gaussian resolution model, obtained by a fit to the data where the partially reconstructed backgrounds were excluded from the mass window. Figure 3.3 shows the invariant mass spectra after applying the preselection and the PID requirements on data, with the results of the fits superimposed, for $B^0 \to J/\psi K^{*0}$, $B^0 \to D^-\pi^+$ and $B_s^0 \to D_s^-\pi^+$ decays. A detailed discussion of the parameterisation used after the BDT is applied, in order to describe the resulting final spectra, can be found in Sec. 3.3.

The data samples available are split into two halves, the first half as explained above is used for the training phase of the BDT, the second is used to test the presence of possible

overtraining effects and to define the optimal requirements on the selection index returned by the BDT classifier $\mu_{\rm BDT}$. Figure 3.4 shows the distributions of $\mu_{\rm BDT}$ for signal and background events. The good agreement between the reference distributions, achieved with the training sample, and the test events, witnesses the good behavior of the classifier, since of the absence of overtraining effects.

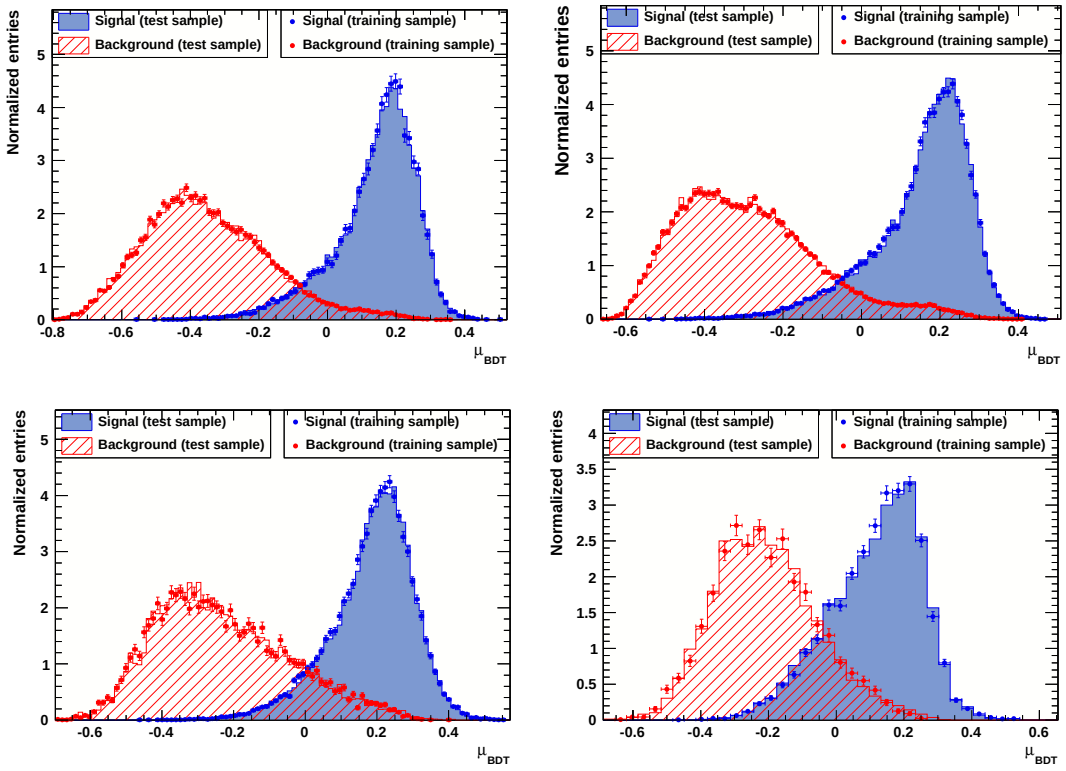

Figure 3.4: Distributions of $\mu_{\rm BDT}$ for signal and background events: (top left) $B^0 \to J/\psi K^{*0}$ 2011 decays, (top right) $B^0 \to J/\psi K^{*0}$ 2012 decays, (bottom left) $B^0 \to D^-\pi^+$ decays and (bottom right) $B_s^0 \to D_s^-\pi^+$ decays. The dots correspond to the training samples, while the filled histograms correspond to the test samples.

The optimal requirements on $\mu_{\rm BDT}$ for each decay mode are set by maximising the quantity $\xi = S/\sqrt{(S+B)}$, where S and B represent the number of signal and combinatorial background events, with an invariant mass in the window of $\pm 3\sigma$ centered around the B^0 or B_s^0 masses. Figure 3.5 shows ξ calculated for the events satisfying the requirement $\mu_{\rm BDT} > \hat{\mu}$, i.e. ξ as a function of $\hat{\mu}$. It turns out that the maximum value of ξ is $\mu_{\rm BDT} > -0.01$ in the cases of the $B^0 \to J/\psi K^{*0}$ and $B^0 \to D^-\pi^+$ decays, it is $\mu_{\rm BDT} > -0.02$ in the case of the $B_s^0 \to D_s^-\pi^+$ decay.

From Fig. 3.5 it is clear that the BDT selection leads to a sizable improvement in the value of ξ for the $B^0 \to J/\psi K^{*0}$ decay, while for the $B^0 \to D^-\pi^+$ and $B_s^0 \to D_s^-\pi^+$ decays the improvement is very mild: it means that the preselection requirements used to select these two decays are tight enough to reject most of the combinatorial background.

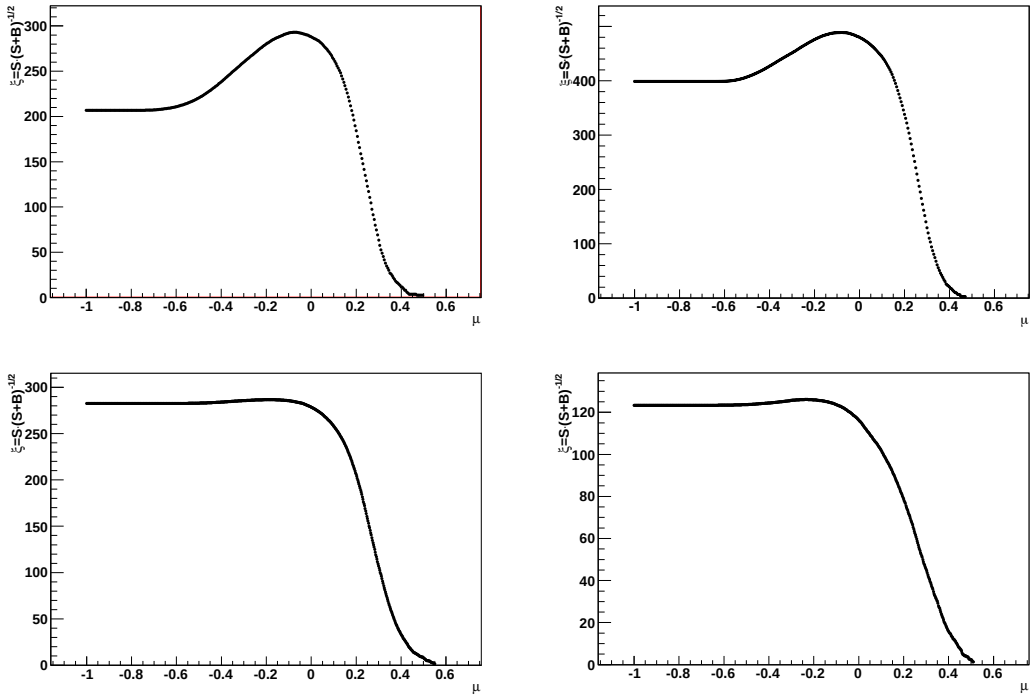

Figure 3.5: Dependence of $\xi = S/\sqrt{(S+B)}$ as a function of the requirement $\mu_{\rm BDT} > \hat{\mu}$: (top left) $B^0 \to J/\psi K^{*0}$ 2011 decays, (top right) $B^0 \to J/\psi K^{*0}$ 2012 decays, (bottom left) $B^0 \to D^-\pi^+$ decays and (bottom right) $B_s^0 \to D_s^-\pi^+$ decays.

3.2 Decay time resolution

We limit this study to the B_s^0, since in this case, the time resolution model has a non-negligible impact on the description of the decay time distribution, due to the fast B_s^0 oscillations. The accuracy on the decay time resolution of the B^0 decays plays instead a negligible role.

The strategy adopted to determine the B_s^0 decay time resolution relies on the reconstruction of the decay time of "fake-B candidates". A fake-B is formed starting from a $D^\pm$, decaying to $K^\mp\pi^\pm\pi^\pm$, and a pion bachelor track, where both the $D^\pm$ and the pion are coming from the same PV. The bachelor pion is selected such not to bias the decay time, hence only requirements on momentum and transverse momentum of the pion have been applied, avoiding the usage of impact parameter variables. The decay time distribution of the fake-B candidates yields an estimation of the decay time resolution measured on real $B_s^0 \to D_s^-\pi^+$ decays.

This study is performed using $1\,\text{fb}^{-1}$ of 2011 data, filtered by a dedicated stripping line `UnbiasedB2DPiWithUnbiasedB2DPi`, which is unbiased since it does not apply any requirement on the impact parameters nor on the decay time. In addition to the selection operated by the stripping line, further selection requirements are applied as described below:

- The $p_{\rm T}$ of fake-B candidates must exceed $2\,\text{GeV}/c$;
- The χ^2 of smallest impact parameters of the $D^\pm$ and of the bachelor pion must be less then 9;
- The χ^2 of the second smallest impact parameter χ^2 of the fake-B candidates must be

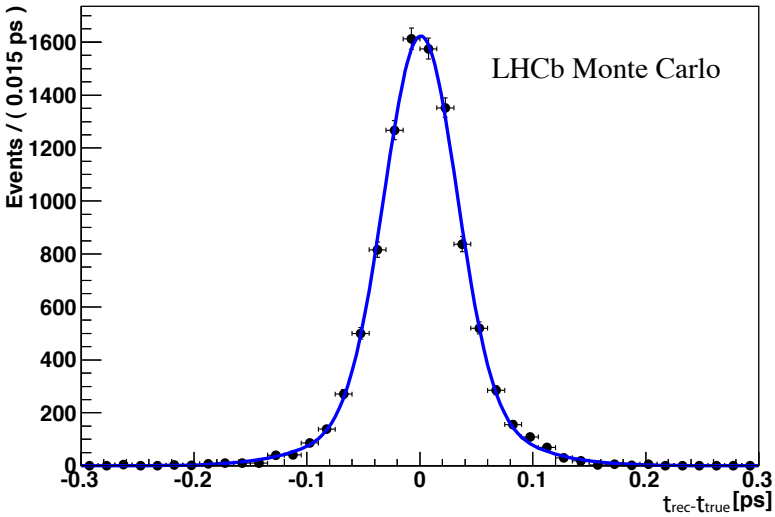

Figure 3.6: $B_s^0 \to D_s^- \pi^+$ decay time resolution, resulting from Monte Carlo simulated events. The values of the parameters obtained from the fit are reported in Table 3.1.

greater then 20.

These additional requirements are used to remove possible fake-B candidates (or rather, its daughters) with an erroneous association to the PV.

3.2.1 Validation of the method with simulated events

In order to validate the reliability of the method we use Monte Carlo simulated events. To evaluate the decay time resolution we use the entire selection chain to the $B_s^0 \to D_s^- \pi^+$ simulated data sample: applying the trigger, the preselection, and the PID and BDT event filtering stages. Figure 3.6 shows the distribution of $t_{\rm rec} - t_{\rm true}$, where $t_{\rm rec}$ is the reconstructed B_s^0 decay time, while $t_{\rm true}$ is the B_s^0 true decay time. The result of the fit performed with a double Gaussian resolution model function (with common mean) is overlaid to the data.

Making use of the stripping line `UnbiasedB2DPiWithUnbiasedB2DPi` and of the additional requirements mentioned above, we select a sample of fake-B candidates, corresponding to a Monte Carlo data sample of prompt $D^- \to K^+\pi^-\pi^-$ decays, and fit the decay time distribution by using the same double Gaussian function resolution model, as it is shown in Fig. 3.7.

In Fig. 3.8 the kinematic distributions in p, $p_{\rm T}$, η and azimuthal angle ϕ of the true B_s^0 mesons and fake-B to check whether they differ appreciably are plotted. The largest difference between the samples is observed for p and $p_{\rm T}$ distributions. In order to check whether such differences lead to any significant effect on the decay time resolution, the kinematics of the fake-B candidates such to match the true B_s^0 mesons at best are re-weighted. The weight of a given bin, to be applied as a correction to the fake-B distributions, is given by the ratio of the true $B_s^0 \to D_s^- \pi^+$ value, divided by the corresponding fake-B one. To account for correlations between p and $p_{\rm T}$, a two-dimensional weighting function for $(p, p_{\rm T})$ is used, whereas a one-dimensional weighting function is used for ϕ. The overall weighting function is obtained as the product of the two. Figure 3.9 shows the kinematic distributions after the re-weighting procedure has been applied.

By fitting the re-weighted distribution shown in Fig. 3.10 we observe a slight variation with

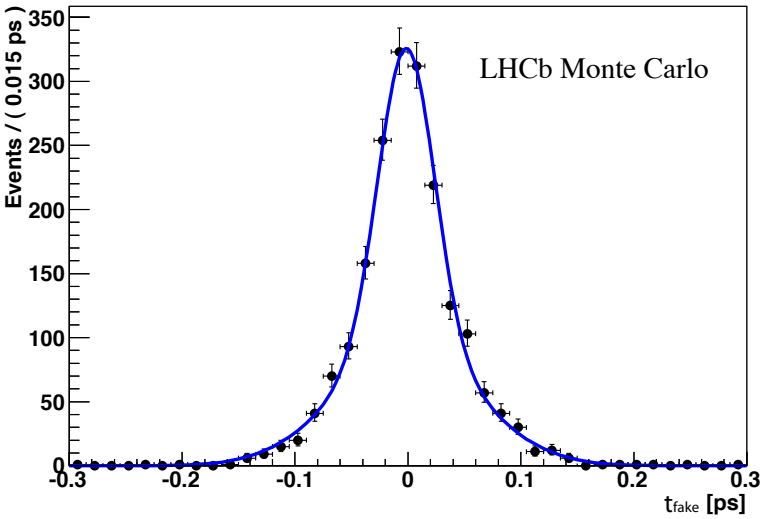

Figure 3.7: Decay time distribution from Monte Carlo fake-B candidates. The values of the parameters obtained from the fit are reported in Table 3.1.

Parameter [fs]	Signal MC	MC fake-B	MC fake-B re-weighted
μ	0.7 ± 0.4	-1.5 ± 0.9	-2.2 ± 0.9
σ_1	32 ± 1	25 ± 2	22 ± 2
σ_2	71 ± 2	62 ± 3	58 ± 2
f_1	0.79 ± 0.02	0.51 ± 0.06	0.44 ± 0.05
$\overline{\sigma}$ (average width)	43 ± 1	47 ± 1	46 ± 1

Table 3.1: Values of the double Gaussian parameters used to fit the decay time resolution for simulated signals, fake-B candidates and reweighted fake-B candidates. The average width is calculated as $\overline{\sigma} = \sqrt{f_1 \cdot \sigma_1^2 + (1 - f_1) \cdot \sigma_2^2}$ and error using a Monte Carlo propagation which takes into account the correlation among the parameters.

respect to the unweighted case, shown earlier in Fig. 3.7.

Table 3.1 summarises the values of the double Gaussian parameters returned by fit of the decay time resolution, in the three cases: of Monte Carlo signals, fake-B and re-weighted fake-B candidates. It is evident that the effects of the different kinematics implied in these processes is mild. In conclusion, it is not necessary to apply a re-weighting procedure: the the fake-B and the re-weighted fake-B time resolution differs only by a tiny amount, as much as 1 fs. The method used to determine the decay time resolution, relying on the fake-B candidates, slightly overestimates the decay time resolution of the B_s^0, by about 4 fs. This difference will be taken into account as a systematic effect.

3.2.2 Decay time resolution from data

In contrast to simulated events, in this case we need to disentangle prompt D^- mesons from delayed D^- mesons originated from B meson decays. The distribution of the logarithm of

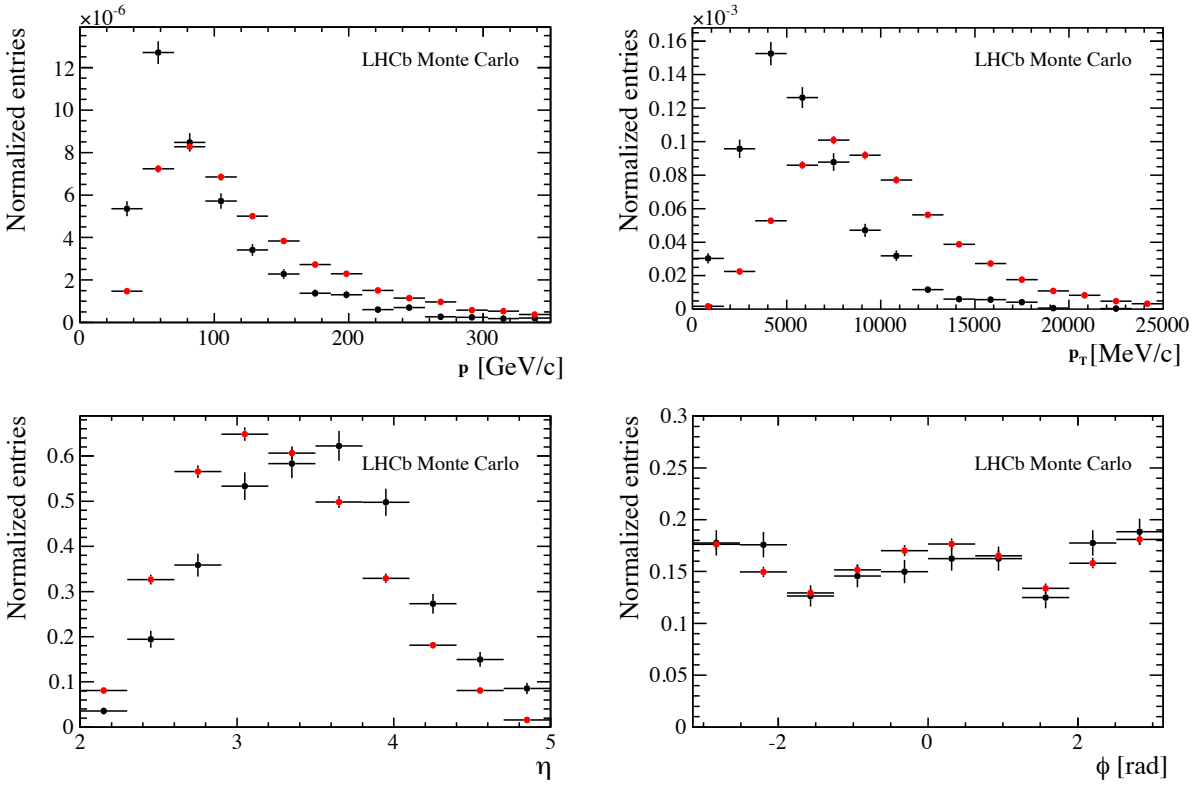

Figure 3.8: Simulated distributions of (top left) p, (top right) $p_{\rm T}$, (bottom left) η and (bottom right) ϕ distributions for (red dots) B_s^0 candidates decaying to $D_s^-\pi^+$ and (black dots) fake-B candidates.

the D-meson impact parameter, $\ln(\mathrm{IP_D})$, is known to significantly differ between prompt and secondary D^- mesons, hence it can be used to perform such a separation. From the data sample selected by the `UnbiasedB2DPiWithUnbiasedB2DPi` stripping line, by using the *sPlot* technique [41], applied to the $D^\pm$ invariant mass spectrum, we obtain a background-subtracted $D^\pm$ data sample that is shown in Fig. 3.11.

To evaluate the amount of a secondary (delayed) $D^\pm$ component, we compare the distribution of $\ln(\mathrm{IP_D})$ between the background-subtracted $D^\pm$ candidates and the simulated prompt $D^\pm$ candidates. Such a comparison is shown in Fig. 3.12, where the results of the fits performed using a `Bukin` function (see below) are overlaid. This distribution function of $\ln(\mathrm{IP_D})$, where x corresponds to $\ln(\mathrm{IP_D})$ and σ_p, ξ and $\rho_{1,2}$ are the free parameters to be determined, is defined as in the following. In the region $x < x_1$ and $x > x_2$ the function is:

$$f(x) = A\exp\left[\frac{\xi\sqrt{\xi^2+1}(x-x_1)\sqrt{2\ln 2}}{\sigma_p\left(\sqrt{\xi^2+1}-\xi\right)^2\ln\left(\sqrt{\xi^2+1}+\xi\right)} + \rho\left(\frac{x-x_i}{x_p-x_i}\right)^2 - \ln 2\right], \tag{3.1}$$

with $\rho = \rho_1$ and $x_i = x_1$ for $x < x_1$ and $\rho = \rho_2$ and $x_i = x_2$ for $x > x_2$.

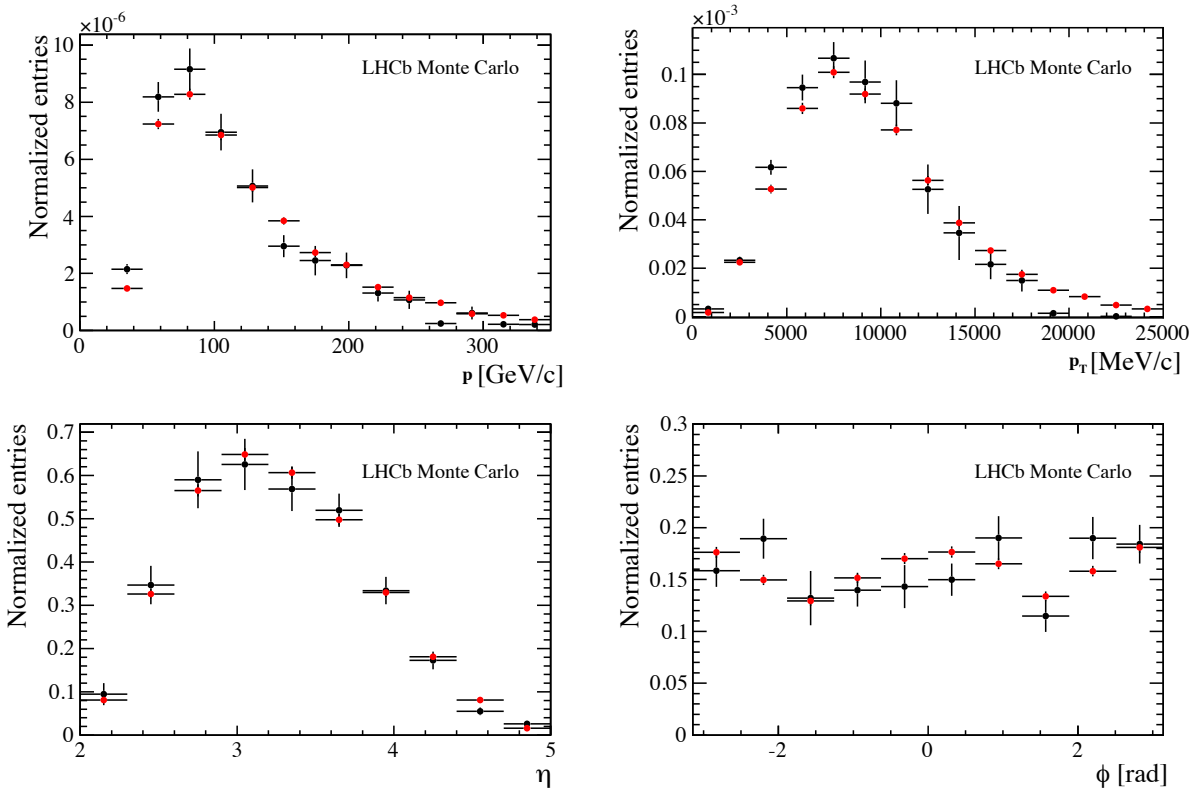

Figure 3.9: Simulated distributions of (top left) p, (top right) $p_{\rm T}$, (bottom left) η and (bottom right) ϕ distributions for (red dots) B_s^0 candidates decaying to $D_s^-\pi^+$ and (black dots) fake-B candidates. The re-weighting procedure described in the text has been applied.

Within the interval $x_1 < x < x_2$ the function is defined as:

$$f(x) = A \exp\left[-\ln 2 \left(\frac{\ln\left(1 + 2\xi\sqrt{\xi^2+1}\,\dfrac{x - x_p}{\sigma_p\sqrt{2\ln 2}}\right)}{\ln\left(1 + 2\xi^2 - 2\xi\sqrt{\xi^2+1}\right)} \right)^2 \right]. \tag{3.2}$$

here A is a normalisation factor.
The values of x_1 and x_2 are defined as:

$$x_{1,2} = x_p + \sigma_p\sqrt{2\ln 2}\left(\frac{\xi}{\sqrt{\xi^2+1}} \mp 1\right). \tag{3.3}$$

The values of the parameters governing the shape of the `Bukin` function obtained from the fits are reported In Table 3.2. There is no evidence of a secondary component in the fake-B candidates constructed with real data: the selection requirements applied to the impact parameters strongly suppress the $D^{\pm}$ secondary component.

The final resolution model adopte is a triple Gaussian function with common mean $\mu^{\rm res}$, widths $\sigma^{\rm res}_{1,2,3}$ and fractions of the first and second Gaussian $f^{\rm res}_{1,2}$ adapted by fitting the decay time distribution of fake-B candidates. Figure 3.13 shows the decay time distribution of the

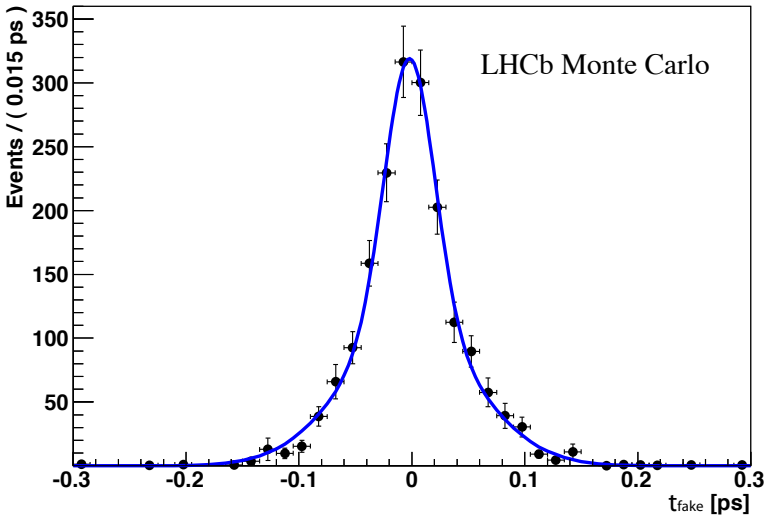

Figure 3.10: Decay time distribution for fake-B_s^0 candidates, once the re-weighting procedure is applied.

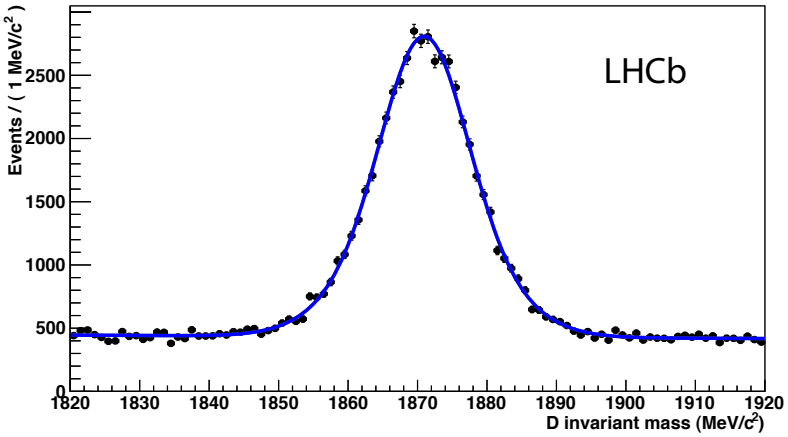

Figure 3.11: Invariant mass spectrum of $D^{\pm}$ candidates used to build the fake-B candidates.

fake-B candidates, with the results of the fit overlaid. In Table 3.3 the values of the triple Gaussian parameters returned by the fit are reported. The small bias of the mean value will be accounted as a systematic uncertainty. As it will be discussed later, since the analysis is performed in bins of p_{T} and η of the B meson, the decay time resolution model is meant to be determined for each bin separately.

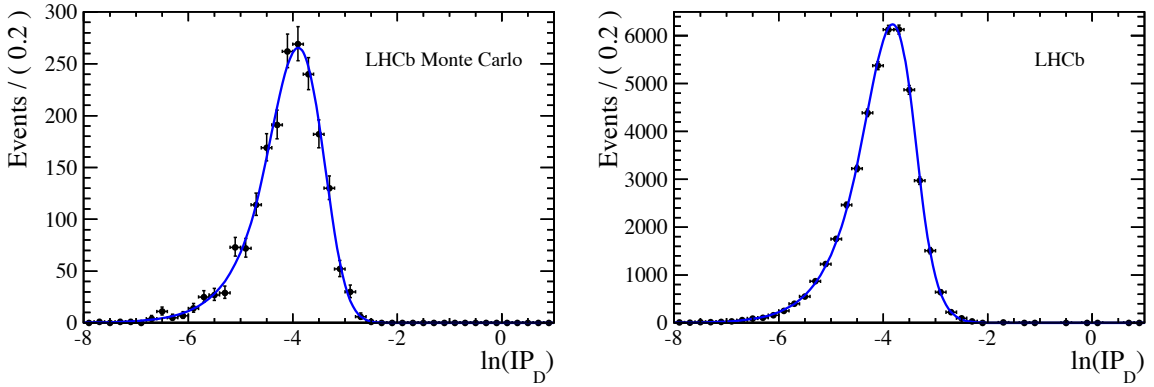

Figure 3.12: Distributions of $\ln(\mathrm{IP_D})$ for (left) prompt Monte Carlo $D^{\pm}$ mesons and (right) $D^{\pm}$ mesons from data used to build the fake-B candidates.

Parameter	prompt $D^{\pm}$ from MC	$D^{\pm}$ from fake-B
x_p	-3.90 ± 0.03	-3.82 ± 0.06
σ_p	0.55 ± 0.02	0.52 ± 0.03
ξ	-0.12 ± 0.04	-0.17 ± 0.01
ρ_1	-0.02 ± 0.04	-0.05 ± 0.01
ρ_2	-1.08 ± 0.40	-0.48 ± 0.05

Table 3.2: Results of the fits to the $\ln(\mathrm{IP_D})$ distributions using a `Bukin` function for prompt Monte Carlo $D^{\pm}$ mesons and $D^{\pm}$ mesons used to form the fake-B candidates.

.

3.2.3 Uncertainty on decay time resolution model

Two possible sources of uncertainty are considered. The first is clearly related to the method used. In this case, as a systematic uncertainty, the difference between the average resolution width of the fully simulated $B_s^0 \to D_s^- \pi^+$ decays and the width obtained using fake-B decays is taken. As already said, this amounts to 4 fs. The second source of uncertainty comes from the dependence of the decay time resolution on the proper time. To study such a dependence we divide the $B_s^0 \to D_s^- \pi^+$ Monte Carlo sample in bins of decay time and plotted the root mean square (RMS) of $t_{\mathrm{rec}} - t_{\mathrm{true}}$ as a function of the bin values in Fig. 3.14. The variation observed is of about ± 8 fs with respect to the average width of 43 fs. We assign a systematic uncertainty to the measurement by using an alternative resolution model where the three widths of the baseline resolution model are rescaled in order to have an average width differing by ± 8 fs from the baseline one, which takes into account the largest difference observed.

3.3 Fit model

A probability function (PDF) for the invariant mass and decay time of each channel starting from elementary components is defined. For each component, the mass and time parts are factorised, due to their independence.

Resolution model parameter	value
$\mu^{\rm res}$	-1.6 ± 0.2 fs
$\sigma_1^{\rm res}$	17.3 ± 0.6 fs
$\sigma_2^{\rm res}$	49.0 ± 0.9 fs
$\sigma_3^{\rm res}$	101 ± 6 fs
$f_1^{\rm res}$	0.25 ± 0.01
$f_2^{\rm res}$	0.68 ± 0.01
$\overline{\sigma}$ (average width)	49 ± 0.3 fs

Table 3.3: Values of the triple Gaussian function parameters obtained from a fit to the decay time distribution of fake-B candidates.

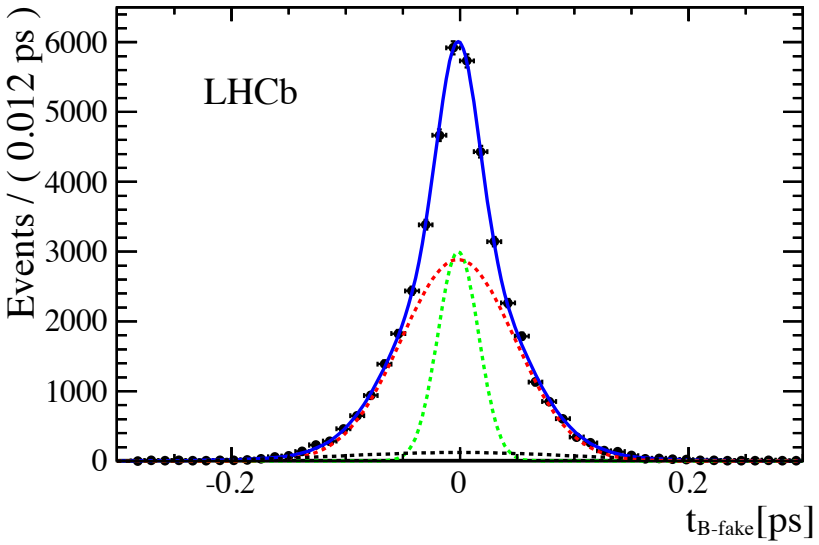

Figure 3.13: Decay time distribution of fake-B candidates, with the result of the fit overlaid.

3.3.1 Signal model

The signal component for each decay is modelled convolving a double Gaussian function with a function parameterizing the final state QED radiation (FSR). The PDF is given by

$$g(m) = A\,[\Theta(\mu - m)\ (\mu - m)^s] \otimes G(m), \tag{3.4}$$

where A is a normalization factor, Θ is the Heaviside function, G is the sum of two (or three) Gaussian functions with widths σ_1, σ_2 (σ_3) and zero mean, f_1 is the fraction of the first (f_2 that of the second) Gaussian function, μ is the B-meson mass, and the symbol $\otimes$ stands for convolution. The parameter s governs the amount of FSR which is studied using simulated events. Figure 3.15 shows the invariant mass spectra for Monte Carlo truth-matched selected signals with the result of fits overlaid. In the case of the $B^0 \to J/\psi\, K^{*0}$ decay I used a better description, obtained using a sum of three Gaussian functions, whereas for $B^0 \to D^-\pi^+$ and $B_s^0 \to D_s^-\pi^+$ decays two Gaussian functions are enough. Table 3.4 summarizes the values obtained from the fits.

The decay rate to a flavour-specific final state of a neutral B meson is parameterised with

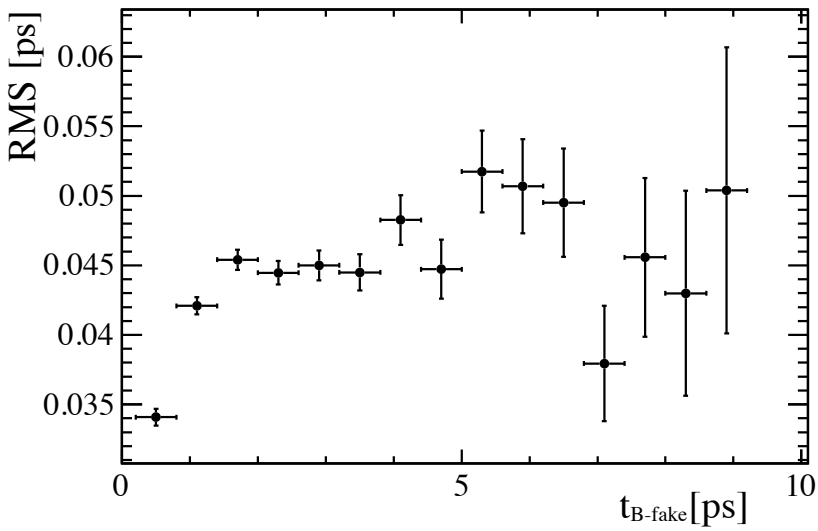

Figure 3.14: Root mean square (RMS) of $t_{\rm rec} - t_{\rm true}$ in bins of decay time for the fully simulated $B_s^0 \to D_s^- \pi^+$ events.

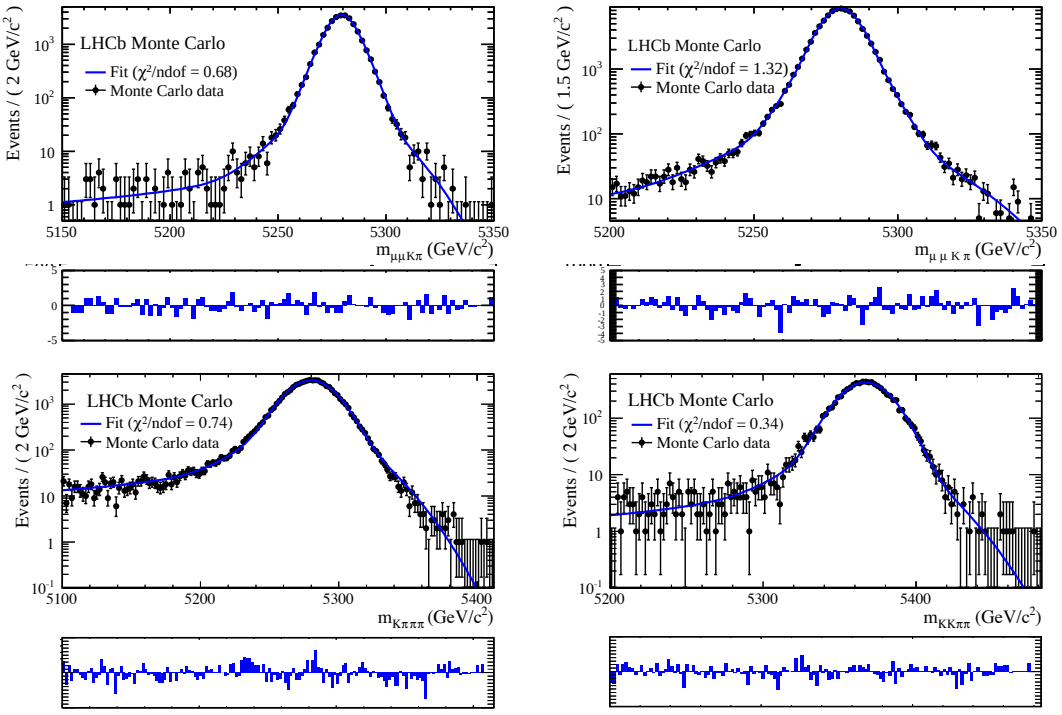

Figure 3.15: Invariant mass spectra for Monte Carlo selected events: (top left) $B^0 \to J/\psi K^{*0}$ 2011 data, (top right) $B^0 \to J/\psi K^{*0}$ 2012 data, (bottom left) $B^0 \to D^- \pi^+$ and (bottom right) $B_s^0 \to D_s^- \pi^+$.

Decay	$B^0 \to J/\psi K^{*0}$ 2011	$B^0 \to J/\psi K^{*0}$ 2012	$B^0 \to D^-\pi^+$	$B_s^0 \to D_s^-\pi^+$
μ [MeV/c^2]	5279.5 ± 0.04	5280.1 ± 0.03	5280.1 ± 0.07	5367.13 ± 0.02
σ_1 [MeV/c^2]	5.5 ± 0.3	5.8 ± 0.1	15.0 ± 0.12	15.3 ± 0.3
σ_2 [MeV/c^2]	9.1 ± 0.8	10.3 ± 0.4	30.6 ± 0.8	32.3 ± 2.9
σ_3 [MeV/c^2]	21.9 ± 2.3	25.9 ± 1.3	–	–
f_1	0.53 ± 0.12	0.65 ± 0.03	0.88 ± 0.13	0.92 ± 0.03
f_3	0.04 ± 0.01	0.04 ± 0.01	–	–
s	-0.9952 ± 0.0005	-0.9943 ± 0.0003	-0.9829 ± 0.0005	-0.9821 ± 0.0014

Table 3.4: Values of the signal mass shape parameters obtained from fits to Monte Carlo selected events.

the PDF defined at (1.55) at page 13:

$$\begin{aligned} f(t,\eta) &= K(1-\eta A_{CP})(1-\eta A_f) \\ &\quad \left\{ e^{-\Gamma t}\left[\Lambda_+ \cosh\left(\frac{\Delta\Gamma t}{2}\right) + \eta\Lambda_- \cos(\Delta m t)\right]\right\} \otimes R(t)\,\varepsilon_{acc}(t), \end{aligned} \tag{3.5}$$

where $R(t)$ is a decay time resolution function and $\varepsilon_{acc}(t)$ is the acceptance as a function of the decay time.

Decay time acceptance

Trigger and event selections lead to distortions in the shapes of the decay time distributions. The signal decay time acceptances are determined from fully simulated events. For each simulated decay, namely $B^0 \to J/\psi K^{*0}$, $B^0 \to D^-\pi^+$ and $B_s^0 \to D_s^-\pi^+$, we apply the trigger and selection algorithms as for the real data. Then an unbinned maximum likelihood fits to the distributions of the decay time is performed. In the fit all the physical parameters are fixed to their simulated values, *i.e.* average decay widths, decay width differences and mass differences of the B mass eigenstates. As decay time resolution model we use a single Gaussian function with 43 fs width. A good parameterization for $B^0 \to J/\psi K^{*0}$ is empirically found to be

$$\varepsilon_{\rm acc}(t) = \frac{1}{2}\left[1 - \mathrm{erf}\left(p_1 t^{p_2}\right)\right](1+p_3 t), \tag{3.6}$$

while for $B^0 \to D^-\pi^+$ and $B_s^0 \to D_s^-\pi^+$ decays it is

$$\varepsilon_{\rm acc}(t) = \frac{1}{2}\left[1 - \frac{1}{2}\mathrm{erf}\left(\frac{p_1 - t}{t}\right) - \frac{1}{2}\mathrm{erf}\left(\frac{p_2 - t}{t}\right)\right](1+p_3 t), \tag{3.7}$$

where p_1, p_2 and p_3 are free parameters and the erf is the error function. In Fig. 3.16 and 3.17 it is shown the decay time distribution and decay time acceptances of $B^0 \to J/\psi K^{*0}$, $B^0 \to D^-\pi^+$ and $B_s^0 \to D_s^-\pi^+$ decays with the results of the fits superimposed. The numerical values of the acceptance parameters obtained from the fits are reported in Table 3.5.

3.3.2 Background model

Two categories of background are considered: the combinatorial background, due to the random association of the tracks, and the partially reconstructed background, due to decays with a topology similar to that of the signal, but with one or more non reconstructed particles. The latter is present only for $B_{(s)}^0 \to D^-{}_{(s)}\pi^+$ decays.

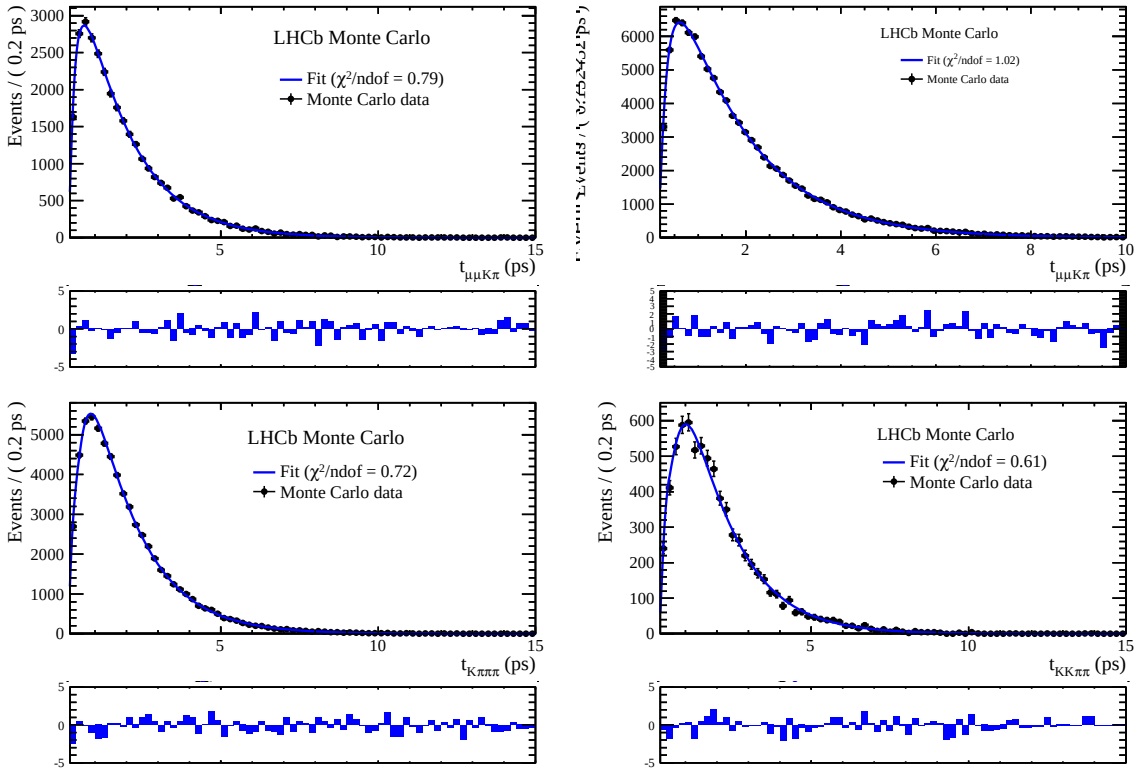

Figure 3.16: Decay time distributions of fully simulated events with the result of the fits overlaid for (top left) $B^0 \to J/\psi K^{*0}$ 2011, (top right) $B^0 \to J/\psi K^{*0}$ 2012, (bottom left) $B^0 \to D^-\pi^+$ and (bottom right) $B_s^0 \to D_s^-\pi^+$.

Parameter	$B^0 \to J/\psi K^{*0}$ 2011	$B^0 \to J/\psi K^{*0}$ 2012	$B^0 \to D^-\pi^+$	$B_s^0 \to D_s^-\pi^+$
p_1	0.13 ± 0.02	0.09 ± 0.01	0.33 ± 0.04	0.41 ± 0.01
p_2	-1.33 ± 0.07	-1.51 ± 0.05	0.93 ± 0.03	1.27 ± 0.08
p_3	-0.008 ± 0.005	-0.014 ± 0.003	-0.029 ± 0.003	-0.049 ± 0.007

Table 3.5: Acceptance parameters determined from decay time fits to Monte Carlo signal events. Note that the parameters p_1 and p_2 have different meanings for $B^0 \to J/\psi K^{*0}$ and $B^0_{(s)} \to D^-{}_{(s)}\pi^+$ decays. The decay time is measured in ps.

Combinatorial background

The invariant mass lineshape is well described in all cases by means of the following PDF

$$B(m) = Ke^{-m\xi^{\text{comb}}} \tag{3.8}$$

where K is a normalization factor. In order to study the parameterization of the decay time distributions we focus on the high invariant mass sidebands, defined as 5.31–5.34 GeV/c^2 for $B^0 \to J/\psi K^{*0}$, 5.40–5.80 GeV/c^2 for $B^0 \to D^-\pi^+$ and 5.45–5.90 GeV/c^2 for $B_s^0 \to D_s^-\pi^+$ decays. Concerning the $J/\psi K^{*0}$ and $D^-\pi^+$ spectra, empirically we find that an accurate description is

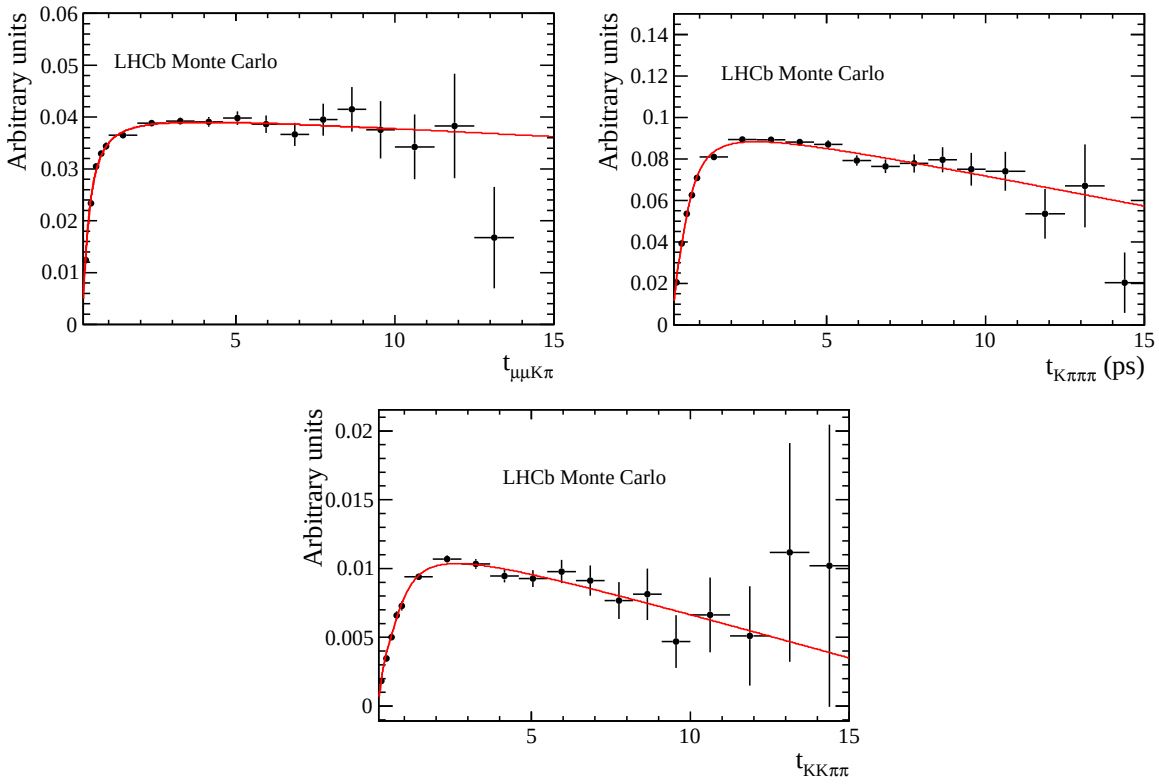

Figure 3.17: Decay time acceptances of fully simulated events with the result of the fits overlaid for (top left) $B^0 \to J/\psi K^{*0}$, (top right) $B^0 \to D^-\pi^+$ and (bottom) $B_s^0 \to D_s^-\pi^+$.

given by the PDF:

$$f\left(t,\,\eta\right) = K\left(1-\eta A_{\rm comb}\right)\left[f^{\rm comb}e^{-\Gamma_1^{\rm comb}t} + \left(1-f^{\rm comb}\right)e^{-\Gamma_2^{\rm comb}t}\right]\varepsilon_{\rm acc}^{\rm comb}\left(t\right), \tag{3.9}$$

where K is a normalization factor and $A_{\rm comb}$ is the charge asymmetry of the combinatorial background. For the $D_s^-\pi^+$ spectrum, a single exponential is enough, *i.e.*

$$f\left(t,\;\eta\right) = K\left(1-\eta A_{\rm comb}\right)e^{-\Gamma_1^{\rm comb}t}\varepsilon_{\rm acc}^{\rm comb}\left(t\right), \tag{3.10}$$

For the $J/\psi K^{*0}$ spectrum the effective "acceptance" function $\varepsilon_{\rm acc}^{\rm comb}\left(t\right)$ is given by

$$\varepsilon_{\rm acc}^{\rm comb}\left(t\right) = \frac{1}{2}\left[1-{\rm erf}\left(p_1^{\rm comb}t^{p_2^{\rm comb}}\right)\right], \tag{3.11}$$

whereas for the $D^-\pi^+$ and $D_s^-\pi^+$ spectra is

$$\varepsilon_{\rm acc}^{\rm comb}\left(t\right) = \frac{1}{2}\left[1-\frac{1}{2}{\rm erf}\left(\frac{p_1^{\rm comb}-t}{t}\right)-\frac{1}{2}{\rm erf}\left(\frac{p_2^{\rm comb}-t}{t}\right)\right]. \tag{3.12}$$

In Fig. 3.18 the decay time distributions corresponding to the high invariant mass sidebands with the result of the fits superimposed are shown. The values of the various parameters determined from the fits are reported in Table 3.6.

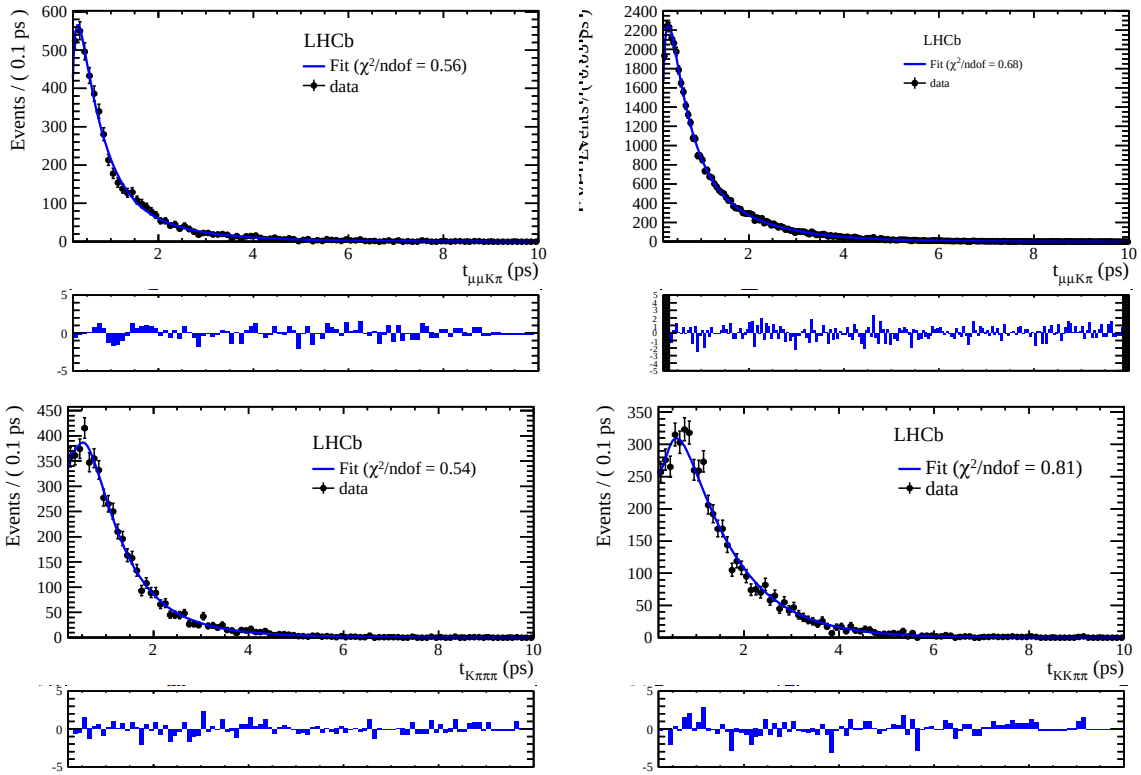

Figure 3.18: Decay time distributions of combinatorial background events from high invariant mass sidebands: (top left) $B^0 \to J/\psi K^{*0}$ 2011 data, (top right) $B^0 \to J/\psi K^{*0}$ 2012 data, (bottom left) $B^0 \to D^-\pi^+$ and (bottom right) $B_s^0 \to D_s^-\pi^+$. The result of the fits are superimposed.

Parameter	$B^0 \to J/\psi K^{*0}$ 2011	$B^0 \to J/\psi K^{*0}$ 2012	$B^0 \to D^-\pi^+$	$B_s^0 \to D_s^-\pi^+$
$p_1^{\rm comb}$	0.10 ± 0.02	0.01 ± 0.01	0.72 ± 0.07	0.69 ± 0.05
$p_2^{\rm comb}$	-2.39 ± 1.02	-2.26 ± 0.51	0.15 ± 0.03	0.29 ± 0.02
$\Gamma_1^{\rm comb}$	0.71 ± 0.05	-0.81 ± 0.01	0.70 ± 0.10	0.98 ± 0.29
$\Gamma_2^{\rm comb}$	2.12 ± 0.24	-2.59 ± 0.19	1.73 ± 0.11	–
$f^{\rm comb}$	0.15 ± 0.02	0.24 ± 0.02	0.05 ± 0.03	–

Table 3.6: Parameters determined from fits to events corresponding to the high mass sidebands. Note that the parameters p_1 and p_2 have different meanings for $B^0 \to J/\psi K^{*0}$ and $B^0_{(s)} \to D^-{}_{(s)}\pi$ decays. The decay time is measured in ps.

Partially reconstructed background

In the cases of the $D^-\pi^+$ and $D_s^-\pi^+$ spectra, a background component due to partially reconstructed B^0 and B_s^0 decays is also present in the low invariant mass sideband. The main contributions are expected to come from

- $B^0 \to D^{*-}(D^-\gamma, D^-\pi^0)\pi^+$ with $D^- \to K^-\pi^+\pi^-$, and a missing γ/π^0;
- $B^0 \to D^-(K^-\pi^+\pi^-)\rho^+(\pi^+\pi^0)$ where the π^0 is missing;
- $B_s^0 \to D_s^{*-}(D_s^-\gamma, D_s^-\pi^0)\pi^+$ with $D_s^- \to K^-K^+\pi^-$, and a missing γ/π^0;
- $B_s^0 \to D_s^-(K^-K^+\pi^-)\rho^+(\pi^+\pi^0)$ where the π^0 is missing.

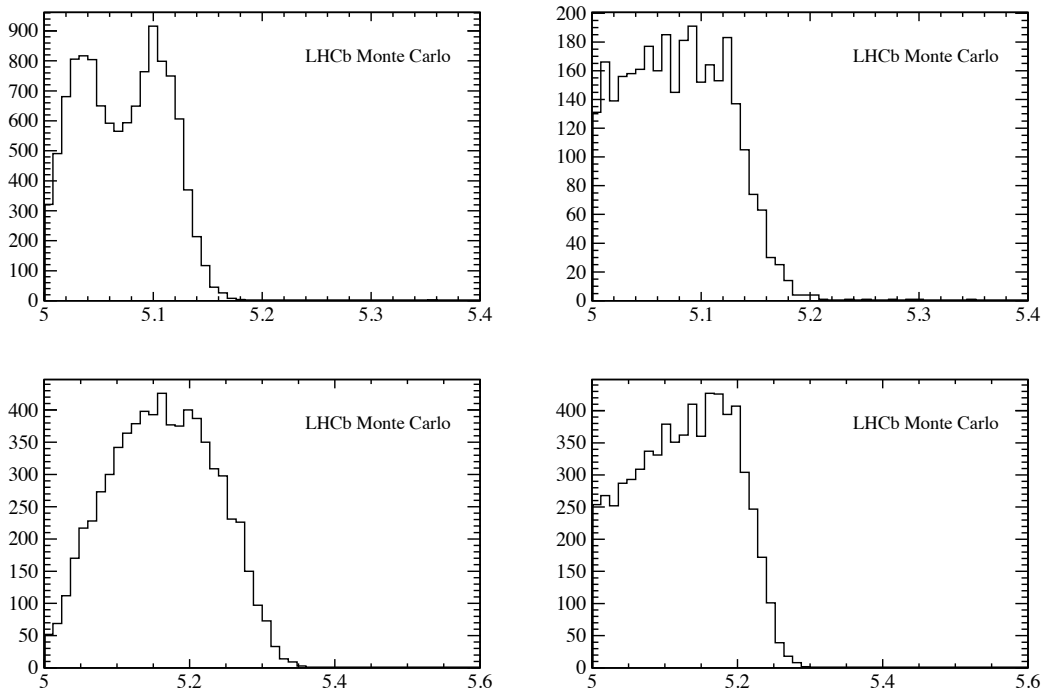

Figure 3.19: Invariant mass distributions of (top left) $B^0 \to D^{*-}\pi^+$, (top right) $B^0 \to D^-\rho^+$, (bottom left) $B_s^0 \to D_s^{*-}\pi^+$ and (bottom right) $B_s^0 \to D_s^-\rho^+$ simulated events.

We parameterise the partially reconstructed components by means of a kernel estimation technique [45] based on invariant mass distributions obtained from the full simulation, where the same selection applied to data is used. In order to take into account the discrepancy in resolution between data and Monte Carlo, the invariant mass were calculated by smearing with Gaussian-distributed random numbers the value of the true mass, *i.e.* the mass calculated using true momenta. The width of the Gaussian is extracted from data by fitting the invariant mass spectrum in the region where no contribution of the from partially reconstructed events is present. We find an average width of ~ 22 MeV/c^2 for both the decay modes. In addition, one can observe there is also a mass shifts of $6\,\mathrm{MeV}/c^2$ in the case of $B^0 \to D^-\pi^+$ decays and of $5\,\mathrm{MeV}/c^2$ in the case of $B_s^0 \to D_s^-\pi^+$ decays, which are included in the mass templates. The invariant mass templates so obtained are shown in Fig. 3.19.

As far as the decay time components are concerned, a good empirical parameterization is given by

$$f\left(t,\ \eta\right) = K\left(1 - \eta A_{\mathrm{phys}}\right) e^{-\Gamma^{\mathrm{phys}} t} \varepsilon_{\mathrm{acc}}^{\mathrm{phys}}\left(t\right), \tag{3.13}$$

where K is a normalization factor and

$$\varepsilon_{\mathrm{acc}}^{phys}\left(t\right) = \frac{1}{2}\left[1 - \mathrm{erf}\left(p_1^{\mathrm{phys}} t^{p_2^{\mathrm{phys}}}\right)\right]. \tag{3.14}$$

In Fig. 3.20 it is shown the decay time distribution corresponding to $B^0 \to D^{*-}\pi^+$, $B^0 \to D^-\rho^+$, $B_s^0 \to D_s^{*-}\pi^+$ and $B_s^0 \to D_s^-\rho^+$ decays, obtained using simulated events. Table 3.7 summarizes the values of the parameters obtained from the fits.

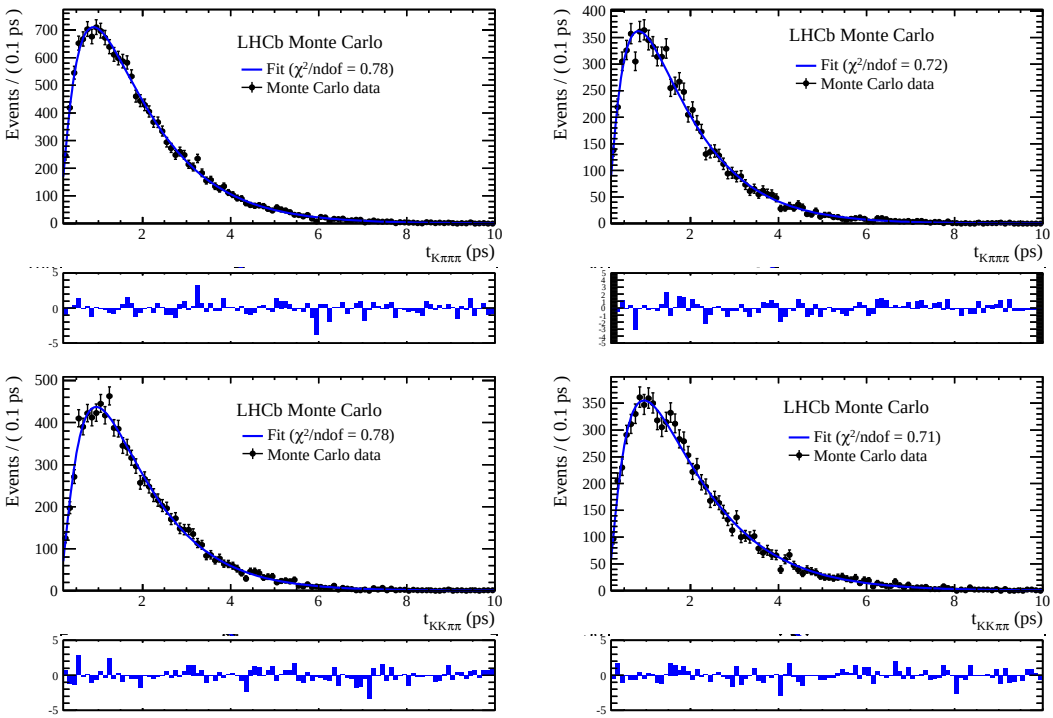

Figure 3.20: Decay time spectra of (top left) $B^0 \to D^{*-}\pi^+$, (top right) $B^0 \to D^-\rho^+$, (bottom left) $B_s^0 \to D_s^{*-}\pi^+$ and (bottom right) $B_s^0 \to D_s^-\rho^+$ decays, obtained using simulated events. The results of the fits are overlaid.

Parameter	$B^0 \to D^-\pi^+$ BDT		$B^0 \to D^-\pi^+$ BDT	
	$B^0 \to D^{*-}\pi^+$	$B^0 \to D^-\rho^+$	$B_s^0 \to D_s^{*-}\pi^+$	$B_s^0 \to D_s^-\rho^+$
p_1^{phys}	0.69 ± 0.08	0.62 ± 0.10	0.81 ± 0.09	0.66 ± 0.08
p_2^{phys}	-0.46 ± 0.06	-0.50 ± 0.08	-0.44 ± 0.06	-0.51 ± 0.07
$\Gamma^{\rm phys}$ [ps^{-1}]	0.83 ± 0.02	0.89 ± 0.03	0.78 ± 0.02	0.92 ± 0.02

Table 3.7: Parameters of functions describing the decay time distributions of partially reconstructed background decays, as determined from fits to simulated events.

$B^0 \to D^-\pi^+$ background of the $B_s^0 \to D_s^-\pi^+$ decay

In the case of $B_s^0 \to D_s^-\pi^+$ decays, there is also a background component due to the $B^0 \to D^-\pi^+$ decays. We accounted for this component in the fits using the same parametrization adopted for the signal as described in Sec. 3.3.1. The invariant mass resolution model is the same as for the B_s^0 decay, with an average mass shifted by the difference in nominal masses between B^0 and B_s^0 mesons according to the PDG. In the decay time PDF, the production asymmetry is fixed from the $B^0 \to D^-\pi^+$ fit. The $B^0 \to D^-\pi^+$ yield is fixed from the ratio between hadronization fractions and branching ratios as reported in Sec. 3.4.3 and in Table 3.14.

Parameter	Value	Reference
$\Delta m_d\,[\text{ps}^{-1}]$	0.510 ± 0.004	[6]
$\Delta m_s\,[\text{ps}^{-1}]$	17.768 ± 0.024	[46]
$\Gamma_d\,[\text{ps}]$	0.6583 ± 0.0030	[6]
$\Gamma_s\,[\text{ps}]$	0.6596 ± 0.0046	[6]
$\Delta\Gamma_d$	0	
$\Delta\Gamma_s\,[\text{ps}^{-1}]$	0.081 ± 0.011	[6]
$\lvert q/p\rvert_{B^0}$	0.9997 ± 0.0013	[47]
$\lvert q/p\rvert_{B_s^0}$	1.0003 ± 0.0030	[48]

Table 3.8: Values of the various physical inputs used in the fits.

3.4 Fit results

In this section we present the results of the invariant mass and decay time fits used to determine the production asymmetries. We perform global fits to the whole data samples first, and then we split the events in bins of p_{T} and η, performing fits for each bin.

3.4.1 Global fits

We perform simultaneous unbinned maximum likelihood fits to the invariant mass and the decay time distributions for each decay mode. The oscillation frequencies Δm_d and Δm_s, the mixing parameters $|q/p|_{B^0}$ and $|q/p|_{B_s^0}$, the average decay widths Γ_d and Γ_s, and the width differences $\Delta\Gamma_d$ and $\Delta\Gamma_s$ are fixed to the values reported in Table 3.8.

In the limit of small *CP* and detection asymmetries, Eq. 3.5 can be written to first order as

$$\begin{aligned} f(t,\eta) \;\simeq\; & K\left[1-\eta\left(A_{CP}+A_f\right)\right] \\ & \left\{e^{-\Gamma t}\left[\Lambda_+\cosh\left(\frac{\Delta\Gamma t}{2}\right)+\eta\Lambda_-\cos\left(\Delta m t\right)\right]\right\}\otimes R(t)\,\varepsilon_{acc}(t)\,, \end{aligned} \tag{3.15}$$

i.e. the fit is only sensitive to the sum of A_{CP} and A_f. In the fit we conventionally fix the direct *CP* violation term A_{CP} to zero, and we leave the detection asymmetry A_f as a free parameter. According to Eq. 3.15, one does not expect any impact on the determination of the production asymmetry A_{P} from the choice of the value of A_{CP}. As a cross-check, we repeat the fit by allowing *CP* violation up to $\pm 1\%$, and as expected the impact on the determination of A_{P} turns out to be completely negligible.

In Figs. 3.21, 3.22, 3.23 and 3.24 we show the $\mu\mu K\pi$, $K\pi\pi\pi$ and $KK\pi\pi$ invariant mass and decay time distributions, respectively, with the result of the fits overlaid. Figures 3.25, 3.26, 3.27 and 3.28 show the raw asymmetries for events in the high and low mass sidebands, as well as for events in the signal mass region.

The values of the parameters determined from the fits are reported in Table 3.9. In particular, the values of the production asymmetries from the global fits are found to be

$$A_{\text{P}}\left(B^0\right)^{2011}_{J/\psi K^{*0}} = (-1.16 \pm 0.63)\,\%, \tag{3.16}$$

$$A_{\text{P}}\left(B^0\right)^{2012}_{J/\psi K^{*0}} = (-1.24 \pm 0.39)\,\%, \tag{3.17}$$

$$A_{\text{P}}\left(B^0\right)_{D^-\pi^+} = (-0.58 \pm 0.70)\,\%, \tag{3.18}$$

$$A_{\text{P}}\left(B_s^0\right) = (-0.32 \pm 1.66)\,\%. \tag{3.19}$$

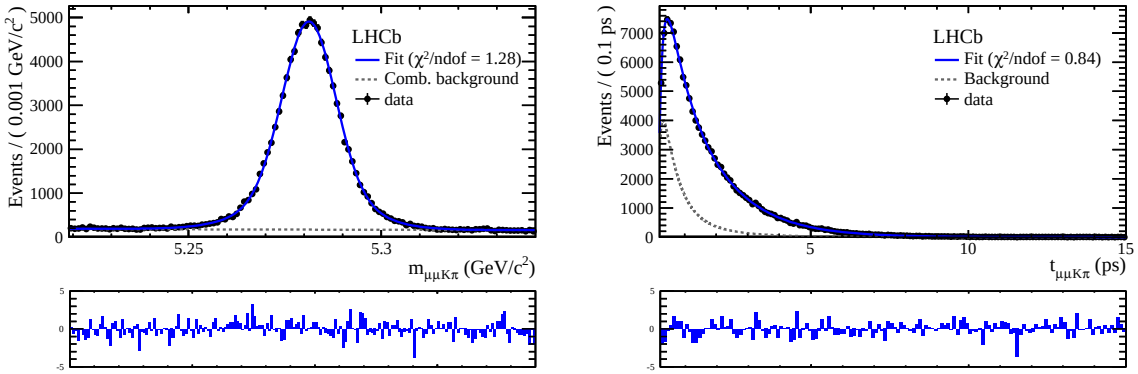

Figure 3.21: Distributions of (left) invariant mass and (right) decay time for $B^0 \to J/\psi K^{*0}$ decays with 2011 data, with the results of the fit overlaid. The dashed line corresponds to the combinatorial background.

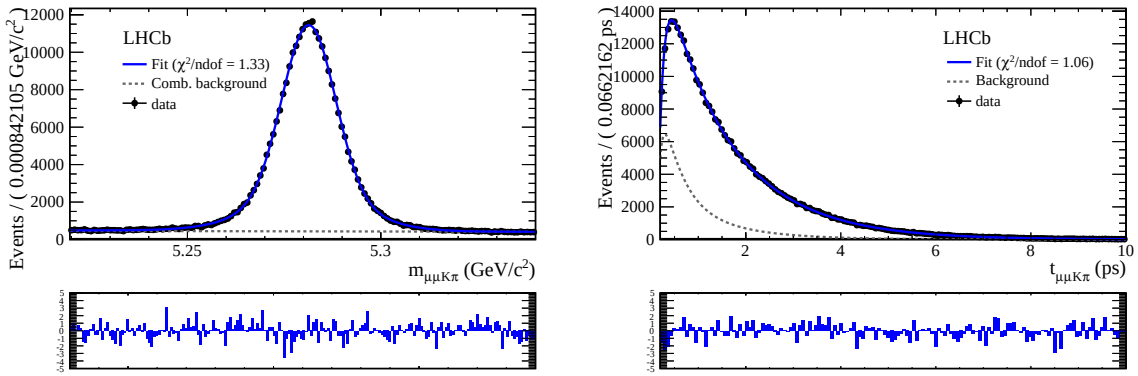

Figure 3.22: Distributions of (left) invariant mass and (right) decay time for $B^0 \to J/\psi K^{*0}$ decays with 2012 data, with the results of the fit overlaid. The dashed line corresponds to the combinatorial background.

3.4.2 Toy Monte Carlo studies

Toy Monte Carlo studies are performed to validate the fit model. Figure 3.29 shows the distributions of the pulls for the quantities $A_{\rm P}$, A_f and $A_{\rm comb}$ obtained by means of 2000 global fits to toy Monte Carlo events using the results of the $B^0 \to J/\psi K^{*0}$, $B^0 \to D^-\pi^+$ and $B_s^0 \to D_s^-\pi^+$ global fits as inputs to the toys. The correlations between the three parameters are reported in Table 3.10.

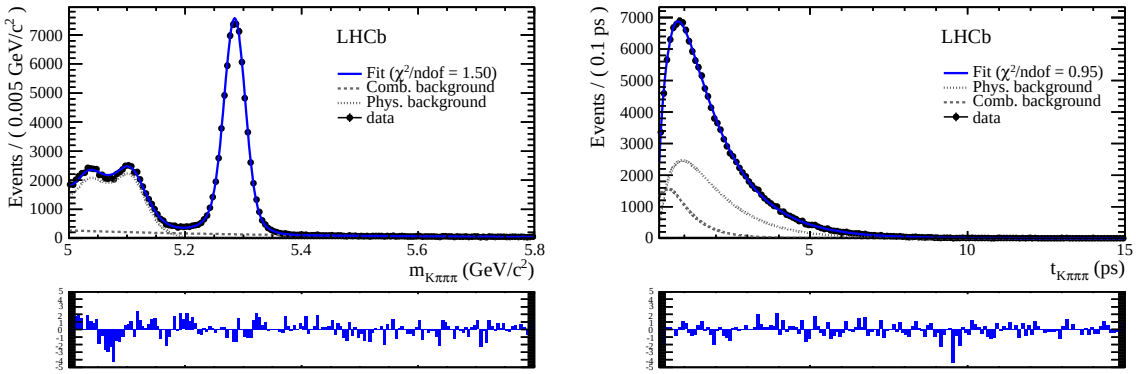

Figure 3.23: Distributions of (left) invariant mass and (right) decay time for $B^0 \to D^-\pi^+$ decays, with the results of the fit overlaid. The dashed line corresponds to the combinatorial background, while the dotted line corresponds to the partially reconstructed background.

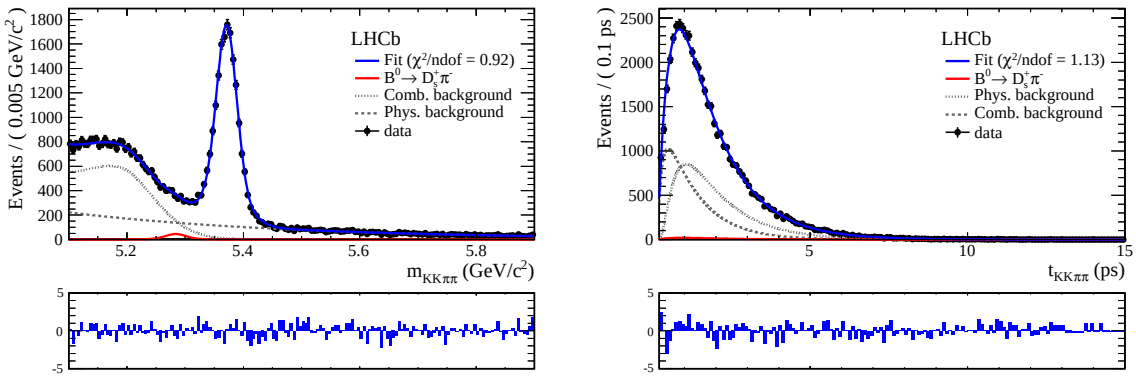

Figure 3.24: Distributions of (left) invariant mass and (right) decay time for $B_s^0 \to D_s^-\pi^+$ decays, with the results of the fit overlaid. The dashed line corresponds to the combinatorial background, while the dotted line corresponds to the partially reconstructed background.

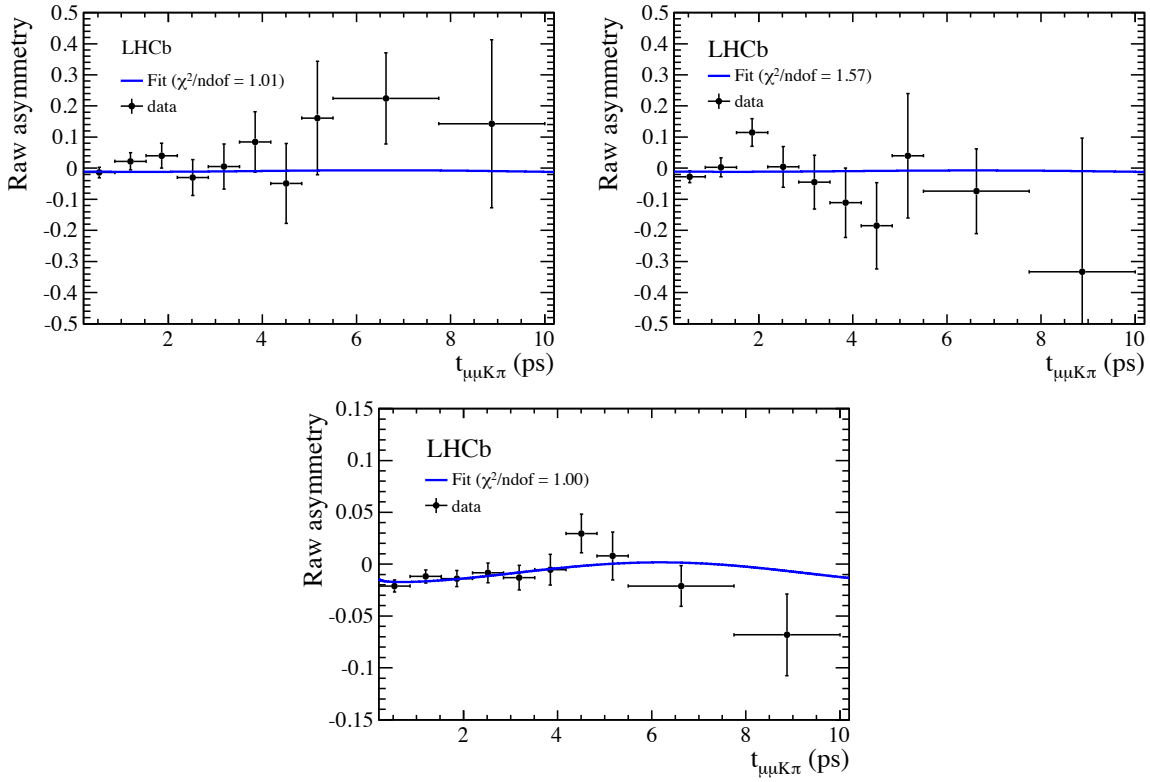

Figure 3.25: Raw asymmetries as a function of the decay time in the (top left) low mass sideband, (top right) high mass sideband, and (bottom) signal mass region from the $B^0 \to J/\psi K^{*0}$ global fit performed with 2011 data. The low mass sideband is defined as $5.22 < m < 5.25\,\mathrm{GeV}/c^2$, the high mass sideband as $5.31 < m < 5.34\,\mathrm{GeV}/c^2$, and the signal region as $5.25 < m < 5.31\,\mathrm{GeV}/c^2$.

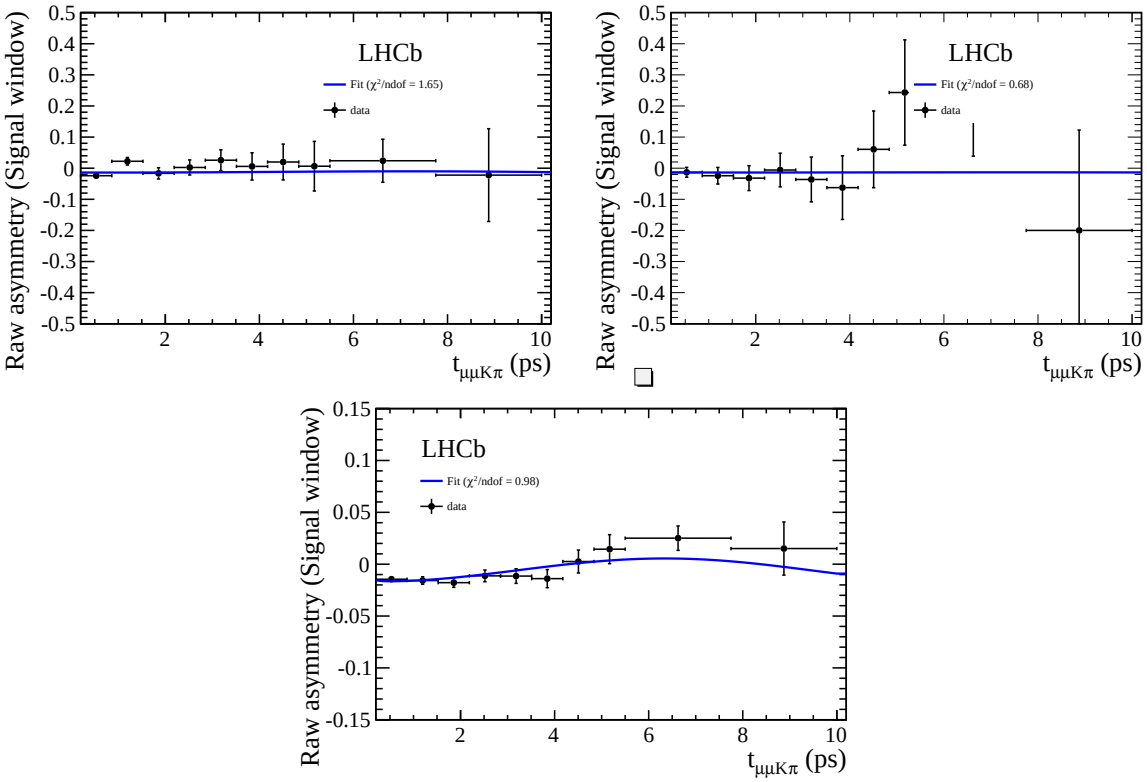

Figure 3.26: Raw asymmetries as a function of the decay time in the (top left) low mass sideband, (top right) high mass sideband, and (bottom) signal mass region from the $B^0 \to J/\psi K^{*0}$ global fit performed with 2012 data. The low mass sideband is defined as $5.22 < m < 5.25\,\mathrm{GeV}/c^2$, the high mass sideband as $5.31 < m < 5.34\,\mathrm{GeV}/c^2$, and the signal region as $5.25 < m < 5.31\,\mathrm{GeV}/c^2$.

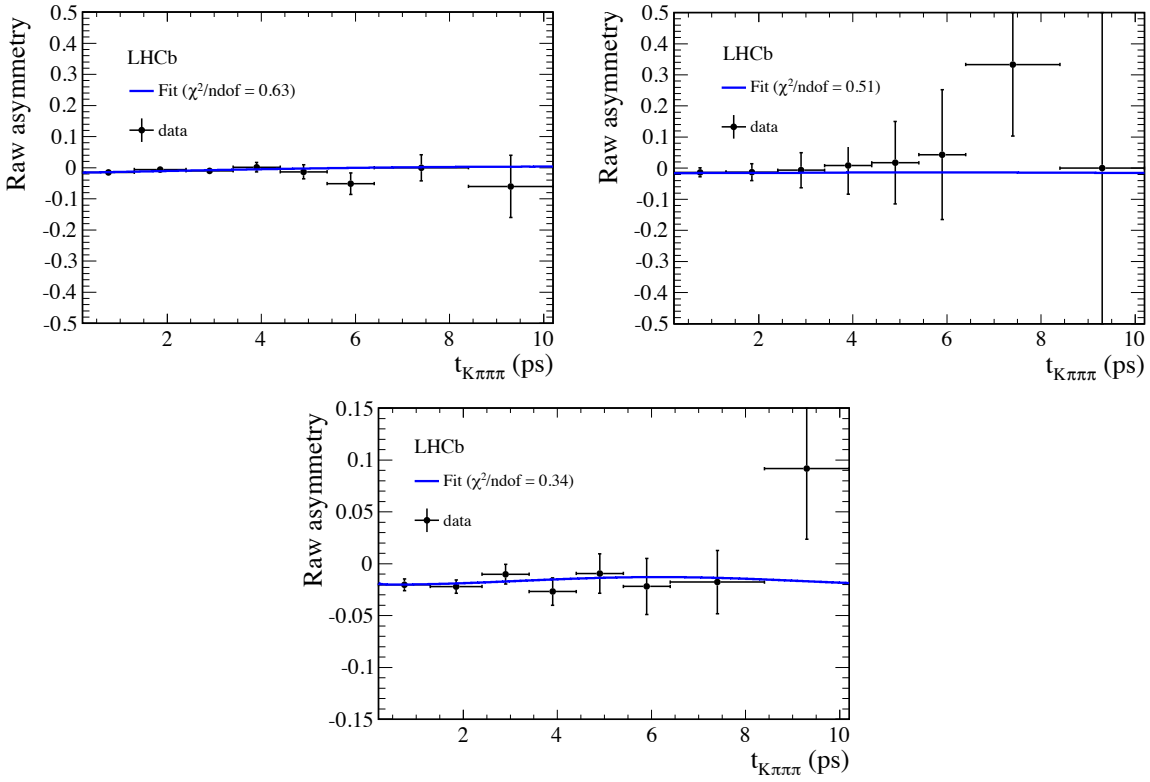

Figure 3.27: Raw asymmetries as a function of the decay time in the (top left) low mass sideband, (top right) high mass sideband, and (bottom) signal mass region from the $B^0 \to D^-\pi^+$ global fit. The low mass sideband is defined as $5.00 < m < 5.20\,\mathrm{GeV}/c^2$, the high mass sideband as $5.36 < m < 5.80\,\mathrm{GeV}/c^2$, and the signal region as $5.20 < m < 5.36\,\mathrm{GeV}/c^2$.

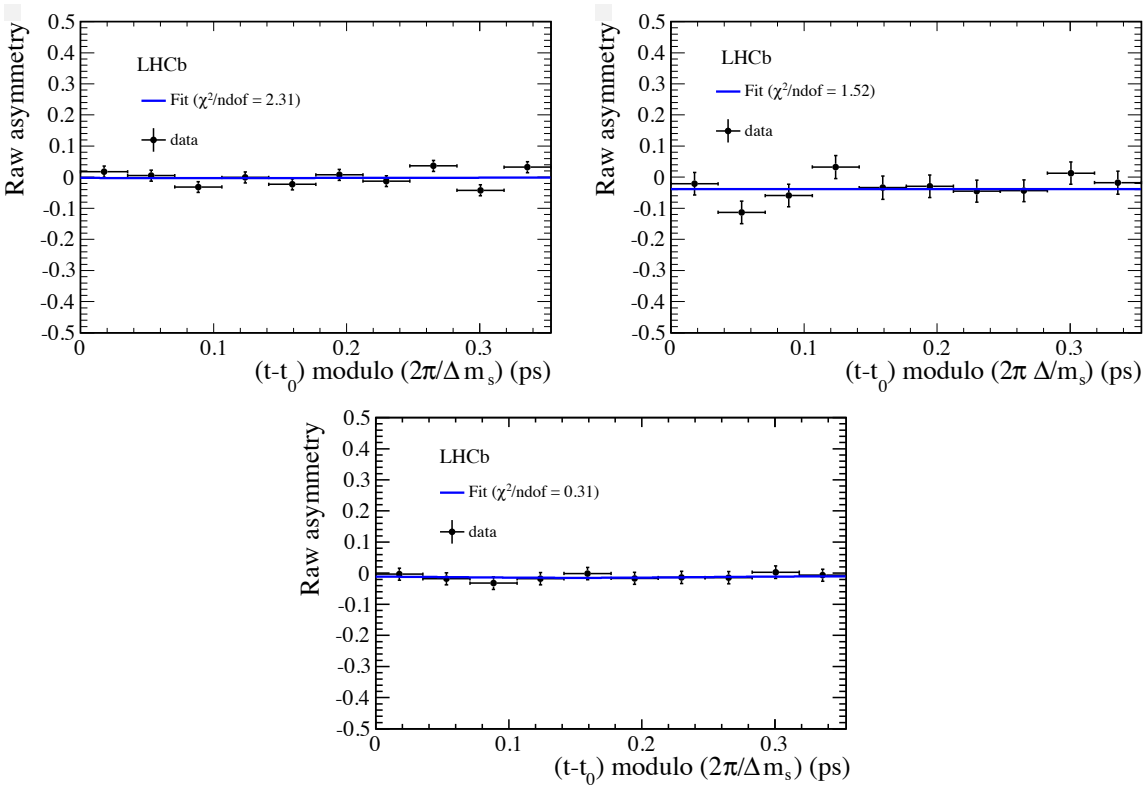

Figure 3.28: Raw asymmetries as a function of the decay time in the (top left) low mass sideband, (top right) high mass sideband, and (bottom) signal mass region from the $B_s^0 \to D_s^- \pi^+$ global fit. The low mass sideband is defined as $5.10 < m < 5.30\,\mathrm{GeV}/c^2$, the high mass sideband as $5.45 < m < 5.90\,\mathrm{GeV}/c^2$, and the signal region as $5.30 < m < 5.45\,\mathrm{GeV}/c^2$.

Parameter	$B^0 \to J/\psi K^{*0}$ 2011	$B^0 \to J/\psi K^{*0}$ 2012	$B^0 \to D^-\pi^+$	$B_s^0 \to D_s^-\pi^+$
		Asymmetries [%]		
$A_{\rm P}$	-1.16 ± 0.63	-1.24 ± 0.39	-0.58 ± 0.70	-0.32 ± 1.66
A_f	-0.86 ± 0.46	-0.55 ± 0.28	-1.51 ± 0.49	-1.10 ± 0.86
$A_{\rm comb}$	-1.57 ± 0.90	-1.39 ± 0.42	-2.05 ± 1.11	-0.39 ± 1.24
$A^{\rm phys}_{B^0_{(s)} \to D^-_{(s)}\rho^+}$	–	–	3.32 ± 2.42	-12.72 ± 20.21
$A^{\rm phys}_{B^0_{(s)} \to D^{*-}_{(s)}\pi^+}$	–	–	-6.82 ± 3.09	3.84 ± 4.58
		Yields		
$N^{\rm sig}$	$93\,627 \pm 360$	$265\,424 \pm 691$	$76\,682 \pm 308$	$16\,887 \pm 174$
$N^{\rm comb}$	$20\,722 \pm 239$	$84\,389 \pm 545$	$19\,416 \pm 445$	$15\,127 \pm 439$
$N^{\rm phys}_{B^0_{(s)} \to D^-_{(s)}\rho^+}$	–	–	$33\,010 \pm 1249$	$3\,024 \pm 457$
$N^{\rm phys}_{B^0_{(s)} \to D^{*-}_{(s)}\pi^+}$	–	–	$25\,447 \pm 1096$	$15\,678 \pm 584$
		Signal parameters		
μ [GeV/c^2]	5.2813 ± 0.0001	5.2814 ± 0.0001	5.2850 ± 0.0001	5.3716 ± 0.0002
σ_1 [GeV/c^2]	0.0067 ± 0.0001	0.0068 ± 0.0001	0.0174 ± 0.0002	0.0171 ± 0.0003
σ_2 [GeV/c^2]	0.0129 ± 0.0004	0.0141 ± 0.0003	0.0343 ± 0.0020	0.0366 ± 0.0018
f_1	0.71 ± 0.02	0.73 ± 0.01	0.83 ± 0.01	0.75 ± 0.02
p_1	0.11 ± 0.01	0.0886	0.35 ± 0.01	0.43 ± 0.01
p_2	-1.43 ± 0.05	-1.5350	1.02 ± 0.03	1.09 ± 0.06
p_3	-0.006 ± 0.003	-0.0115	-0.033 ± 0.002	-0.023 ± 0.006
		Background parameters		
$\xi^{\rm comb}$ [c^2/ GeV]	1.16 ± 0.12	-0.86 ± 0.10	2.33 ± 0.08	2.63 ± 0.10
$p_1^{\rm comb}$	0.02 ± 0.01	0.01 ± 0.01	0.23 ± 0.02	0.43 ± 0.02
$p_2^{\rm comb}$	-1.75 ± 0.21	-2.30 ± 0.29	0.79 ± 0.05	–
$p_1^{\rm phys}$	–	–	0.80 ± 0.08	0.47 ± 0.07
$p_2^{\rm phys}$	–	–	-0.43 ± 0.05	-1.05 ± 0.07
$f^{\rm comb}$	0.13 ± 0.02	0.21 ± 0.01	0.98 ± 0.01	–
$\Gamma_1^{\rm comb}$ [ps^{-1}]	0.73 ± 0.04	-0.83 ± 0.01	1.61 ± 0.06	0.97 ± 0.02
$\Gamma_2^{\rm comb}$ [ps^{-1}]	2.15 ± 0.16	-2.56 ± 0.12	0.51 ± 0.05	–
$\Gamma^{\rm phys}_{B^0_{(s)} \to D^-_{(s)}\rho^+}$ [ps^{-1}]	–	–	0.82 ± 0.01	0.81 ± 0.10
$\Gamma^{\rm phys}_{B^0_{(s)} \to D^{*-}_{(s)}\pi^+}$ [ps^{-1}]	–	–	0.99 ± 0.06	0.87 ± 0.02

Table 3.9: Values of the parameters obtained from the global fits.

Correlation	$B^0 \to J/\psi K^{*0}$	$B^0 \to D^-\pi^+$	$B_s^0 \to D_s^-\pi^+$
$\rho\,(A_{\rm P}, A_f)$	-0.64	-0.66	-0.01
$\rho\,(A_{\rm P}, A_{\rm comb})$	-0.09	-0.08	0.03

Table 3.10: Values of correlations between $A_{\rm P}$, A_f and $A_{\rm comb}$ for $B^0 \to J/\psi K^{*0}$, $B^0 \to D^-\pi^+$ and $B_s^0 \to D_s^-\pi^+$ decays determined from global fits to toy Monte Carlo events.

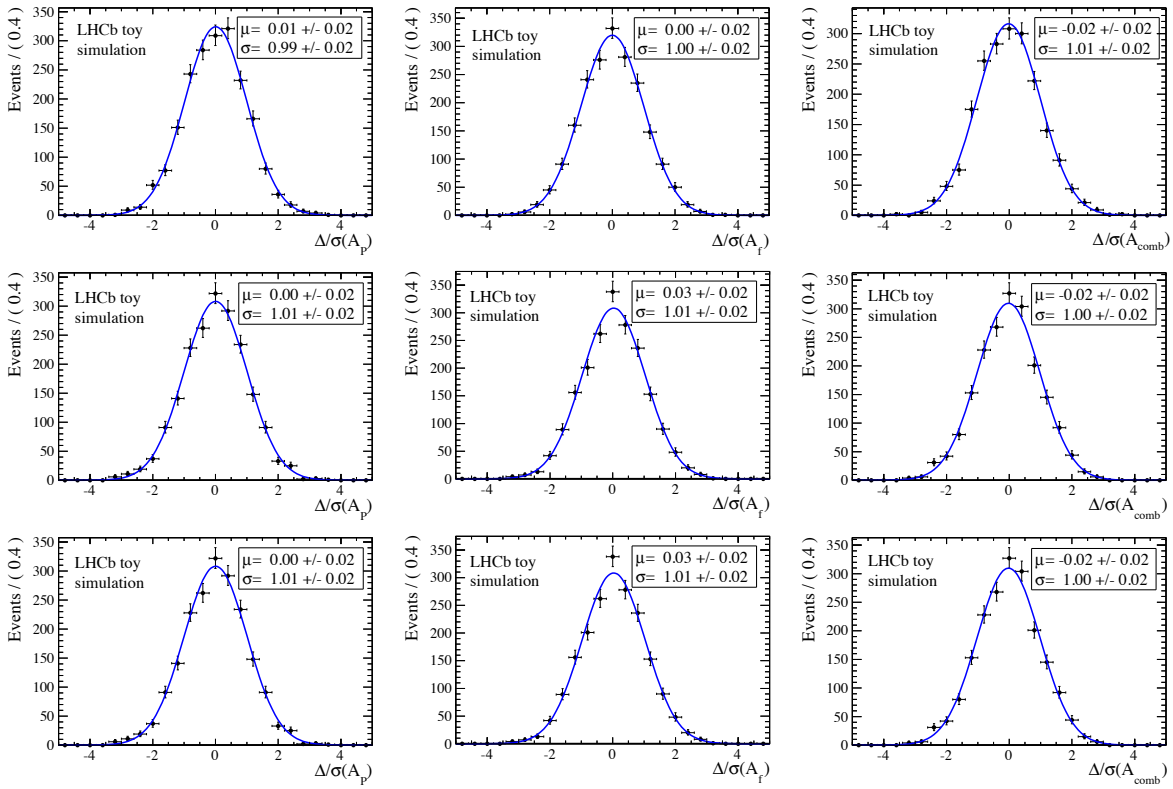

Figure 3.29: Distributions of the pulls for $A_{\rm P}$ (left), A_f (center) and $A_{\rm comb}$ (right) obtained from global fits to toy Monte Carlo events for the $B^0 \to J/\psi K^{*0}$ (top), $B^0 \to D^- \pi^+$ (middle) and $B_s^0 \to D_s^- \pi^+$ (bottom) decays.

3.4.3 Estimation of misidentified background yields

The expected number of misidentified background events in the case of selected $B^0 \to D^-\pi^+$ decays is given by

$$\begin{aligned}
N(\Lambda_b^0 \to \Lambda_c^-\pi^+) &= N(B^0 \to D^-\pi^+) \cdot \frac{f_{\Lambda_b}}{f_d} \cdot \frac{\mathcal{B}(\Lambda_b^0 \to \Lambda_c^-\pi^+)}{\mathcal{B}(B^0 \to D^-\pi^+)} \cdot \frac{\epsilon_{\rm rec}(\Lambda_b \to \Lambda_c^-\pi^+)}{\epsilon_{\rm rec}(B^0 \to D^-\pi^+)} \cdot \\
&\quad \cdot \frac{\epsilon_{\rm mis-ID}(\Lambda_b^0 \to \Lambda_c^-\pi^+)}{\epsilon_{\rm PID}(B^0 \to D^-\pi^+)}, \\
N(B_s^0 \to D_s^-\pi^+) &= N(B^0 \to D^-\pi^+) \cdot \frac{f_s}{f_d} \cdot \frac{\mathcal{B}(B_s^0 \to D_s^-\pi^+)}{\mathcal{B}(B^0 \to D^-\pi^+)} \cdot \frac{\epsilon_{\rm rec}(B_s^0 \to D_s^-\pi^+)}{\epsilon_{\rm rec}(B^0 \to D^-\pi^+)} \cdot \\
&\quad \cdot \frac{\epsilon_{\rm mis-ID}(B_s^0 \to D_s^-\pi^+)}{\epsilon_{\rm PID}(B^0 \to D^-\pi^+)}, \\
N(B^0 \to D^-K^+) &= N(B^0 \to D^-\pi^+) \cdot \frac{\mathcal{B}(B^0 \to D^-K^+)}{\mathcal{B}(B^0 \to D^-\pi^+)} \cdot \frac{\epsilon_{\rm rec}(B^0 \to D^-K^+)}{\epsilon_{\rm rec}(B^0 \to D^-\pi^+)} \cdot \\
&\quad \cdot \frac{\epsilon_{\rm mis-ID}(B^0 \to D^-K^+)}{\epsilon_{\rm PID}(B^0 \to D^-\pi^+)},
\end{aligned}$$

where f is probability for a b quark to hadronize into a given b-hadron, $N(B^0 \to D_s^-\pi^+)$ is the observed signal yield, $\mathcal{B}$ is the branching fraction, $\epsilon_{\rm rec}$ is the overall reconstruction efficiency (including generator level, trigger, preselection and final selection efficiencies), $\epsilon_{\rm PID}$ is the PID efficiency, taking into account that the PID requirements are applied in relevant invariant mass regions, and $\epsilon_{\rm mis-ID}$ is the PID efficiency for the misidentified background hypothesis.

Similarly, for the case of selected $B^0 \to D^-\pi^+$ decays, we have

$$\begin{aligned}
N(\Lambda_b^0 \to \Lambda_c^-\pi^+) &= N(B_s^0 \to D_s^-\pi^+) \cdot \frac{f_{\Lambda_b}}{f_s} \cdot \frac{\mathcal{B}(\Lambda_b^0 \to \Lambda_c^-\pi^+)}{\mathcal{B}(B_s^0 \to D_s^-\pi^+)} \cdot \frac{\epsilon_{\rm rec}(\Lambda_b^0 \to \Lambda_c^-\pi^+)}{\epsilon_{\rm rec}(B_s^0 \to D_s^-\pi^+)} \cdot \\
&\quad \cdot \frac{\epsilon_{\rm mis-ID}(\Lambda_b^0 \to \Lambda_c^-\pi^+)}{\epsilon_{\rm PID}(B_s^0 \to D_s^-\pi^+)} \\
N(B^0 \to D^-\pi^+) &= N(B_s^0 \to D_s^-\pi^+) \cdot \frac{f_d}{f_s} \cdot \frac{\mathcal{B}(B^0 \to D^-\pi^+)}{\mathcal{B}(B_s^0 \to D_s^-\pi^+)} \cdot \frac{\epsilon_{\rm rec}(B^0 \to D^-\pi^+)}{\epsilon_{\rm rec}(B_s^0 \to D_s^-\pi^+)} \cdot \\
&\quad \cdot \frac{\epsilon_{\rm mis-ID}(B^0 \to D^-\pi^+)}{\epsilon_{\rm PID}(B_s^0 \to D_s^-\pi^+)} \\
N(B_s^0 \to D_s^-K^+) &= N(B_s^0 \to D_s^-\pi^+) \cdot \frac{\mathcal{B}(B^0 \to D_s^-K^+)}{\mathcal{B}(B_s^0 \to D_s^-\pi^+)} \cdot \frac{\epsilon_{\rm rec}(B^0 \to D_s^-K^+)}{\epsilon_{\rm rec}(B_s^0 \to D_s^-\pi^+)} \cdot \\
&\quad \cdot \frac{\epsilon_{\rm mis-ID}(B^0 \to D^-K^+)}{\epsilon_{\rm PID}(B_s^0 \to D_s^-\pi^+)}
\end{aligned}$$

The reconstruction efficiencies are evaluated from simulation, whereas PID performances are determined from data, using a dedicated calibration sample of $D^{*-} \to D^0(K^-\pi^+)$ events and making use of the package `PIDCalibTool` [49]. PID performances, in general, depend on kinematics. For this reason we reweight the momentum and pseudorapidity of the D^0 daughters (bachelor pion) to match those of Monte Carlo $D_{(s)}^-$ daughters (bachelor pion). The relevant branching fractions and the hadronization fractions are reported in Tables 3.11 and 3.12. The final background yields are summarized in Tables 3.13 and 3.14. With the exception of the

$B^0 \to D_s^- \pi^+$ background to the $B_s^0 \to D_s^- \pi^+$ signal, which is modelled in the fit, we conclude that the presence of cross-feed background events can be safely neglected, when compared with signal yields.

Decay	$\mathcal{B} \times 10^4$
$B^0 \to D^-(K^+\pi^-\pi^-)\pi^+$	2.45 ± 0.12
$B^0 \to D^-(K^+\pi^-\pi^-)K^+$	0.18 ± 0.02
$B^0 \to D_s^-(K^+K^-\pi^-)\pi^+$	0.0119 ± 0.0015
$B_s^0 \to D_s^-(K^+K^-\pi^-)\pi^+$	1.67 ± 0.15
$B_s^0 \to D_s^-(K^+K^-\pi^-)K^+$	0.11 ± 0.02
$\Lambda_b^0 \to \Lambda_c^-(\bar{p}K^+\pi^-)\pi^+$	2.85 ± 2.13

Table 3.11: Relevant branching fractions used for the estimation of misidentified background yields. Values are take from the PDG.

b hadron species	hadronization fraction
B^0 or B^+	0.326 ± 0.024
B_s^0	0.084 ± 0.009
Λ_b^0	0.264 ± 0.074

Table 3.12: Hadronization fractions calculated from LHCb measurements [50, 51] assuming $f_{B^0} = f_{B^+}$ and $f_{B^+} + f_{B^0} + f_{B_s^0} + f_{\Lambda_b^0} = 1$.

Decay	ϵ_{rec} [%]	ϵ_{PID} [%]	$\epsilon_{\text{mis-ID}}$ [%]	N
$B^0 \to D^-\pi^+$	0.324 ± 0.001	69.0 ± 0.08	–	$76\,682 \pm 308$
$B^0 \to D^-K^+$	0.315 ± 0.001	–	2.03 ± 0.01	14 ± 2
$B_s^0 \to D_s^-\pi^+$	0.074 ± 0.001	–	1.34 ± 0.08	60 ± 18
$\Lambda_b^0 \to \Lambda_c^-\pi^+$	0.022 ± 0.003	–	1.39 ± 0.15	99 ± 81

Table 3.13: Reconstruction efficiencies, PID efficiencies, mis-ID efficiencies and expected number of background events for $B^0 \to D^-\pi^+$ decays. In the $B^0 \to D^-\pi^+$ row, the last column reports the number of events obtained from the global fit.

3.4.4 Fits in bins of p_{T} and η

To investigate whether the production asymmetry has a dependence on the kinematics of the B mesons, we perform again the same fits shown in the previous Section, but subdividing the data sample in bins of p_{T} and η.

Figure 3.30 shows the two dimensional distribution of p_{T} and η for background-subtracted $B^0 \to J/\psi K^{*0}$, $B^0 \to D^-\pi^+$ and $B_s^0 \to D_s^+\pi^+$ decays, with the chosen definition of the various bins. For the B^0 decays and 2011 data, we use the same bin ranges in order to allow a simple combination of the measurements of A_{P} from the two independent measurements. The bins, labelled as A and B contains events only in the case of $B^0 \to J/\psi K^{*0}$. For this bin the combination will not be performed and only the single measurements from $B^0 \to J/\psi K^{*0}$ will be given.

Decay	$\epsilon_{\rm rec}$ [%]	$\epsilon_{\rm PID}$ [%]	$\epsilon_{\rm mis-ID}$ [%]	N
$B_s^0 \to D_s^- \pi^+$	0.383 ± 0.003	73.0 ± 0.04	–	$16\,887 \pm 174$
$B^0 \to D_s^- \pi^+$	0.382 ± 0.003	73.0 ± 0.04	–	468 ± 95
$B^0 \to D^- \pi^+$	0.119 ± 0.001	–	0.32 ± 0.01	1.3 ± 0.4
$B_s^0 \to D_s^- K^+$	0.384 ± 0.002	–	2.67 ± 0.01	36 ± 7
$\Lambda_b^0 \to \Lambda_c^- \pi^+$	0.044 ± 0.001	–	0.51 ± 0.02	73 ± 60

Table 3.14: Reconstruction efficiencies, PID efficiencies, mis-ID efficiencies and expected number of background events for $B_s^0 \to D_s^- \pi^+$ decays. In the $B_s^0 \to D_s^- \pi^+$ row, the last column reports the number of events obtained from the global fit.

In the case of 2012 data we define a finer binning exploiting the larger statistics. The numerical values of the adopted bin ranges are reported in Tables 3.15 and 3.16.

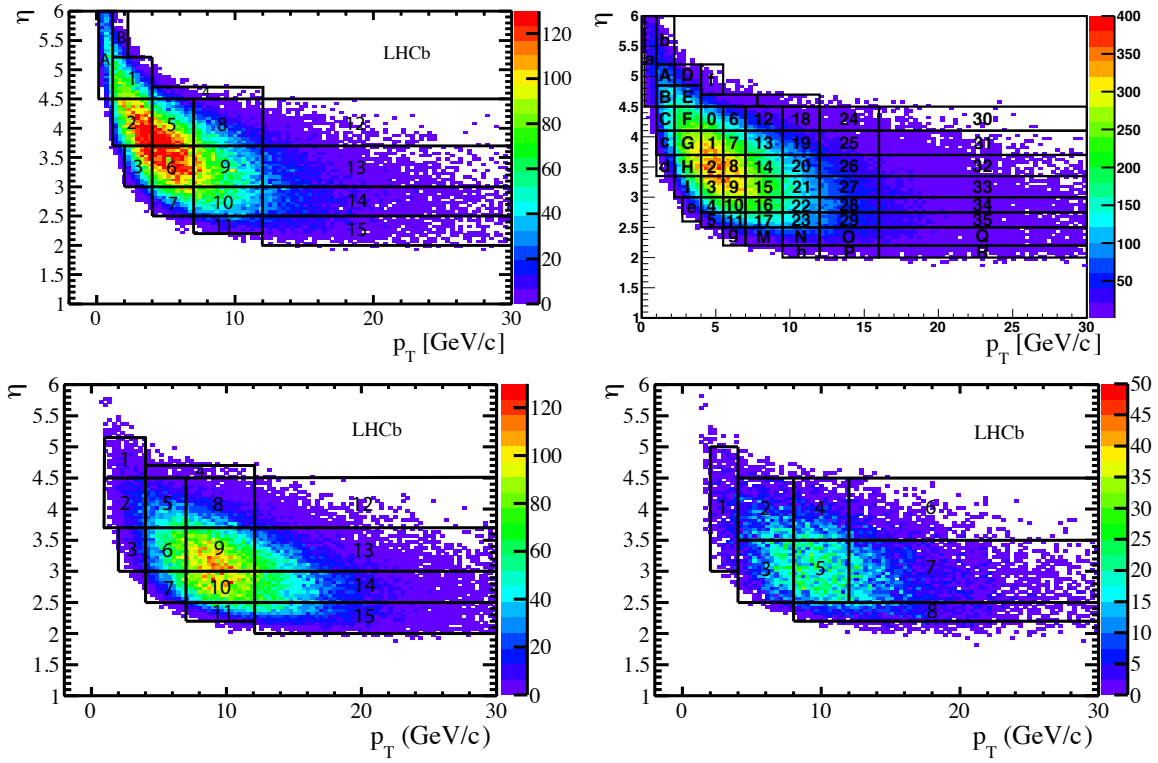

Figure 3.30: Distribution of $p_{\rm T}$ and η for background-subtracted (top left) $B^0 \to J/\psi K^{*0}$, (top right) $B^0 \to D^- \pi^+$ and (bottom) $B_s^0 \to D_s^+ \pi^+$.

Unbinned maximum likelihood fits to the mass and decay time distributions are performed for each bin. In the case of $B^0 \to J/\psi K^{*0}$ fit, the combinatorial background is described by the same function used in the corresponding global fit, with parameters fixed to those obtained in the global fit. In the case of the $B^0 \to D^- \pi^+$ and $B_s^0 \to D_s^- \pi^+$ fits, we also use the same model of the corresponding global fits, except that the function $\varepsilon_{\rm acc}^{comb}(t)$ is given by

$$\varepsilon_{\rm acc}^{comb}(t) = \frac{1}{2}\left[1 - {\rm erf}\left(\frac{p^{\rm comb} - t}{t}\right)\right], \tag{3.20}$$

Bin	$p_{\rm T}$ range [GeV/c]	η range
1	$1.0 - 4.0$	$4.5 - 5.2$
2	$1.0 - 4.0$	$3.7 - 4.5$
3	$2.0 - 4.0$	$3.0 - 3.7$
4	$4.0 - 12.0$	$4.5 - 4.7$
5	$4.0 - 7.0$	$3.7 - 4.5$
6	$4.0 - 7.0$	$3.0 - 3.7$
7	$4.0 - 7.0$	$2.5 - 3.0$
8	$7.0 - 12.0$	$3.7 - 4.5$
9	$7.0 - 12.0$	$3.0 - 3.7$
10	$7.0 - 12.0$	$2.5 - 3.0$
11	$7.0 - 12.0$	$2.2 - 2.5$
12	$12.0 - 30.0$	$3.7 - 4.5$
13	$12.0 - 30.0$	$3.0 - 3.7$
14	$12.0 - 30.0$	$2.5 - 3.0$
15	$12.0 - 30.0$	$2.0 - 2.5$
A	$0.2 - 1.0$	$4.5 - 6.0$
B	$1.0 - 2.2$	$5.2 - 6.0$

Table 3.15: Bin ranges used to study the dependence of $A_{\rm P}(B^0)$ on $p_{\rm T}$ and η from $B^0 \to J/\psi\, K^{*0}$ and $B^0 \to D^-\pi^+$ decays, with 2011 data.

Bin	$p_{\rm T}$ range [GeV/c]	η range
1	$2.0 - 4.0$	$3.0 - 5.0$
2	$4.0 - 8.0$	$3.5 - 4.5$
3	$4.0 - 8.0$	$2.5 - 3.5$
4	$8.0 - 12.0$	$3.5 - 4.5$
5	$8.0 - 12.0$	$2.5 - 3.5$
6	$12.0 - 30.0$	$3.5 - 4.5$
7	$12.0 - 30.0$	$2.5 - 3.5$
8	$8.0 - 30.0$	$2.2 - 2.5$

Table 3.16: Bin ranges used to study the dependence of $A_{\rm P}(B_s^0)$ on $p_{\rm T}$ and η from $B_s^0 \to D_s^-\pi^+$ decays.

where the parameter $p^{\rm comb}$ is left free to vary, whereas $\Gamma_1^{\rm comb}$ and $\Gamma_2^{\rm comb}$ are fixed to the values obtained in the global fit. In addition, the decay time acceptance for the signals is simplified as

$$\varepsilon_{\rm acc}\,(t) = \frac{1}{2}\left[1 - {\rm erf}\left(\frac{p_1 - t}{t}\right)\right](1 + p_3 t)\,. \tag{3.21}$$

The values of $A_{\rm P}(B^0)$ determined from each fit using $B^0 \to J/\psi\, K^{*0}$ and $B^0 \to D^-\pi^+$ decays using 2011 data are reported in Table 3.18. In the last raw it is also reported the weighted averages of $A_{\rm P}$ measured in each bin for $B^0 \to J/\psi\, K^{*0}$ and $B^0 \to D^-\pi^+$. The overall bin-by-bin agreement between the two sets of independent $A_{\rm P}$ measurements is evaluated with a χ^2 test, and turns out to be $\chi^2/{\rm ndf} = 0.50$. The values of $A_{\rm P}(B^0)$ determined from each fit using $B^0 \to J/\psi\, K^{*0}$ decay with 2012 data are reported in Table 3.19.

Bin	p_{T} range [GeV/c]	η range	Bin	p_{T} range [GeV/c]	η range
0	$4.0 - 5.5$	$4.10 - 4.50$	a	$0.2 - 1.0$	$4.50 - 6.00$
1	$4.0 - 5.5$	$3.70 - 4.10$	b	$1.0 - 2.2$	$5.20 - 6.00$
2	$4.0 - 5.5$	$3.35 - 3.7$	c	$1.0 - 2.2$	$3.70 - 4.10$
3	$4.0 - 5.5$	$3.00 - 3.35$	d	$1.0 - 2.2$	$3.35 - 3.70$
4	$4.0 - 5.5$	$2.75 - 3.00$	e	$2.7 - 4.0$	$2.60 - 3.00$
5	$4.0 - 5.5$	$2.50 - 2.75$	f	$4.0 - 5.5$	$4.70 - 5.20$
6	$5.5 - 7.0$	$4.10 - 4.50$	g	$5.5 - 7.0$	$2.20 - 2.50$
7	$5.5 - 7.0$	$3.70 - 4.10$	h	$9.5 - 12.0$	$2.00 - 2.20$
8	$5.5 - 7.0$	$3.35 - 3.70$	A	$1.0 - 2.2$	$4.85 - 5.20$
9	$5.5 - 7.0$	$3.00 - 3.35$	B	$1.0 - 2.2$	$4.50 - 4.85$
10	$5.5 - 7.0$	$2.75 - 3.00$	C	$1.0 - 2.2$	$4.10 - 4.50$
11	$5.5 - 7.0$	$2.50 - 2.75$	D	$2.2 - 4.0$	$4.85 - 5.20$
12	$7.0 - 9.5$	$4.10 - 4.50$	E	$2.2 - 4.0$	$4.50 - 4.85$
13	$7.0 - 9.5$	$3.70 - 4.10$	F	$2.2 - 4.0$	$4.10 - 4.50$
14	$7.0 - 9.5$	$3.35 - 3.70$	G	$2.2 - 4.0$	$3.70 - 4.10$
15	$7.0 - 9.5$	$3.00 - 3.35$	H	$2.2 - 4.0$	$3.35 - 3.70$
16	$7.0 - 9.5$	$2.75 - 3.00$	I	$2.2 - 4.0$	$3.00 - 3.35$
17	$7.0 - 9.5$	$2.50 - 2.75$	L	$4.0 - 12.0$	$4.50 - 4.70$
18	$9.5 - 12.0$	$4.10 - 4.50$	M	$7.0 - 9.5$	$2.20 - 2.50$
19	$9.5 - 12.0$	$3.70 - 4.10$	N	$9.5 - 12.0$	$2.20 - 2.50$
20	$9.5 - 12.0$	$3.35 - 3.70$	O	$12.0 - 16.0$	$2.20 - 2.50$
21	$9.5 - 12.0$	$3.00 - 3.35$	P	$12.0 - 16.0$	$2.00 - 2.20$
22	$9.5 - 12.0$	$2.75 - 3.00$	Q	$16.0 - 30.0$	$2.20 - 2.50$
23	$9.5 - 12.0$	$2.50 - 2.75$	R	$16.0 - 30.0$	$2.00 - 2.20$
24	$12.0 - 16.0$	$4.10 - 4.50$			
25	$12.0 - 16.0$	$3.70 - 4.10$			
26	$12.0 - 16.0$	$3.35 - 3.70$			
27	$12.0 - 16.0$	$3.00 - 3.35$			
28	$12.0 - 16.0$	$2.75 - 3.00$			
29	$12.0 - 16.0$	$2.50 - 2.75$			
30	$16.0 - 30.0$	$4.10 - 4.50$			
31	$16.0 - 30.0$	$3.70 - 4.10$			
32	$16.0 - 30.0$	$3.35 - 3.70$			
33	$16.0 - 30.0$	$3.00 - 3.35$			
34	$16.0 - 30.0$	$2.75 - 3.00$			
35	$16.0 - 30.0$	$2.50 - 2.75$			

Table 3.17: Bin ranges used to study the dependence of $A_{\mathrm{P}}(B^0)$ on p_{T} and η from $B^0 \to J/\psi\, K^{*0}$ for 2012 data set.

In the case of the $B_s^0 \to D_s^- \pi^+$ fit, since an accurate knowledge of the decay time resolution is important due to the fast oscillation of the B_s^0 meson, we determine the decay time resolution using the same method described in Sec. 3.2, applied for events belonging to each p_{T} and η bin. Figure 3.31 shows the decay time distributions for fake-B_s^0 candidates in the eight bins of p_{T} and η, with the results of double Gaussian fits overlaid. The widths $\sigma_{1,2}^{\mathrm{res}}$ and the fraction f_1^{res} of the first Gaussian function obtained from the fits are reported in Table 3.20. The values of $A_{\mathrm{P}}(B_s^0)$

Bin	$A_{\rm P}(B^0 \to J/\psi K^{*0})$	$A_{\rm P}(B^0 \to D^-\pi^+)$
1	0.004 ± 0.026	-0.033 ± 0.110
2	-0.016 ± 0.017	-0.013 ± 0.052
3	0.008 ± 0.027	-0.011 ± 0.074
4	-0.049 ± 0.084	0.235 ± 0.153
5	-0.022 ± 0.018	-0.010 ± 0.031
6	-0.034 ± 0.016	-0.025 ± 0.023
7	0.070 ± 0.032	0.032 ± 0.041
8	-0.036 ± 0.027	0.016 ± 0.032
9	-0.007 ± 0.017	-0.020 ± 0.015
10	-0.034 ± 0.023	-0.018 ± 0.017
11	-0.040 ± 0.062	-0.010 ± 0.042
12	-0.020 ± 0.065	-0.095 ± 0.069
13	-0.019 ± 0.031	0.020 ± 0.022
14	0.030 ± 0.031	0.013 ± 0.019
15	0.003 ± 0.048	-0.003 ± 0.027
A	-0.039 ± 0.050	–
B	0.052 ± 0.068	-
average	-0.0130 ± 0.0064	-0.0063 ± 0.0071

Table 3.18: Values of $A_{\rm P}(B^0)$ determined from $B^0 \to J/\psi K^{*0}$ and $B^0 \to D^-\pi^+$ fits in the various bins of $p_{\rm T}$ and η.

determined from the $B_s^0 \to D_s^-\pi^+$ fits are reported in Table 3.21 together with the signal yields. In the last column are reported the $A_{\rm P}(B_s^0)$ weighted average and the sum of the signal yields.

3.5 $A_{\rm P}$ integrated over $p_{\rm T}$ and η

We perform the integration in the ranges $4 < p_{\rm T} < 30$ GeV/c and $2.5 < \eta < 4.5$. This corresponds to integrate over bins N. 5-10 and 12-14 for the $A_P^{2011}(B^0)$, over bins N. 2-7 for $A_P^{2011}(B_s^0)$ and N. 0-35 for $A_P^{2012}(B^0)$.

The integrated value of $A_{\rm P}$ is given by

$$A_{\rm P} = \frac{\sum_i \frac{N_i}{\varepsilon_i} A_{{\rm P},i}}{\sum_i \frac{N_i}{\varepsilon_i}}, \tag{3.22}$$

where the index i runs over the bins, N_i is the number of signal events and ε_i is the efficiency defined as the number of selected events divided by the number of produced events in the i-th bins. The signal yield in each bin can be expressed as

$$N_i = \mathcal{L} \cdot \sigma_{b\bar{b}} \cdot 2 \cdot f_{b(s)} \cdot \mathcal{B} \cdot f_i \cdot \varepsilon_i, \tag{3.23}$$

where $\mathcal{L}$ is the integrated luminosity, $\sigma_{b\bar{b}}$ is the $b\bar{b}$ cross section, $f_{b(s)}$ is the $B^0_{(s)}$ hadronization fraction, f_i is the fraction of B mesons produced in the i-th bin and $\mathcal{B}$ is the branching fraction of the B decay. By substituting N_i/ε_i from Eq. 3.23 into Eq. 3.22, the integrated value of $A_{\rm P}$ becomes:

$$A_{\rm P} = \sum_i \omega_i A_{{\rm P},i}\,, \tag{3.24}$$

Bin	$A_{\rm P}(B^0 \to J/\psi K^{*0})$	Bin	$A_{\rm P}(B^0 \to J/\psi K^{*0})$
0	0.043 ± 0.026	a	0.027 ± 0.046
1	-0.023 ± 0.019	b	-0.081 ± 0.065
2	0.012 ± 0.018	c	0.013 ± 0.042
3	0.018 ± 0.021	d	-0.168 ± 0.082
4	-0.056 ± 0.033	e	-0.090 ± 0.074
5	-0.098 ± 0.056	f	-0.177 ± 0.118
6	0.003 ± 0.033	g	0.045 ± 0.099
7	-0.071 ± 0.021	h	-0.019 ± 0.194
8	-0.029 ± 0.019	A	0.069 ± 0.045
9	-0.017 ± 0.019	B	0.042 ± 0.038
10	0.029 ± 0.027	C	-0.064 ± 0.034
11	-0.013 ± 0.040	D	-0.067 ± 0.063
12	0.038 ± 0.039	E	0.001 ± 0.031
13	-0.031 ± 0.021	F	-0.030 ± 0.021
14	-0.001 ± 0.018	G	-0.032 ± 0.018
15	-0.014 ± 0.017	H	-0.018 ± 0.021
16	0.031 ± 0.021	I	-0.046 ± 0.029
17	-0.038 ± 0.026	L	-0.013 ± 0.048
18	0.008 ± 0.068	M	-0.032 ± 0.045
19	-0.007 ± 0.030	N	0.034 ± 0.043
20	-0.014 ± 0.025	O	-0.018 ± 0.038
21	-0.012 ± 0.024	P	0.320 ± 0.113
22	0.001 ± 0.028	Q	0.030 ± 0.039
23	-0.028 ± 0.029	R	0.059 ± 0.085
24	-0.064 ± 0.084		
25	-0.034 ± 0.042		
26	-0.048 ± 0.032		
27	-0.003 ± 0.028		
28	-0.012 ± 0.032		
29	0.030 ± 0.034		
30	0.143 ± 0.170		
31	-0.063 ± 0.064		
32	-0.085 ± 0.046		
33	-0.006 ± 0.039		
34	0.005 ± 0.042		
35	-0.028 ± 0.039		
average			-0.012 ± 0.004

Table 3.19: Values of $A_{\rm P}(B^0)$ determined from $B^0 \to J/\psi K^{*0}$ fits in the various bins of $p_{\rm T}$ and η using 2012 data

where $\omega_i = f_i / \sum_i f_i$.

The values of ω_i are determined using simulated events. Signal events for $B^0 \to J/\psi K^{*0}$, $B^0 \to D^-\pi^+$ and $B_s^0 \to D_s^-\pi^+$ are generated using PYTHIA without any generator level cut. Table 3.22 (Table 3.23) reports the values of ω_i for $B^0 \to J/\psi K^{*0}$ and $B^0 \to D^-\pi^+$ decays using the binning scheme of Table 3.15 (Table 3.17). Obviously, the values for these two decay modes

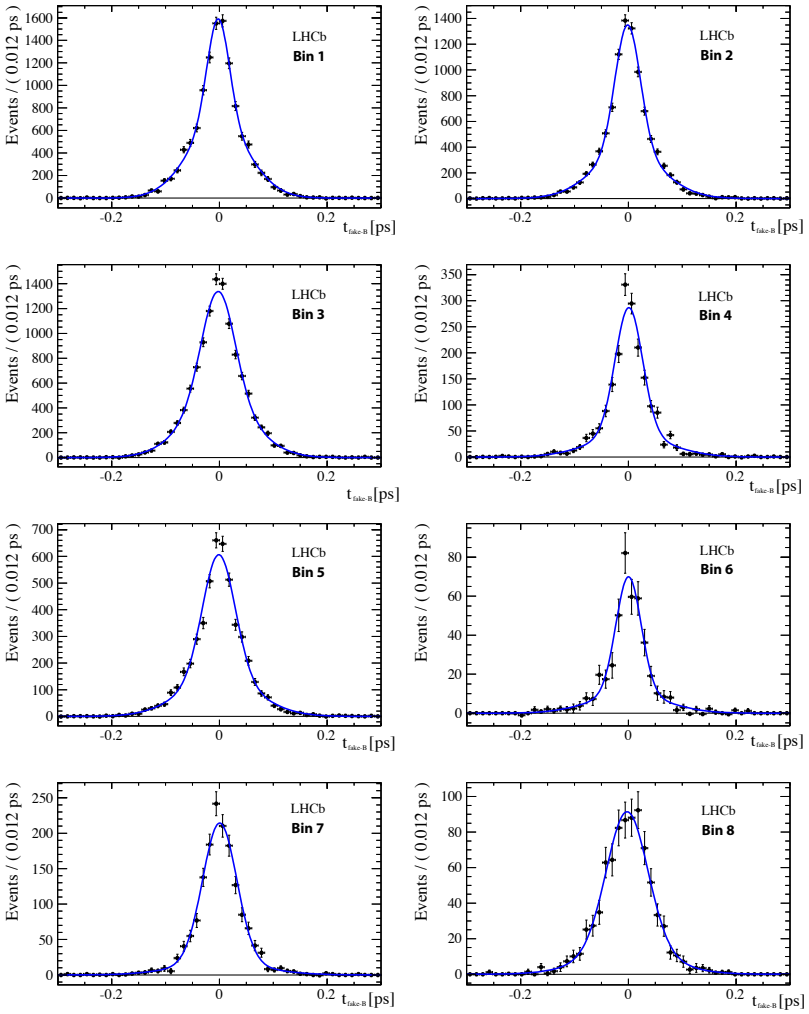

Figure 3.31: Decay time distributions of fake-B_s^0 candidates in bins of p_{T} and η, with the results of the fits overlaid.

Bin	σ_1^{res} [fs]	σ_1^{res} [fs]	f_1^{res}	Average width [fs]
1	21 ± 1	56 ± 1	0.35 ± 0.02	47.0 ± 0.4
2	23 ± 1	63 ± 1	0.51 ± 0.03	47.5 ± 0.5
3	31 ± 1	64 ± 2	0.50 ± 0.04	50.2 ± 0.4
4	25 ± 2	73 ± 4	0.68 ± 0.04	46.2 ± 1.2
5	30 ± 2	71 ± 3	0.60 ± 0.05	50.6 ± 0.7
6	23 ± 3	71 ± 7	0.68 ± 0.08	44.0 ± 2.6
7	32 ± 1	82 ± 7	0.83 ± 0.04	44.4 ± 1.4
8	38 ± 3	77 ± 9	0.75 ± 0.10	50.0 ± 2.1

Table 3.20: Decay time resolution parameters corresponding to the various bins of p_{T} and η for the $B_s^0 \to D_s^- \pi^+$ fits.

Bin	$A_{\rm P}(B_s^0 \to D_s^-\pi^+)$
1	-0.1475 ± 0.0895
2	-0.0471 ± 0.0513
3	0.0376 ± 0.0467
4	0.0582 ± 0.0537
5	0.0370 ± 0.0332
6	-0.0339 ± 0.0750
7	-0.0333 ± 0.0309
8	-0.0351 ± 0.0485
average	-0.0055 ± 0.0161

Table 3.21: Values of $A_{\rm P}(B_s^0)$ determined from $B_s^0 \to D_s^-\pi^+$ fits in the various bins of $p_{\rm T}$ and η with 2011 data.

Bin	$B^0 \to J/\psi K^{*0}$	$B^0 \to D^-\pi^+$
5	0.1698 ± 0.0008	0.1707 ± 0.0006
6	0.2432 ± 0.0009	0.2416 ± 0.0006
7	0.2222 ± 0.0009	0.2225 ± 0.0006
8	0.0662 ± 0.0006	0.0661 ± 0.0004
9	0.1129 ± 0.0007	0.1138 ± 0.0005
10	0.1150 ± 0.0007	0.1152 ± 0.0005
12	0.0113 ± 0.0003	0.0114 ± 0.0002
13	0.0276 ± 0.0004	0.0266 ± 0.0003
14	0.0318 ± 0.0004	0.0322 ± 0.0003

Table 3.22: Values of ω_i for $B^0 \to J/\psi K^{*0}$ and $B^0 \to D^-\pi^+$ decays determined from simulation using the 2011 B^0 binning scheme.

are compatible within statistical uncertainties. The values of ω_i for $B_s^0 \to D_s^-\pi^+$, $B^0 \to D^-\pi^+$ and $B^0 \to J/\psi K^{*0}$ decays, in the binning scheme of Table 3.16, are reported in Table 3.24.

The values of ω_i are also extracted from data using $B^0 \to J/\psi K^{*0}$ decays. In this case $\omega_i^{\rm data}$ is measured as

$$\omega_i^{\rm data} = \frac{N_i}{\varepsilon_i^{\rm sel} \cdot \varepsilon_i^{\rm trig} \cdot \varepsilon_i^{\rm PID}} \Big/ \sum_i \frac{N_i}{\varepsilon_i^{\rm sel} \cdot \varepsilon_i^{\rm trig} \cdot \varepsilon_i^{\rm PID}} \tag{3.25}$$

where:

- N_i is the yield in the i-th bin;
- $\varepsilon_i^{\rm sel}$ is defined as the number of selected events, without trigger and PID requirements, in the i-th bin divided by the number of produced events in that bin;
- $\varepsilon_i^{\rm PID}$ is defined as the number of selected events, including PID requirements, in the i-th bin divided by the number of selected events without trigger and PID requirements in that bin;
- $\varepsilon_i^{\rm trig}$ is defined as the number of selected events, including PID requirements and trigger, in the i-th bin divided by the number of selected events including PID requirements in that bin.

Bin	$B^0 \to J/\psi K^{*0}$	Bin	$B^0 \to J/\psi K^{*0}$
0	0.04594 ± 0.00049	1	0.06170 ± 0.00055
2	0.06651 ± 0.00057	3	0.07673 ± 0.00061
4	0.06136 ± 0.00055	5	0.06683 ± 0.00057
6	0.02698 ± 0.00038	7	0.03812 ± 0.00045
8	0.04277 ± 0.00047	9	0.05149 ± 0.00051
10	0.04229 ± 0.00047	11	0.04466 ± 0.00048
12	0.02029 ± 0.00033	13	0.03061 ± 0.00040
14	0.03581 ± 0.00043	15	0.04532 ± 0.00048
16	0.03722 ± 0.00044	17	0.04072 ± 0.00046
18	0.00708 ± 0.00020	19	0.01182 ± 0.00025
20	0.01474 ± 0.00028	21	0.01939 ± 0.00032
22	0.01652 ± 0.00030	23	0.01890 ± 0.00032
24	0.00337 ± 0.00014	25	0.00633 ± 0.00019
26	0.00860 ± 0.00022	27	0.01164 ± 0.00025
28	0.00996 ± 0.00023	29	0.01213 ± 0.00026
30	0.00105 ± 0.00008	31	0.00232 ± 0.00011
32	0.00370 ± 0.00014	33	0.00545 ± 0.00017
34	0.00515 ± 0.00017	35	0.00649 ± 0.00019

Table 3.23: Values of ω_i for $B^0 \to J/\psi K^{*0}$ and $B^0 \to D^-\pi^+$ decays determined from simulation using the 2012 B^0 binning scheme.

Bin	$B^0 \to D^-\pi^+$	$B_s^0 \to D_s^-\pi^+$	$B^0 \to J/\psi K^{*0}$
2	0.2671 ± 0.0006	0.2677 ± 0.0006	0.2667 ± 0.0009
3	0.4742 ± 0.0006	0.4702 ± 0.0006	0.4766 ± 0.0009
4	0.0579 ± 0.0004	0.0583 ± 0.0004	0.0564 ± 0.0005
5	0.1306 ± 0.0005	0.1316 ± 0.0005	0.1295 ± 0.0008
6	0.0170 ± 0.0002	0.0173 ± 0.0002	0.0175 ± 0.0003
7	0.0533 ± 0.0004	0.0550 ± 0.0003	0.0532 ± 0.0005

Table 3.24: Values of ω_i for $B^0 \to D^-\pi^+$, $B_s^0 \to D_s^-\pi^+$ and $B^0 \to J/\psi K^{*0}$ decays determined from simulation using the B_s^0 binning scheme.

The values of ε^{sel} and $\varepsilon^{\text{trig}}$ are determined from simulated events, while in order to account for the discrepancy between PID performances in data and simulated events, ε^{PID} is determined from data, using a dedicated calibration sample of $D^{*+} \to D^0(K^-\pi^+)\pi^+$ events and making use of the `PIDCalibTool` package [49]. As PID performances depend on kinematics, we reweight the events in order to match the momentum and pseudorapidity distributions of the D^0 daughters to those of Monte Carlo K^{*0} daughters. The efficiencies and the corresponding values of ω_i^{data} are calculated using B^0 and B_s^0 binning scheme as reported in Table 3.25 and Table 3.26 respectively.

Figures 3.33, 3.34 and 3.35 show the two-dimensional p_{T} and η distributions of Monte Carlo events generated without using generator level cuts and the total reconstruction efficiencies determined from simulated events for each of the three decay modes under study.

The values of ω_i and ω_i^{data} exhibit systematic differences at the 10% level. The difference in the central value between $A_{\text{P}}(B^0 \to J/\psi K^{*0})$ calculated using either ω_i or ω_i^{data} will be assigned

Bin	$\varepsilon^{\rm sel}$	$\varepsilon^{\rm PID}$	$\varepsilon^{\rm trig}$	$\omega_i^{\rm data}$
5	0.151 ± 0.002	0.7209 ± 0.0008	0.689 ± 0.014	0.1946 ± 0.0025
6	0.148 ± 0.002	0.7679 ± 0.0005	0.673 ± 0.012	0.2396 ± 0.0036
7	0.056 ± 0.001	0.7199 ± 0.0007	0.541 ± 0.018	0.1976 ± 0.0051
8	0.188 ± 0.004	0.5939 ± 0.0012	0.762 ± 0.023	0.0789 ± 0.0016
9	0.242 ± 0.004	0.7877 ± 0.0005	0.769 ± 0.014	0.1129 ± 0.0045
10	0.163 ± 0.003	0.7648 ± 0.0006	0.731 ± 0.017	0.1002 ± 0.0019
12	0.240 ± 0.010	0.3769 ± 0.0027	0.795 ± 0.060	0.0160 ± 0.0007
13	0.302 ± 0.008	0.7094 ± 0.0012	0.805 ± 0.026	0.0307 ± 0.0028
14	0.275 ± 0.007	0.7652 ± 0.0009	0.814 ± 0.026	0.0296 ± 0.0025

Table 3.25: Values of efficiencies and $\omega_i^{\rm data}$ for $B^0 \to J/\psi K^{*0}$ decays using the B^0 binning scheme.

Bin	$\varepsilon^{\rm sel}$	$\varepsilon^{\rm PID}$	$\varepsilon^{\rm trig}$	$\omega_i^{\rm data}$
2	0.160 ± 0.002	0.7316 ± 0.0004	0.698 ± 0.011	0.3064 ± 0.0020
3	0.104 ± 0.001	0.7545 ± 0.0006	0.643 ± 0.010	0.4644 ± 0.0030
4	0.220 ± 0.005	0.6324 ± 0.0005	0.782 ± 0.022	0.0640 ± 0.0015
5	0.217 ± 0.003	0.7823 ± 0.0012	0.770 ± 0.014	0.0873 ± 0.0019
6	0.255 ± 0.009	0.4617 ± 0.0007	0.808 ± 0.019	0.0238 ± 0.0008
7	0.288 ± 0.006	0.7543 ± 0.0022	0.809 ± 0.043	0.0541 ± 0.0027

Table 3.26: Values of efficiencies and $\omega_i^{\rm data}$ for $B^0 \to J/\psi K^{*0}$ decays using the B_s^0 binning scheme.

as a systematic uncertainty for both $A_{\rm P}(B^0)$ and $A_{\rm P}(B_s^0)$. The differences between the values of ω_i predicted by PYTHIA for B^0 and B_s^0 mesons, reported in Table 3.24, are in fact very small.

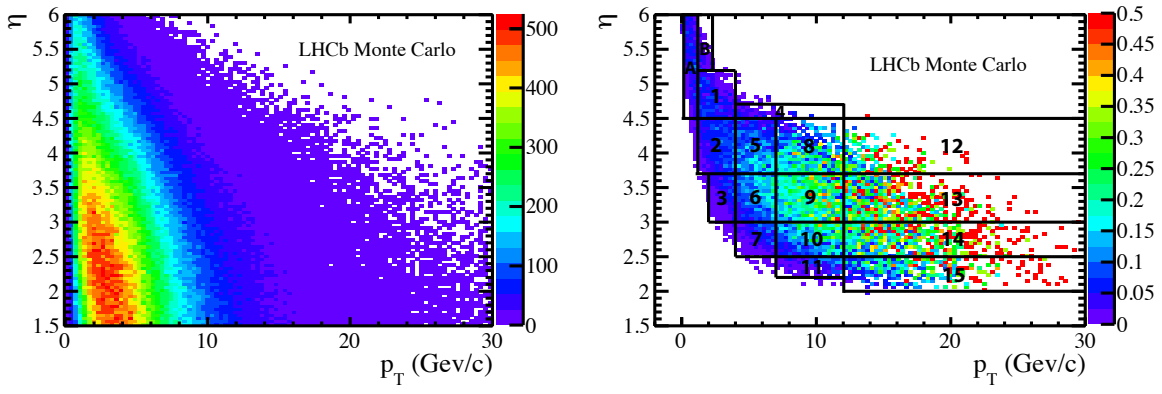

Figure 3.32: Distribution of $p_{\rm T}$ and η for simulated B^0 mesons produced without generator level cuts at $\sqrt{s} = 7\,\text{TeV}$ (left), and efficiency as function of $p_{\rm T}$ and η (right) for $B^0 \to J/\psi K^{*0}$ decays with 2011 data.

Bin	ε^{sel}	ε^{PID}	$\varepsilon^{\text{trig}}$	ω_i^{data}
1	0.104 ± 0.004	0.711 ± 0.003	0.602 ± 0.031	0.053 ± 0.001
2	0.130 ± 0.003	0.788 ± 0.002	0.690 ± 0.024	0.062 ± 0.003
3	0.124 ± 0.003	0.797 ± 0.001	0.670 ± 0.024	0.066 ± 0.003
4	0.086 ± 0.003	0.786 ± 0.001	0.657 ± 0.027	0.081 ± 0.002
5	0.040 ± 0.002	0.767 ± 0.001	0.636 ± 0.043	0.070 ± 0.003
6	0.015 ± 0.001	0.749 ± 0.002	0.547 ± 0.065	0.064 ± 0.008
7	0.107 ± 0.005	0.625 ± 0.004	0.703 ± 0.044	0.029 ± 0.001
8	0.160 ± 0.005	0.765 ± 0.002	0.713 ± 0.029	0.039 ± 0.003
9	0.167 ± 0.005	0.808 ± 0.002	0.709 ± 0.026	0.043 ± 0.003
10	0.142 ± 0.004	0.805 ± 0.001	0.707 ± 0.026	0.050 ± 0.003
11	0.089 ± 0.003	0.792 ± 0.001	0.686 ± 0.037	0.042 ± 0.001
12	0.045 ± 0.002	0.778 ± 0.002	0.589 ± 0.046	0.047 ± 0.002
13	0.124 ± 0.006	0.506 ± 0.005	0.800 ± 0.056	0.022 ± 0.001
14	0.206 ± 0.006	0.708 ± 0.002	0.791 ± 0.030	0.028 ± 0.003
15	0.229 ± 0.006	0.802 ± 0.001	0.772 ± 0.025	0.032 ± 0.004
16	0.199 ± 0.005	0.818 ± 0.001	0.774 ± 0.024	0.040 ± 0.004
17	0.156 ± 0.005	0.809 ± 0.002	0.786 ± 0.031	0.032 ± 0.003
18	0.096 ± 0.004	0.798 ± 0.002	0.680 ± 0.035	0.041 ± 0.001
19	0.153 ± 0.011	0.373 ± 0.009	0.850 ± 0.103	0.009 ± 0.001
20	0.251 ± 0.011	0.619 ± 0.004	0.810 ± 0.048	0.012 ± 0.002
21	0.276 ± 0.010	0.774 ± 0.002	0.809 ± 0.037	0.013 ± 0.003
22	0.257 ± 0.009	0.816 ± 0.002	0.805 ± 0.033	0.017 ± 0.003
23	0.213 ± 0.009	0.812 ± 0.002	0.803 ± 0.039	0.015 ± 0.003
24	0.158 ± 0.007	0.812 ± 0.002	0.776 ± 0.042	0.017 ± 0.002
25	0.145 ± 0.016	0.297 ± 0.012	0.906 ± 0.168	0.006 ± 0.001
26	0.260 ± 0.015	0.506 ± 0.007	0.863 ± 0.072	0.007 ± 0.002
27	0.300 ± 0.014	0.710 ± 0.004	0.858 ± 0.049	0.008 ± 0.002
28	0.265 ± 0.011	0.801 ± 0.002	0.848 ± 0.043	0.011 ± 0.003
29	0.267 ± 0.012	0.806 ± 0.002	0.845 ± 0.046	0.009 ± 0.003
30	0.220 ± 0.010	0.813 ± 0.002	0.821 ± 0.047	0.010 ± 0.002
31	0.204 ± 0.033	0.204 ± 0.017	0.875 ± 0.331	0.002 ± 0.001
32	0.367 ± 0.030	0.373 ± 0.011	0.929 ± 0.115	0.003 ± 0.001
33	0.343 ± 0.023	0.562 ± 0.008	0.856 ± 0.078	0.004 ± 0.002
34	0.327 ± 0.018	0.724 ± 0.005	0.872 ± 0.059	0.005 ± 0.002
35	0.326 ± 0.019	0.755 ± 0.004	0.859 ± 0.061	0.005 ± 0.002
36	0.288 ± 0.016	0.774 ± 0.003	0.869 ± 0.058	0.006 ± 0.002

Table 3.27: Values of efficiencies and ω_i^{data} for $B^0 \to J/\psi K^{*0}$ decays using the 2012 B^0 binning scheme and data.

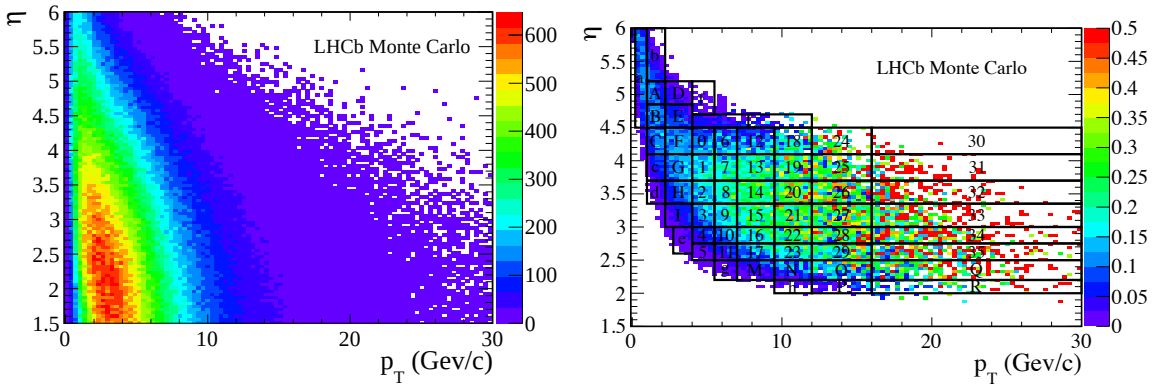

Figure 3.33: Distribution of $p_{\rm T}$ and η for simulated B^0 mesons produced without generator level cuts at $\sqrt{s} = 8\,\text{TeV}$ (left), and efficiency as function of $p_{\rm T}$ and η (right) for $B^0 \to J/\psi\, K^{*0}$ decays with 2012 data.

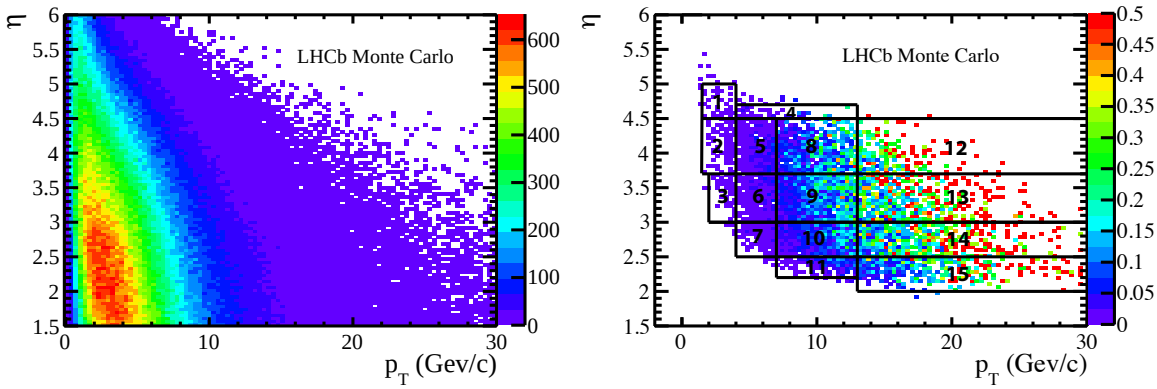

Figure 3.34: Distribution of $p_{\rm T}$ and η for simulated B^0 mesons produced without generator level cuts at $\sqrt{s} = 7\,\text{TeV}$ (left), and efficiency as function of $p_{\rm T}$ and η (right) for $B^0 \to D^-\pi^+$ decays with 2011 data.

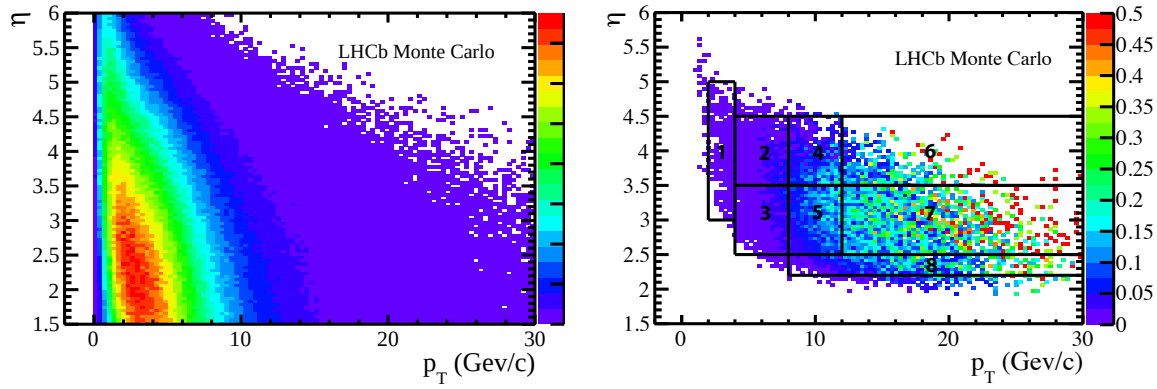

Figure 3.35: Distribution of $p_{\rm T}$ and η for simulated B^0 mesons produced without generator level cuts at $\sqrt{s} = 7\,\text{TeV}$ (left), and efficiency as function of $p_{\rm T}$ and η (right) for $B^0_s \to D^-_s\pi^+$ with 2011 data.

3.6 Systematic uncertainties

We consider the following sources of systematic uncertainties affecting the determination of the production asymmetries

- invariant mass
  - inaccuracies in the shapes of any component (signals, combinatorial and partially reconstructed backgrounds);
- decay time
  - inaccuracies in the resolution and acceptance functions;
  - uncertainties on the external inputs ($|q/p|_{B^0}$, $|q/p|_{B^0_s}$, Δm_d, Δm_s, $\Delta\Gamma_s$, Γ_d and Γ_s);

To estimate the contribution of each single source we repeat the fit for each single bin after having modified the baseline fit model. The shifts from the relevant baseline values are accounted for as systematic uncertainties.

To estimate a systematic uncertainty related to the parameterization of QED radiation effects on the signal mass distributions, the parameter s is varied by $\pm1\sigma$ of the corresponding value obtained from fits to simulated events. A systematic uncertainty related to the invariant mass resolution model is estimated by repeating the fit using a single Gaussian function. The systematic uncertainty related to the parameterization of the mass shape for the combinatorial background is investigated by replacing the exponential function with a straight line. Concerning the partially reconstructed background, we assess a systematic uncertainty by repeating the fits while excluding the low mass sideband, *i.e.* applying the requirements $m > 5.20\,\mathrm{GeV}/c^2$ for the $B^0 \to D^-\pi^+$ decays and $m > 5.33\,\mathrm{GeV}/c^2$ for $B^0_s \to D^-_s\pi^+$ decays. In the case of $B^0_s \to D^-_s\pi^-$ we fixed the number of $B^0 \to D^-_s\pi^+$ to the one estimated in Table 3.14 and we assign as systematic uncertanty by varying the yield by $\pm1\sigma$. To estimate an uncertainty related to the parameterization of signal decay time acceptances, we exchange the $B^0 \to J/\psi\,K^{*0}$ and $B \to D\pi$ acceptance functions. Effects of inaccuracies in the knowledge of the decay time resolution are estimated by rescaling the widths of the baseline model in order to obtain an average resolution width differing by ±8 fs, corresponding to the uncertainty estimated in Sec. 3.2, with respect to the baseline one. Effects due to a possible bias in the decay time are also accounted for by introducing a bias of ±2 fs in the decay time resolution model.

The determination of the systematic uncertainties related to the $|q/p|$ input value needs a special treatement, as $A_{\rm P}$ turns out to be correlated with $|q/p|$. For this reasons, any variation of $|q/p|$ turns into the same shift of $A_{\rm P}$ in each of the kinematic bins, *i.e.* such systematic uncertainties are 100% correlated between the various bins. Such a correlation must be taken into account when averaging $A_{\rm P}(B^0)$ measurements from $B^0 \to J/\psi\,K^{*0}$ and $B^0 \to D^-\pi^+$ decays, or when integrating over $p_{\rm T}$ and η.

A summary of the numerical values of all systematic uncertainties is reported in Tables 3.28 - 3.32.

Bin	Γ_d	Δm_d	$\lvert q/p \rvert$	DTR	FSR	DTB	SMS	CMS	DTA	Total	Uncorr. total
1	–	–	0.0013	–	0.0001	–	0.0007	0.0001	0.0002	0.0015	0.0007
2	–	0.0001	0.0013	–	0.0002	–	0.0010	–	–	0.0017	0.0010
3	0.0001	–	0.0013	–	–	–	0.0047	–	0.0001	0.0049	0.0047
4	0.0001	0.0007	0.0013	–	0.0009	0.0001	0.0033	–	0.0017	0.0041	0.0039
5	–	0.0001	0.0013	–	–	–	0.0005	–	–	0.0014	0.0005
6	–	0.0001	0.0013	–	0.0002	–	0.0012	–	–	0.0018	0.0012
7	–	0.0005	0.0013	–	0.0001	–	0.0024	–	0.0001	0.0028	0.0025
8	–	0.0002	0.0013	–	0.0001	–	0.0006	–	–	0.0015	0.0006
9	–	–	0.0013	–	–	–	0.0007	–	–	0.0015	0.0007
10	–	0.0004	0.0013	–	0.0002	–	0.0023	0.0002	–	0.0027	0.0024
11	–	0.0008	0.0013	–	0.0011	0.0001	0.0020	–	0.0001	0.0027	0.0024
12	–	0.0004	0.0013	–	0.0004	–	0.0005	–	0.0002	0.0015	0.0008
13	–	0.0001	0.0013	–	0.0005	–	0.0038	–	–	0.0040	0.0038
14	–	0.0003	0.0013	–	0.0004	–	0.0010	0.0001	–	0.0017	0.0011
15	–	0.0002	0.0013	–	0.0006	–	0.0006	–	–	0.0016	0.0009
A	–	0.0007	0.0013	–	0.0002	0.0001	0.0006	0.0001	0.0001	0.0016	0.0010
B	0.0001	0.0002	0.0013	–	0.0003	–	0.0021	0.0002	–	0.0025	0.0021

Table 3.28: Systematic uncertainties on $A_{\rm P}(B^0)$ from $B^0 \to J/\psi\, K^{*0}$ decays corresponding to each kinematic bin. No value is reported when it turns out to be less then 0.0001. The various acronyms refer to: decay time resolution (DTR), final state radiation (FSR), decay time bias (DTB), signal mass shape (SMS), combinatorial background mass shape (CMS), decay time acceptance (DTA). In the second to last column we report the total systematic uncertainty, whereas in the last column we report the total systematic error with the correlated systematic component excluded.

Bin	Γ_d	Δm_d	$\lvert q/p \rvert$	DTR	FSR	DTB	SMS	CMS	DTA	Total	Uncorr. total
0	0.0006	0.0003	0.0013	0.0001	0.0002	–	0.0001	0.0028	0.0028	0.0042	0.0040
1	0.0004	0.0004	0.0013	–	0.0003	–	–	0.0001	0.0002	0.0015	0.0007
2	0.0001	0.0006	0.0013	–	0.0003	–	–	0.0003	0.0003	0.0015	0.0008
3	0.0004	0.0003	0.0013	–	0.0004	–	–	–	–	0.0015	0.0006
4	0.0001	0.0013	0.0013	0.0001	0.0002	0.0001	–	0.0018	0.0018	0.0032	0.0029
5	0.0003	0.0033	0.0013	–	0.0009	–	–	0.0029	0.0030	0.0056	0.0054
6	0.0006	0.0013	0.0013	–	0.0001	–	–	0.0016	0.0015	0.0029	0.0026
7	0.0009	0.0021	0.0013	–	0.0003	–	–	0.0001	0.0001	0.0026	0.0023
8	–	0.0011	0.0013	–	0.0002	–	–	0.0002	0.0002	0.0017	0.0012
9	–	0.0002	0.0013	–	0.0002	–	–	–	0.0001	0.0013	0.0003
10	0.0006	0.0002	0.0013	–	0.0003	–	–	0.0012	0.0012	0.0022	0.0018
11	–	0.0002	0.0013	–	0.0013	–	–	0.0001	0.0001	0.0019	0.0013
12	0.0010	0.0014	0.0013	–	0.0004	–	–	0.0018	0.0018	0.0033	0.0031
13	–	0.0014	0.0013	–	0.0004	–	–	0.0001	0.0001	0.0020	0.0015
14	0.0002	0.0010	0.0013	–	0.0001	–	–	0.0006	0.0006	0.0019	0.0013
15	0.0001	0.0016	0.0013	–	0.0004	–	–	0.0004	0.0004	0.0022	0.0017
16	0.0005	0.0007	0.0013	–	–	–	–	0.0031	0.0031	0.0047	0.0045
17	0.0004	0.0001	0.0013	–	0.0005	–	–	0.0001	0.0001	0.0015	0.0007
18	0.0003	0.0042	0.0013	–	0.0013	–	–	0.0026	0.0026	0.0059	0.0057
19	0.0001	0.0003	0.0013	–	0.0002	–	–	0.0004	0.0004	0.0015	0.0007
20	0.0001	0.0024	0.0013	–	0.0003	–	–	0.0002	0.0002	0.0028	0.0024
21	0.0004	0.0011	0.0013	–	0.0008	–	–	0.0013	0.0013	0.0027	0.0023
22	0.0001	0.0009	0.0013	–	0.0004	–	–	–	–	0.0016	0.0010
23	0.0002	0.0001	0.0014	0.0001	0.0001	0.0001	0.0001	0.0012	0.0012	0.0022	0.0017
24	0.0010	0.0039	0.0013	0.0001	–	0.0001	–	0.0053	0.0053	0.0086	0.0085
25	0.0005	0.0002	0.0013	–	0.0003	–	–	0.0024	0.0024	0.0037	0.0034
26	0.0005	0.0009	0.0013	–	0.0004	–	–	0.0018	0.0018	0.0031	0.0028
27	–	0.0003	0.0013	–	0.0005	–	–	0.0002	0.0002	0.0015	0.0007
28	0.0003	0.0010	0.0013	–	0.0008	–	–	0.0018	0.0018	0.0031	0.0029
29	0.0009	0.0009	0.0014	0.0001	–	0.0001	0.0001	0.0053	0.0053	0.0077	0.0076
30	0.0013	0.0047	0.0012	0.0001	0.0010	0.0001	–	0.0164	0.0155	0.0230	0.0230
31	0.0012	0.0033	0.0013	–	0.0013	–	–	0.0043	0.0043	0.0073	0.0071
32	0.0018	0.0004	0.0013	–	–	–	–	0.0049	0.0049	0.0073	0.0072
33	0.0002	0.0035	0.0013	–	0.0009	0.0001	–	0.0018	0.0016	0.0045	0.0043
34	–	0.0017	0.0013	–	0.0007	–	–	0.0001	0.0001	0.0023	0.0018
35	0.0002	0.0005	0.0013	–	0.0006	–	–	–	–	0.0015	0.0008

Table 3.29: Systematic uncertainties on $A_{\rm P}(B^0)$ from $B^0 \to J/\psi K^{*0}$ decays corresponding to bin N. 0-35 for 2012 data. No value is reported when it turns out to be less then 0.0001. The various acronyms refer to: decay time resolution (DTR), final state radiation (FSR), decay time bias (DTB), signal mass shape (SMS), combinatorial background mass shape (CMS), decay time acceptance (DTA). In the second to last column we report the total systematic uncertainty, whereas in the last column we report the total systematic error with the correlated systematic component excluded.

Bin	Γ_d	Δm_d	$\lvert q/p \rvert$	DTR	FSR	DTB	SMS	CMS	DTA	Total	Uncorr. total
a	0.0004	0.0015	0.0014	0.0001	0.0002	0.0001	0.0001	0.0021	0.0017	0.0034	0.0031
b	0.0007	0.0017	0.0014	0.0001	0.0010	0.0001	0.0001	0.0076	0.0067	0.0104	0.0103
c	0.0004	0.0023	0.0013	–	0.0013	–	–	0.0031	0.0029	0.0052	0.0050
d	0.0020	0.0113	0.0013	0.0001	0.0038	0.0001	–	0.0149	0.0147	0.0242	0.0242
e	0.0010	0.0012	0.0013	–	0.0004	–	–	0.0090	0.0091	0.0130	0.0129
f	0.0226	0.0074	0.0013	0.0167	0.0162	0.0168	0.0165	0.0094	0.0012	0.0418	0.0418
g	0.0017	0.0058	0.0013	0.0001	0.0031	0.0001	–	0.0030	0.0031	0.0082	0.0080
h	0.0018	0.0011	0.0013	–	0.0065	–	–	0.0172	0.0169	0.0251	0.0251
A	0.0012	0.0036	0.0013	–	0.0011	0.0001	–	0.0056	0.0054	0.0088	0.0087
B	0.0011	0.0025	0.0013	–	0.0002	–	–	0.0004	0.0004	0.0031	0.0028
C	0.0005	0.0002	0.0013	–	0.0002	–	–	0.0035	0.0039	0.0054	0.0053
D	0.0006	0.0016	0.0013	–	0.0019	–	–	0.0051	0.0051	0.0078	0.0077
E	0.0001	0.0012	0.0013	–	0.0004	–	–	0.0003	0.0003	0.0019	0.0013
F	–	0.0011	0.0013	–	0.0001	–	–	–	–	0.0017	0.0011
G	0.0005	0.0008	0.0013	–	0.0002	–	–	0.0008	0.0009	0.0020	0.0015
H	–	0.0003	0.0013	–	0.0005	–	–	0.0003	0.0002	0.0015	0.0007
I	0.0001	–	0.0013	–	0.0002	–	–	0.0017	0.0017	0.0027	0.0024
L	0.0007	0.0017	0.0013	–	0.0002	–	–	0.0040	0.0040	0.0061	0.0060
M	0.0002	0.0013	0.0013	0.0001	0.0007	0.0001	0.0001	–	0.0001	0.0020	0.0015
N	0.0003	0.0027	0.0013	–	0.0001	–	–	0.0002	0.0002	0.0030	0.0027
O	0.0003	0.0004	0.0013	–	0.0006	–	–	0.0009	0.0009	0.0020	0.0015
P	0.0053	0.0106	0.0013	0.0001	0.0055	0.0002	–	0.0335	0.0236	0.0430	0.0430
Q	0.0008	0.0006	0.0013	–	0.0001	–	–	0.0005	0.0004	0.0018	0.0012
R	0.0018	0.0053	0.0013	0.0001	0.0045	0.0001	–	0.0156	0.0175	0.0246	0.0245

Table 3.30: Systematic uncertainties on $A_{\rm P}(B^0)$ from $B^0 \to J/\psi K^{*0}$ decays corresponding to bin N. A-R and N. a-h for 2012 data. No value is reported when it turns out to be less then 0.0001. The various acronyms refer to: decay time resolution (DTR), final state radiation (FSR), decay time bias (DTB), signal mass shape (SMS), combinatorial background mass shape (CMS), decay time acceptance (DTA). In the second to last column we report the total systematic uncertainty, whereas in the last column we report the total systematic error with the correlated systematic component excluded.

Bin	Γ_d	Δm_d	$\lvert q/p \rvert$	DTR	FSR	DTB	SMS	CMS	PMS	DTA	Total	Uncorr. Total
1	–	0.0022	0.0013	0.0002	0.0001	0.0002	0.0050	–	0.0022	–	0.0060	0.0059
2	–	0.0005	0.0013	–	0.0001	–	0.0018	–	0.0033	–	0.0040	0.0038
3	–	0.0003	0.0013	–	–	–	0.0006	–	0.0021	–	0.0025	0.0022
4	0.0001	0.0014	0.0013	0.0001	0.0007	–	0.0128	0.0008	0.0198	0.0053	0.0243	0.0242
5	–	0.0002	0.0013	–	0.0001	–	0.0020	–	0.0016	0.0001	0.0029	0.0026
6	–	0.0004	0.0013	–	–	–	0.0006	–	–	0.0001	0.0015	0.0007
7	0.0001	0.0001	0.0013	–	–	–	0.0026	–	0.0003	0.0024	0.0038	0.0036
8	0.0001	0.0004	0.0013	–	0.0001	–	0.0030	–	0.0022	0.0023	0.0046	0.0044
9	–	0.0001	0.0013	–	–	–	0.0011	–	0.0002	0.0001	0.0017	0.0011
10	–	0.0003	0.0013	–	–	–	0.0003	–	0.0003	0.0003	0.0014	0.0006
11	–	0.0003	0.0013	–	–	–	0.0042	–	0.0016	0.0003	0.0047	0.0045
12	0.0001	0.0001	0.0013	–	0.0001	–	0.0007	–	0.0016	0.0002	0.0021	0.0018
13	0.0001	0.0001	0.0013	–	0.0001	–	0.0014	–	0.0009	0.0018	0.0029	0.0025
14	–	0.0001	0.0013	–	–	–	0.0019	–	0.0006	0.0008	0.0026	0.0021
15	–	0.0001	0.0013	–	–	–	0.0009	–	0.0017	0.0006	0.0024	0.0020

Table 3.31: Systematic uncertainties on $A_{\rm P}(B^0)$ from $B^0 \to D^-\pi^+$ decays corresponding to each kinematic bin. No value is reported when it turns out to be less then 0.0001. The various acronyms refer to: decay time resolution (DTR), final state radiation (FSR), decay time bias (DTB), signal mass shape (SMS), combinatorial background mass shape (CMS), partially reconstructed background mass shape (PMS), decay time acceptance (DTA). In the second to last column we report the total systematic uncertainty, whereas in the last column we report the total systematic error with the correlated systematic component excluded.

Bin	Γ_s	Δm_s	$\lvert q/p \rvert$	DTR	FSR	DTB	$\Delta\Gamma_s$	B0	SMS	CMS	PMS	DTA	Total	Uncorr. total
1	0.0001	0.0050	0.0030	0.0158	0.0002	0.0007	0.0002	–	0.0058	0.0002	0.0072	0.0029	0.0194	0.0192
2	0.0002	0.0086	0.0030	0.0044	0.0003	0.0032	0.0003	–	0.0028	0.0013	0.0033	0.0004	0.0116	0.0112
3	–	0.0038	0.0030	0.0044	–	0.0007	–	–	0.0058	0.0003	0.0002	0.0002	0.0088	0.0083
4	–	0.0003	0.0030	0.0051	–	0.0004	0.0001	–	0.0005	0.0002	0.0014	0.0002	0.0061	0.0053
5	–	0.0018	0.0030	0.0037	0.0001	0.0018	0.0002	–	0.0017	0.0006	0.0011	0.0010	0.0059	0.0051
6	0.0010	0.0036	0.0030	0.0032	0.0012	0.0027	0.0010	0.0010	0.0036	0.0010	0.0064	–	0.0099	0.0095
7	–	0.0020	0.0030	0.0032	0.0001	0.0009	0.0002	–	0.0009	0.0002	0.0006	0.0001	0.0050	0.0040
8	–	0.0017	0.0030	0.0025	0.0001	0.0002	–	–	0.0033	0.0012	0.0035	0.0010	0.0067	0.0059

Table 3.32: Systematic uncertainties on $A_{\rm P}(B_s^0)$ from $B_s^0 \to D_s^- \pi^+$ decays corresponding to each kinematic bin. No value is reported when it turns out to be less then 0.0001. The various acronyms refer to: variation of $B^0 \to D_s^- \pi$ fraction (B0), decay time resolution (DTR), final state radiation (FSR), decay time bias (DTB), signal mass shape (SMS), combinatorial background mass shape (CMS), partially reconstructed background mass shape (PMS), decay time acceptance (DTA). In the second to last column we report the total systematic uncertainty, whereas in the last column we report the total systematic error with the correlated systematic component excluded.

Bin	$A_{\rm P}(B^0)$
1	$0.0016 \pm 0.0253 \pm 0.0016$
2	$-0.0158 \pm 0.0162 \pm 0.0015$
3	$0.0055 \pm 0.0254 \pm 0.0016$
4	$0.0160 \pm 0.0736 \pm 0.0067$
5	$-0.0189 \pm 0.0158 \pm 0.0032$
6	$-0.0311 \pm 0.0132 \pm 0.0014$
7	$0.0556 \pm 0.0254 \pm 0.0020$
8	$-0.0145 \pm 0.0205 \pm 0.0027$
9	$-0.0142 \pm 0.0111 \pm 0.0015$
10	$-0.0236 \pm 0.0138 \pm 0.0014$
11	$-0.0190 \pm 0.0348 \pm 0.0034$
12	$-0.0550 \pm 0.0473 \pm 0.0020$
13	$0.0067 \pm 0.0180 \pm 0.0021$
14	$0.0177 \pm 0.0162 \pm 0.0023$
15	$-0.0018 \pm 0.0236 \pm 0.0020$
A	$-0.0391 \pm 0.0501 \pm 0.0016$
B	$0.0523 \pm 0.0684 \pm 0.0025$

Table 3.33: Combined values of $A_{\rm P}(B^0)$ from $B^0 \to J/\psi K^{*0}$ and $B^0 \to D^-\pi^+$ decays, corresponding to the various kinematic bins. The first uncertainties are statistical and the second systematic.

3.7 Final results in bins of $p_{\rm T}$ and η

Since we have two measurements of $A_{\rm P}(B^0)$ with 2011 data, one from $B^0 \to J/\psi K^{*0}$ and one from $B^0 \to D^-\pi^+$ decays, we need to average them, accounting for their partial correlation. We write the average ($\bar{x}$) of two partially correlated measurements (x_1 and x_2) as

$$\bar{x} = \frac{x_1/\sigma_1^2 + x_2/\sigma_2^2 - \rho(x_1+x_2)/(\sigma_1\sigma_2)}{1/\sigma_1^2 + 1/\sigma_2^2 - 2\rho/(\sigma_1\sigma_2)}, \tag{3.26}$$

where $\sigma_i^2 = \sigma_{i\,\rm s}^2 + \sigma_{i\,\rm u}^2 + \sigma_{i\,\rm c}^2$, the subscripts s, u and c stand for statistical, uncorrelated and correlated, respectively, and $\rho = \sigma_{1\,\rm c}\sigma_{2\,\rm c}/(\sigma_1\sigma_2)$. The variance of $\bar{x}$ is

$$\sigma^2 = \frac{1-\rho^2}{1/\sigma_1^2 + 1/\sigma_2^2 - 2\rho/(\sigma_1\sigma_2)}. \tag{3.27}$$

The variance can be decomposed into statistical and systematic components by subtracting in quadrature the statistical uncertainty

$$\sigma_{\rm stat}^2 = 1/(1/\sigma_{1\,\rm s}^2 + 1/\sigma_{2\,\rm s}^2), \tag{3.28}$$

$$\sigma_{\rm syst}^2 = \sigma^2 - \sigma_{\rm stat}^2. \tag{3.29}$$

The final results for $A_{\rm P}(B^0)$ with 2011 data are summarized in Table 3.33, whereas those $A_{\rm P}(B_s^0)$ can be found in 3.34. The final results for $A_{\rm P}(B^0)$ from 2012 are reported in Table 3.35.

Bin	$A_{\rm P}(B_s^0)$
1	$-0.1475 \pm 0.0895 \pm 0.0192$
2	$-0.0471 \pm 0.0513 \pm 0.0112$
3	$0.0376 \pm 0.0467 \pm 0.0083$
4	$0.0582 \pm 0.0537 \pm 0.0053$
5	$0.0370 \pm 0.0332 \pm 0.0051$
6	$-0.0339 \pm 0.0750 \pm 0.0095$
7	$-0.0333 \pm 0.0309 \pm 0.0040$
8	$-0.0351 \pm 0.0485 \pm 0.0059$

Table 3.34: Values of $A_{\rm P}(B^0)$ from $B_s^0 \to D_s^- \pi^+$ decays, corresponding to the various kinematic bins. The first uncertainties are statistical and the second systematic.

Bin	$A_{\rm P}(B^0 \to J/\psi K^{*0})$	Bin	$A_{\rm P}(B^0 \to J/\psi K^{*0})$
0	$0.043 \pm 0.026 \pm 0.0042$	a	$0.027 \pm 0.046 \pm 0.0034$
1	$-0.023 \pm 0.019 \pm 0.0015$	b	$-0.081 \pm 0.065 \pm 0.0104$
2	$0.012 \pm 0.018 \pm 0.0015$	c	$0.013 \pm 0.042 \pm 0.0052$
3	$0.018 \pm 0.021 \pm 0.0015$	d	$-0.168 \pm 0.082 \pm 0.0242$
4	$-0.056 \pm 0.033 \pm 0.0032$	e	$-0.090 \pm 0.074 \pm 0.0130$
5	$-0.098 \pm 0.056 \pm 0.0056$	f	$-0.177 \pm 0.118 \pm 0.0418$
6	$0.003 \pm 0.029 \pm 0.0026$	g	$0.045 \pm 0.099 \pm 0.0082$
7	$-0.071 \pm 0.021 \pm 0.0026$	h	$-0.019 \pm 0.194 \pm 0.0251$
8	$-0.029 \pm 0.019 \pm 0.0017$	A	$0.069 \pm 0.045 \pm 0.0088$
9	$-0.017 \pm 0.019 \pm 0.0013$	B	$0.042 \pm 0.038 \pm 0.0031$
10	$0.029 \pm 0.027 \pm 0.0022$	C	$-0.064 \pm 0.034 \pm 0.0054$
11	$-0.013 \pm 0.040 \pm 0.0019$	D	$-0.067 \pm 0.063 \pm 0.0078$
12	$0.038 \pm 0.039 \pm 0.0033$	E	$0.001 \pm 0.031 \pm 0.0019$
13	$-0.031 \pm 0.021 \pm 0.0020$	F	$-0.030 \pm 0.021 \pm 0.0017$
14	$-0.001 \pm 0.018 \pm 0.0019$	G	$-0.032 \pm 0.018 \pm 0.0020$
15	$-0.014 \pm 0.017 \pm 0.0022$	H	$-0.018 \pm 0.021 \pm 0.0015$
16	$0.031 \pm 0.021 \pm 0.0047$	I	$-0.046 \pm 0.029 \pm 0.0027$
17	$-0.038 \pm 0.026 \pm 0.0015$	L	$-0.013 \pm 0.048 \pm 0.0061$
18	$0.008 \pm 0.068 \pm 0.0059$	M	$-0.032 \pm 0.045 \pm 0.0020$
19	$-0.007 \pm 0.030 \pm 0.0015$	N	$0.034 \pm 0.043 \pm 0.0030$
20	$-0.014 \pm 0.025 \pm 0.0028$	O	$-0.018 \pm 0.038 \pm 0.0020$
21	$-0.012 \pm 0.024 \pm 0.0027$	P	$0.320 \pm 0.113 \pm 0.0430$
22	$0.001 \pm 0.028 \pm 0.0016$	Q	$0.030 \pm 0.039 \pm 0.0018$
23	$-0.028 \pm 0.029 \pm 0.0022$	R	$0.059 \pm 0.085 \pm 0.0246$
24	$-0.064 \pm 0.084 \pm 0.0086$		
25	$-0.034 \pm 0.042 \pm 0.0037$		
26	$-0.048 \pm 0.032 \pm 0.0031$		
27	$-0.003 \pm 0.028 \pm 0.0015$		
28	$-0.012 \pm 0.032 \pm 0.0031$		
29	$0.030 \pm 0.034 \pm 0.0077$		
30	$0.143 \pm 0.170 \pm 0.0230$		
31	$-0.063 \pm 0.064 \pm 0.0073$		
32	$-0.085 \pm 0.046 \pm 0.0073$		
33	$-0.006 \pm 0.039 \pm 0.0045$		
34	$0.005 \pm 0.042 \pm 0.0023$		
35	$-0.028 \pm 0.039 \pm 0.0015$		

Table 3.35: Values of $A_{\rm P}(B^0)$ determined from $B^0 \to J/\psi K^{*0}$ fits in the various bins of $p_{\rm T}$ and η using 2012 data. The first uncertainties are statistical and the second systematic.

3.8 Final integrated results

The overall production asymmetries integrated over the $4 < p_{\mathrm{T}} < 30$ GeV/c and $2.5 < \eta < 4.5$ are determined. The integrated values of A_{P} are obtained according to Eq. 3.24, where the values of ω_i are obtained from simulation, as discussed in Sec. 3.5. The central values become

$$A_{\mathrm{P}}(B^0)^{2011}_{B^0\to J/\psi K^{*0}} = \quad -0.0033, \tag{3.30}$$

$$A_{\mathrm{P}}(B^0)^{2012}_{B^0\to J/\psi K^{*0}} = \quad -0.0146, \tag{3.31}$$

$$A_{\mathrm{P}}(B^0)_{B^0\to D^-\pi^+} = \quad -0.0038, \tag{3.32}$$

$$A_{\mathrm{P}}(B^0)_{B^0_s\to D^-_s\pi^+} = \quad 0.0109. \tag{3.33}$$

The statistical, uncorrelated and correlated systematic uncertainties are calculated by error propagation as

$$\sigma_{\mathrm{stat}} = \sqrt{\sum_i \left(\omega_i\, \sigma_{\mathrm{stat}}\left(A_{\mathrm{P},i}\right)\right)^2} \tag{3.34}$$

$$\sigma_{\mathrm{uncorr.\,syst}} = \sqrt{\sum_i \left(\omega_i\, \sigma_{\mathrm{uncorr.\,syst}}\left(A_{\mathrm{P},i}\right)\right)^2}, \tag{3.35}$$

$$\sigma_{\mathrm{corr.\,syst}} = \sigma_{\mathrm{corr.\,syst}}\left(A_{\mathrm{P}}\right), \tag{3.36}$$

where the last equation is due to the equality of the correlated uncertainties in all bins.

Other systematic effects need to be taken into account. The statistical uncertainties on the values of ω_i are propagated as

$$\sigma_\omega = \sqrt{\sum_i \left(A_{\mathrm{P},i}\, \sigma_{\mathrm{stat}}\left(\omega_i\right)\right)^2}. \tag{3.37}$$

Furthermore, as already mentioned in Sec. 3.5, we account for a systematic uncertainty related to the determination of ω_i from simulation. This is defined as the difference between the central values of $A_{\mathrm{P}}(B^0 \to J/\psi K^{*0})$ calculated using either ω_i or ω_i^{data}, and is found to be 0.0024 using the B^0 binning scheme, and 0.0034 using the B^0_s binning scheme. The various systematic uncertainties on A_{P} determined from $B^0 \to J/\psi K^{*0}$, $B^0 \to D^-\pi^+$ and $B^0_s \to D^-_s\pi^+$ decays are summarized in Table 3.36.

Finally, the average of the two integrated measurements of $A_{\mathrm{P}}(B^0)$ from $B^0 \to J/\psi K^{*0}$ and $B^0 \to D^-\pi^+$ decays is made. As for the bin-by-bin average discussed in Sec. 3.7, we separate the systematic uncertainties into uncorrelated and correlated components

$$\begin{aligned}
A_{\mathrm{P}}(B^0)^{2011}_{B^0\to J/\psi K^{*0}} &= -0.0033 \pm 0.0096\,(\mathrm{stat}) \pm 0.0004\,(\mathrm{uncorr.\,syst}) \pm 0.0028\,(\mathrm{corr.\,syst}),\\
A_{\mathrm{P}}(B^0)^{2012}_{B^0\to J/\psi K^{*0}} &= -0.0146 \pm 0.0063\,(\mathrm{stat}) \pm 0.0011\,(\mathrm{uncorr.\,syst}) \pm 0.0028\,(\mathrm{corr.\,syst}),\\
A_{\mathrm{P}}(B^0 \to D^-\pi^+) &= -0.0038 \pm 0.0124\,(\mathrm{stat}) \pm 0.0009\,(\mathrm{uncorr.\,syst}) \pm 0.0028\,(\mathrm{corr.\,syst}).
\end{aligned}$$

Assuming no dependence of the production asymmetry on $\sqrt{s}$ between $\sqrt{s} = 7\,\mathrm{TeV}$ and $\sqrt{s} = 8\,\mathrm{TeV}$ and considering the partial correlation amongst the three measurements, the final average is

$$A_{\mathrm{P}}(B^0) = -0.0100 \pm 0.0048\,(\mathrm{stat}) \pm 0.0029\,(\mathrm{syst}).$$

The final result for $A_{\mathrm{P}}(B^0_s)$ is

$$A_{\mathrm{P}}(B^0_s) = \quad 0.0109 \pm 0.0261\,(\mathrm{stat}) \pm 0.0066\,(\mathrm{syst}).$$

Uncertainty	$B^0 \to J/\psi K^{*0}$ [2011]	$B^0 \to J/\psi K^{*0}$ [2012]	$B^0 \to D^-\pi^+$	$B_s^0 \to D_s^-\pi^+$
Statistical	0.0096	0.0063	0.0124	0.0261
Uncorr. systematic	0.0004	0.0011	0.0009	0.0048
Weights	0.0001	0.0001	0.0001	0.0001
Total uncorr. systematic	0.0004	0.0011	0.0009	0.0048
Corr. systematic (from bins)	0.0013	0.0013	0.0013	0.0030
Corr. systematic (from weights)	0.0024	0.0024	0.0024	0.0034
Total Corr. systematic	0.0028	0.0028	0.0028	0.0045

Table 3.36: Statistical and systematic uncertainties on the integrated production asymmetries. The total uncorrelated systematic uncertainties are obtained by summing in quadrature the uncertainties in the previous three rows.

$p_{\rm T}$ [GeV/c]	$A_{\rm P}$ ($B^0 \to J/\psi K^{*0}$)	$A_{\rm P}$ ($B^0 \to D^-\pi^+$)	$A_{\rm P}$ (B^0 average)
4–7	$0.0056 \pm 0.0138 \pm 0.0010 \pm 0.0027$	$-0.0008 \pm 0.0187 \pm 0.0015 \pm 0.0027$	$0.0033 \pm 0.0111 \pm 0.0028$
7–12	$-0.0241 \pm 0.0126 \pm 0.0010 \pm 0.0027$	$-0.0107 \pm 0.0113 \pm 0.0011 \pm 0.0027$	$-0.0167 \pm 0.0084 \pm 0.0028$
12–30	$0.0027 \pm 0.0213 \pm 0.0016 \pm 0.0027$	$-0.0014 \pm 0.0164 \pm 0.0014 \pm 0.0027$	$0.0001 \pm 0.0130 \pm 0.0029$

Table 3.37: Values of the production asymmetry $A_{\rm P}(B^0)$ in bins of $p_{\rm T}$ from $B^0 \to J/\psi K^{*0}$ and $B^0 \to D^-\pi^+$ decays. The last column contains the averages of the first two columns. In the first two columns, the first uncertainties are statistical, the second and the third systematic (uncorrelated and correlated, respectively). In the last column, the first uncertainty is statistical and the second systematic.

In Tables 3.37 and 3.38 we report the values of $A_{\rm P}(B^0)$ integrated over η and $p_{\rm T}$, whereas those of $A_{\rm P}(B_s^0)$ can be found in Tables 3.40 and 3.41. The dependencies of $A_{\rm P}(B^0)$ and $A_{\rm P}(B_s^0)$ on $p_{\rm T}$ and η are shown in Figs. 3.37 and 3.38.

η	$A_{\rm P}$ ($B^0 \to J/\psi K^{*0}$)	$A_{\rm P}$ ($B^0 \to D^-\pi^+$)	$A_{\rm P}$ (B^0 average)
2.5–3.0	$0.0343 \pm 0.0209 \pm 0.0017 \pm 0.0027$	$0.0150 \pm 0.0252 \pm 0.0022 \pm 0.0027$	$0.0264 \pm 0.0161 \pm 0.0030$
3.0–3.7	$-0.0250 \pm 0.0116 \pm 0.0008 \pm 0.0027$	$-0.0199 \pm 0.0154 \pm 0.0006 \pm 0.0027$	$-0.0232 \pm 0.0093 \pm 0.0028$
3.7–4.5	$-0.0258 \pm 0.0148 \pm 0.0004 \pm 0.0013$	$-0.0069 \pm 0.0231 \pm 0.0021 \pm 0.0027$	$-0.0203 \pm 0.0125 \pm 0.0021$

Table 3.38: Values of the production asymmetry $A_{\rm P}(B^0)$ in bins of η from $B^0 \to J/\psi K^{*0}$ and $B^0 \to D^-\pi^+$ decays with 2011 data. The last column contains the averages of the first two columns. In the first two columns, the first uncertainties are statistical, the second and the third systematic (uncorrelated and correlated, respectively). In the last column, the first uncertainty is statistical and the second systematic.

$p_{\rm T}$ [GeV/c]	$A_{\rm P}(B^0)$	η	$A_{\rm P}(B^0)$
4.0–5.5	$-0.0192 \pm 0.0132 \pm 0.0018$	2.50–2.75	$-0.0474 \pm 0.0229 \pm 0.0025$
5.5–7.0	$-0.0166 \pm 0.0111 \pm 0.0015$	2.75–3.00	$-0.0063 \pm 0.0146 \pm 0.0021$
7.0–9.5	$-0.0058 \pm 0.0093 \pm 0.0017$	3.00–3.35	$-0.0021 \pm 0.0100 \pm 0.0015$
9.5–12.0	$-0.0111 \pm 0.0124 \pm 0.0017$	3.35–3.70	$-0.0082 \pm 0.0098 \pm 0.0016$
12.0–16.0	$-0.0122 \pm 0.0149 \pm 0.0025$	3.70–4.10	$-0.0367 \pm 0.0108 \pm 0.0016$
16.0–30.0	$-0.0205 \pm 0.0203 \pm 0.0026$	4.10–4.50	$0.0267 \pm 0.0169 \pm 0.0025$

Table 3.39: Values of the production asymmetry $A_{\rm P}(B^0_s)$ in bins of $p_{\rm T}$ and η from $B^0 \to J/\psi K^{*0}$ decays with 2012 data. The first uncertainties are statistical and the second systematic.

$p_{\rm T}$ [GeV/c]	$A_{\rm P}(B^0_s)$
4.0–8.0	$0.0069 \pm 0.0351 \pm 0.0067$
8.0–12.0	$0.0435 \pm 0.0283 \pm 0.0039$
12.0–30.0	$-0.0334 \pm 0.0296 \pm 0.0038$

Table 3.40: Values of the production asymmetry $A_{\rm P}(B^0_s)$ in bins of $p_{\rm T}$ from $B^0_s \to D^-_s\pi^+$ decays. The first uncertainties are statistical and the second systematic.

η	$A_{\rm P}(B^0_s)$
2.5–3.5	$0.0315 \pm 0.0342 \pm 0.0060$
3.5–4.5	$-0.0286 \pm 0.0412 \pm 0.0088$

Table 3.41: Values of the production asymmetry $A_{\rm P}(B^0_s)$ in bins of η from $B^0_s \to D^-_s\pi^+$ decays. The first uncertainties are statistical and the second systematic.

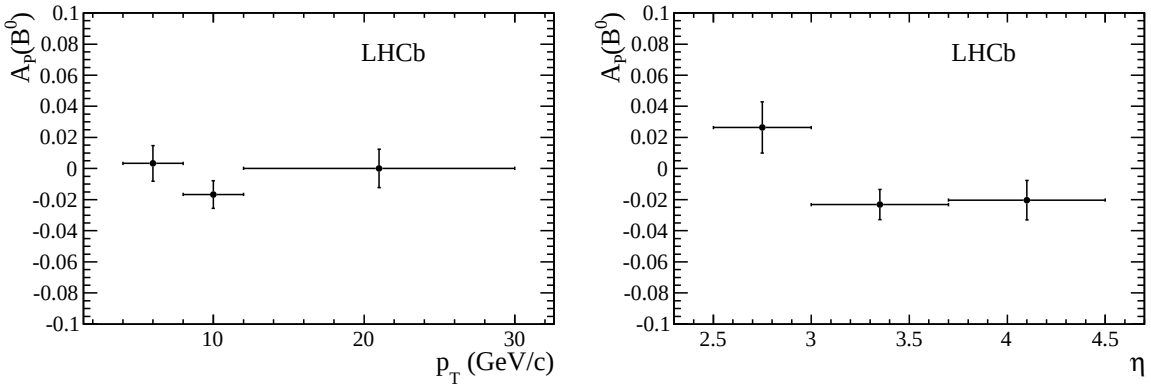

Figure 3.36: Dependence of $A_{\rm P}(B^0)$ on (left) $p_{\rm T}$ and (right) η for 2011 data.

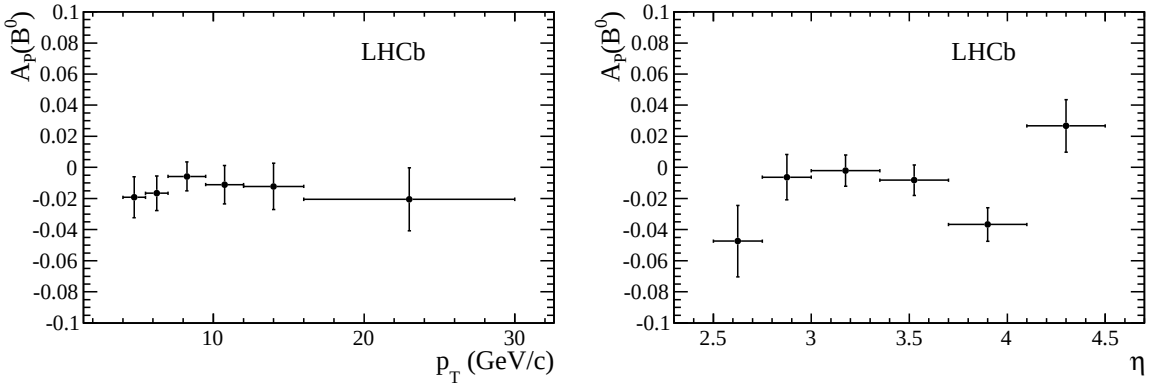

Figure 3.37: Dependence of $A_{\rm P}(B^0)$ on (left) $p_{\rm T}$ and (right) η for 2012 data.

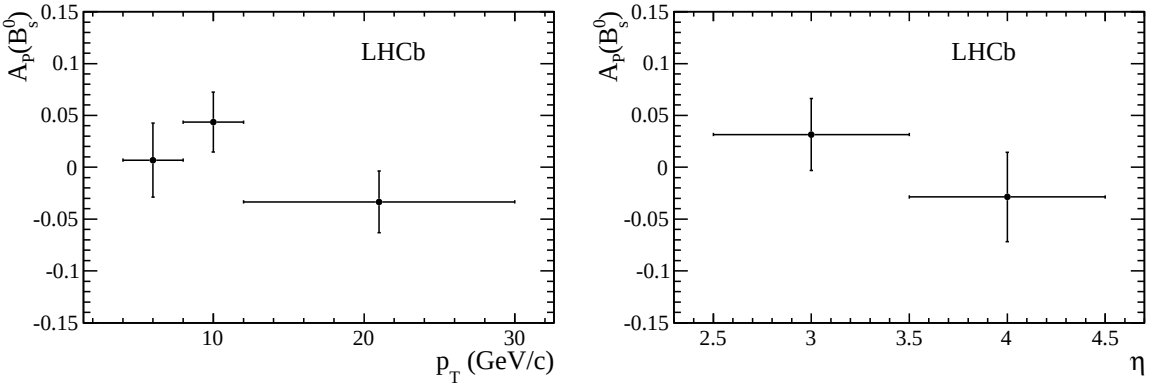

Figure 3.38: Dependence of $A_{\rm P}(B_s^0)$ on (left) $p_{\rm T}$ and (right) η.

3.9 Summary

We measure the production asymmetries of B^0 and B_s^0 mesons in pp collisions at $\sqrt{s} = 7\,\text{TeV}$, using a data sample corresponding to an integrated luminosity of $1.0\,\text{fb}^{-1}$. The measurements are performed in bins of p_T and η. The results are summarized in Tables 3.33 and 3.34.

The overall production asymmetries, integrated in the ranges $4 < p_\text{T} < 30\,\text{GeV}/c$ and $2.5 < \eta < 4.5$, are determined to be

$$A_\text{P}(B^0) = (-1.00 \pm 0.48\,(\text{stat}) \pm 0.29\,(\text{syst}))\%,$$

$$A_\text{P}(B_s^0) = (\quad 1.09 \pm 2.61\,(\text{stat}) \pm 0.66\,(\text{syst}))\%.$$

where in the case of $A_\text{P}(B^0)$ we assume the dependence of production asymmetry on $\sqrt{s}$ to be negligibile.

Conclusion

This thesis presents the analysis performed to determine the production asymmetries of B^0 and B_s^0 using a data samples collected during the 2011 and 2012 data takings at two different values of the centre of mass energy $\sqrt{s} = 7\,\text{TeV}$ and at $\sqrt{s} = 8\,\text{TeV}$, corresponding respectively to an integrated luminosity of 1 fb^{-1} and of 2 fb^{-1}.

All the results reported in this thesis represent original contributions of the author.

The measurements of the production asymmetries are performed in bins of p_T and η of the B-meson. Their values provide constraints that can be used to test different models of B-meson production mechanisms. Furthermore, once integrated using the appropriate weights to combine for any reconstructed B^0 and B_s^0 decay modes, they can be used to derive an effective production asymmetry, as inputs for precise CP violation measurements with the LHCb detector.

Assuming a negligible dependence of the production asymmetry on $\sqrt{s}$ in the range $\sqrt{s} = 7$-$8\,\text{TeV}$, the values of the production asymmetries, integrated in the ranges $4 < p_\text{T} < 30\,\text{GeV}/c$ and $2.5 < \eta < 4.5$, are determined to be:

$$A_\text{P}(B^0) = (-1.00 \pm 0.48 \pm 0.29)\%,$$

$$A_\text{P}(B_s^0) = (\ \ 1.09 \pm 2.61 \pm 0.61)\%,$$

where the first uncertainty is statistical and the second is systematic. The measurement of $A_\text{P}(B^0)$ is performed using the full statistics collected by LHCb so far, corresponding to an integrated luminosity of $3\,\text{fb}^{-1}$, while the measurement of $A_\text{P}(B_s^0)$ is realized with the first $1\,\text{fb}^{-1}$, leaving room for improvement. No clear evidence of dependences on the values of p_T and η is observed. Shown results are the most precise measurements available up to date.

Bibliography

[1] R. N. Cahn, *The eighteen arbitrary parameters of the standard model in your everyday life*, Rev. Mod. Phys **68**, 951 (1996).

[2] M. K. Gaillard, P. D. Grannis and F. J. Sciulli, *The standard model of particle physics*, Rev. Mod. Phys **71**, S96 (1999).

[3] [CMS Collaboration] S. Chatrchyan *et al.*, *Observation of a new boson at a mass of 125 GeV with the CMS experiment at the LHC*, Phys. Lett. **B716**, 30 (2012).

[4] [ATLAS Collaboration] G. Aad *et al.*, *Observation of a new particle in the search for the Standard Model Higgs boson with the ATLAS detector at the LHC*, Phys. Lett. **B716**, 1 (2012).

[5] O'Luanaigh, C. *New results indicate that new particle is a Higgs boson*, (2013), CERN.

[6] [Particle Data Group] K.A. Olive *et al.*, *The Review of Particle Physics*, Chin. Phys. C, **38**, 090001 (2014).

[7] C. S. Wu *et al.*, *Experimental Test of Parity Conservation in Beta Decay*, Phys. Rev. **105**, 1413 (1957)

[8] T. D. Lee and C. N. Yang *Question of Parity Conservation in Weak Interaction*, Phys. Rev. **104**, 254-258 (1956).

[9] R. L. Garwin *et al.*, *Observations of the Failure of Conservation of Parity and Charge Conjugation in Meson Decays: the Magnetic Moment of the Free Muon*, Phys. Rev. **105**, 1415 - 1417 (1957)

[10] L. D. Landau *et al.*, *On the Conservation Laws in Weak Interactions*, Nucl. Phys. **3**, 127 (1957)

[11] J. I. Friedman and V. L. Telegdi *Nuclear Emulsion Evidence for Parity Nonconservation in the Decay Chain* $\pi^+ \to \mu^+ \to e^+$, Phys. Rev. **106**, 1290 - 1293 (1957).

[12] J. H. Christenson, J. W. Cronin, V. L. Fitch, and R. Turlay, *Evidence for the* 2π *decay of the* K_2^0 *meson* Phys. Rev. Lett. **13**, 138 (1964).

[13] [BABAR Collaboration] B. Aubert, *et al.*, *Observation Of CP Violation In The* B^0 *Meson System*, Phys. Rev. Lett. **87**, 091801 (2001).

[14] [Belle Collaboration] K. Abe *et al.*, *Observation Of Large CP Violation In The Neutral B Meson System*, Phys. Rev. Lett. **87**, 091802 (2001).

[15] [BABAR Collaboration] B. Aubert, *et al.*, *Observation Of Direct CP Violation in $B^0 \to K^+\pi^-$ decays*, Phys. Rev. Lett. **93**, 131801 (2004).

[16] N. Cabibbo, *Unitary Symmetry and Leptonic Decays*, Phys. Rev. Lett. **10**, 531 (1963)

[17] M. Kobayashi and T. Maskawa, *CP-Violation in the Renormalizable Theory of Weak Interaction*, Prog. Theor. Phys. **49**, 652 (1973)

[18] L. Wolfenstein, *Parametrization of the Kobayashi-Maskawa Matrix*, Phys. Rev. Lett. **51**, 1945 (1983)

[19] C. Jarlskog, *Commutator of the quark mass matrices in the Standard Electroweak model and a measure of maximal CP violation*, Phys. Rev. Lett. **55**, 1039 (1985)

[20] UTfit Collaboration web pages, www.utfit.org/.

[21] M. Ciuchini *et al.*, *2000 CKM-Triangle Analysis. A Critical Review with Updated Experimental Inputs and Theoretical Parameters*, JHEP **0107**, 013 (2001).

[22] V. Weisskopf and E. P. Wigner, *Calculation of the natural brightness of spectral lines on the basis of Dirac's theory (In German)*, Z. Phys. **63**, 54 (1930);

[23] V. Weisskopf and E. P. Wigner, *Over the natural line width in the radiation of the harmonius oscillator (In German)*, Z. Phys. **65**, 18 (1930).

[24] I. I. Bigi and A. I. Sanda, *CP violation*, Cambridge University Press, (2000).

[25] A. J. Buras, W. Słominski and H. Steger, Nucl. Phys. **B245**, 369 (1984).

[26] [LHCb Collaboration] A. A. Alves *et al.*, *The LHCb Detector at the LHC*, JINST **3**, S08005 (2008).

[27] L. Evans and P. Bryant, *The CERN Large Hadron Collider: Accelerator and Experiments*, JINST **3**, S08001 (2008).

[28] [LHCb Collaboration] W. Flegel, M. Losasso, F. Rohner *et al.*, *LHCb Magnet: Technical Design Report*, CERN-LHCC-2000-007.

[29] [LHCb Collaboration] P.R. Barbosa-Marinho *et al.*, *LHCb VELO (VErtex LOcator): Technical Design Report*, CERN-LHCC-2001-011.

[30] [LHCb Collaboration] R. Aaij *et al.*, *Performance of the LHCb Vertex Locator*, CERN-LHCB-DP-2014-001, `arXiv:1405.7808`.

[31] [LHCb Collaboration], *LHCb reoptimized detector design and performance*, CERN-LHCC-2003-030.

[32] [LHCb Collaboration], *Inner Tracker Technical Design Report*, CERN-LHCC-2002-029.

[33] [LHCb Collaboration], *Outer Tracker Technical Design Report*, CERN-LHCC-2001-024.

[34] [LHCb Collaboration], *RICH Technical Design Report*, CERN-LHCC-2000-037.

[35] M. Adinolfi *et al.*, *Performance of the LHCb RICH detector at the LHC*, Eur. Phys. J. **C73** (2013) 2431, `arXiv:1211.6759`

[36] [LHCb Collaboration], *Calorimeters Technical Design Report*, CERN-LHCC-2000-036.

[37] [LHCb Collaboration], *Muon System Technical Design Report*, CERN-LHCC-2001-010.

[38] [LHCb Collaboration], *LHCb trigger System Technical Design Report*, CERN-LHCC-2003-066

[39] Worldwide LHC Computing Grid web page, `wlcg.web.cern.ch`.

[40] DIRAC web page, `diracgrid.org`

[41] M. Pivk *et al.*, *sPlot: a quick introduction,* `arXiv:physics/0602023`

[42] L. Breiman, J. H. Friedman, R. A. Olshen, and C. J. Stone, *Classification and regression trees*, Wadsworth international group, Belmont, California, USA, 1984

[43] B. P. Roe *et al.*, *Boosted decision trees as an alternative to artificial neural networks for particle identification*, Nucl. Instrum. Meth. **A543** (2005) 577, `arXiv:physics/0408124`

[44] A. Carbone *et al.*, *Measurement of time-dependent CP-violating asymmetries in* $B^0 \to \pi^+\pi^-$ *and* $B_s^0 \to K^+K^-$ *decays at LHCb*, LHCb-ANA-2013-040

[45] K. S. Cranmer, *Kernel estimation in high-energy physics*, Comput. Phys. Commun. **136** (2001) 198, `arXiv:hep-ex/0011057`

[46] LHCb collaboration, R. Aaij *et al.*, *Precision measurement of the* B_s^0-$\bar{B}_s^0$ *oscillation frequency with the decay* $B_s^0 \to D_s^-\pi^+$, New J. Phys. **15** (2013) 053021, `arXiv:1304.4741`

[47] Heavy Flavor Averaging Group, Y. Amhis *et al.*, *Averages of b-hadron, c-hadron, and* τ*-lepton properties as of early 2012*, `arXiv:1207.1158`, update available online at `slac.stanford.edu/xorg/hfag`

[48] LHCb collaboration, R. Aaij *et al.*, *Measurement of the flavour-specific CP-violating asymmetry* $a^s_{\rm sl}$ *in* B_s^0 *decays*, `arXiv:1308.1048`

[49] A. Powell *et al.*, *Particle identification at LHCb*, PoS **ICHEP2010** (2010) 020, `LHCb-PROC-2011-008`

[50] LHCb collaboration, R. Aaij *et al.*, *Measurement of the fragmentation fraction ratio* f_s/f_d *and its dependence on B meson kinematics*, JHEP **1304** (2013) 001, `arXiv:1301.5286`

[51] LHCb Collaboration, R. Aaij *et al.*, *Measurement of b-hadron production fractions in* 7 TeVpp *collisions*, Phys. Rev. **D85** (2012) 032008, `arXiv:1111.2357`